HYBRID CORE-SHELL NANOWIRE ELECTRODES UTILIZING VERTICALLY ALIGNED CARBON NANOFIBER ARRAYS FOR HIGH-PERFORMANCE ENERGY STORAGE

by

STEVEN ARNOLD KLANKOWSKI

B.S., Winona State University, 2009

AN ABSTRACT OF A DISSERTATION

submitted in partial fulfillment of the requirements for the degree

DOCTOR OF PHILOSOPHY

Department of Chemistry
College of Arts and Sciences

KANSAS STATE UNIVERSITY
Manhattan, Kansas

2015

Abstract

Nanostructured electrode materials for electrochemical energy storage systems have been shown to improve both rate performance and capacity retention, while allowing considerably longer cycling lifetime. The nano-architectures provide enhanced kinetics by means of larger surface area, higher porosity, better material interconnectivity, shorter diffusion lengths, and overall mechanical stability. Meanwhile, active materials that once were excluded from use due to bulk property issues are now being examined in new nanoarchitecture.

Silicon was such a material, desired for its large lithium-ion storage capacity of 4,200 mAh g^{-1} and low redox potential of 0.4 V vs. Li/Li^+; however, a ~300% volume expansion and increased resistivity upon lithiation limited its broader applications. In the first study, the silicon-coated vertically aligned carbon nanofiber (VACNF) array presents a unique core-shell nanowire (NW) architecture that demonstrates both good capacity and high rate performance. In follow-up, the Si-VACNFs NW electrode demonstrates enhanced power rate capabilities as it shows excellent storage capacity at high rates, attributed to the unique nanoneedle structure that high vacuum sputtering produces on the three-dimensional array.

Following silicon's success, titanium dioxide has been explored as an alternative high-rate electrode material by utilizing the dual storage mechanisms of Li^+ insertion and pseudocapacitance. The TiO_2-coated VACNFs shows improved electrochemical activity that delivers near theoretical capacity at larger currents due to shorter Li^+ diffusion lengths and highly effective electron transport. A unique cell is formed with the Si-coated and TiO_2-coated electrodes place counter to one another, creating the hybrid of lithium ion battery-pseudocapacitor that demonstrated both high power and high energy densities. The hybrid cell operates like a battery at lower current rates, achieving larger discharge capacity, while retaining one-third of that capacity as the current is raised by 100-fold. This showcases the VACNF arrays as a solid platform capable of assisting lithium active compounds to achieve high capacity at very high rates, comparable to modern supercapacitors.

Lastly, manganese oxide is explored to demonstrate the high power rate performance that the VACNF array can provide by creating a supercapacitor that is highly effective in cycling at various high current rates, maintaining high-capacity and good cycling performance for thousands of cycles.

HYBRID CORE-SHELL NANOWIRE ELECTRODES UTILIZING VERTICALLY ALIGNED CARBON NANOFIBER ARRAYS FOR HIGH-PERFORMANCE ENERGY STORAGE

by

STEVEN ARNOLD KLANKOWSKI

B.S., Winona State University, 2009

A DISSERTATION

submitted in partial fulfillment of the requirements for the degree

DOCTOR OF PHILOSOPHY

Department of Chemistry
College of Arts and Sciences

KANSAS STATE UNIVERSITY
Manhattan, Kansas

2015

Approved by:

Major Professor
Jun Li, Ph.D.

Abstract

Nanostructured electrode materials for electrochemical energy storage systems have been shown to improve both rate performance and capacity retention, while allowing considerably longer cycling lifetime. The nano-architectures provide enhanced kinetics by means of larger surface area, higher porosity, better material interconnectivity, shorter diffusion lengths, and overall mechanical stability. Meanwhile, active materials that once were excluded from use due to bulk property issues are now being examined in new nanoarchitecture.

Silicon was such a material, desired for its large lithium-ion storage capacity of 4,200 mAh g^{-1} and low redox potential of 0.4 V vs. Li/Li^+; however, a ~300% volume expansion and increased resistivity upon lithiation limited its broader applications. In the first study, the silicon-coated vertically aligned carbon nanofiber (VACNF) array presents a unique core-shell nanowire (NW) architecture that demonstrates both good capacity and high rate performance. In follow-up, the Si-VACNFs NW electrode demonstrates enhanced power rate capabilities as it shows excellent storage capacity at high rates, attributed to the unique nanoneedle structure that high vacuum sputtering produces on the three-dimensional array.

Following silicon's success, titanium dioxide has been explored as an alternative high-rate electrode material by utilizing the dual storage mechanisms of Li^+ insertion and pseudocapacitance. The TiO_2-coated VACNFs shows improved electrochemical activity that delivers near theoretical capacity at larger currents due to shorter Li^+ diffusion lengths and highly effective electron transport. A unique cell is formed with the Si-coated and TiO_2-coated electrodes place counter to one another, creating the hybrid of lithium ion battery-pseudocapacitor that demonstrated both high power and high energy densities. The hybrid cell operates like a battery at lower current rates, achieving larger discharge capacity, while retaining one-third of that capacity as the current is raised by 100-fold. This showcases the VACNF arrays as a solid platform capable of assisting lithium active compounds to achieve high capacity at very high rates, comparable to modern supercapacitors.

Lastly, manganese oxide is explored to demonstrate the high power rate performance that the VACNF array can provide by creating a supercapacitor that is highly effective in cycling at various high current rates, maintaining high-capacity and good cycling performance for thousands of cycles.

Table of Contents

List of Figures

List of Tables

List of Abbreviations

C-Rate	Current Rate
CNF	Carbon Nanofiber
CNT	Carbon Nanotubes
CPE	Constant Phase Element
CV	Cyclic Voltammetry
CVD	Chemical Vapor Deposition
DMC	Dimethyl Carbonate
EC	Ethylene Carbonate
EDL	Electric Double Layer
EDLC	Electric Double Layer Capacitance
EDS	Energy Dispersive X-ray Spectroscopy
EES	Electrical Energy Storage
EIS	Electrochemical Impedance Spectroscopy
EMC	Ethyl Methyl Carbonate
EOS	Effective Oxidation State
Kel-F	Polychlorotrifluoroethylene polymer
Li^+	Lithium-ion
Li/Li^+	Lithium Oxidation Potential
LIB	Lithium-ion Battery
mAh	Electrical Storage Capacity, milliAmpere-hours
MWCNT	Multi walled Carbon Nanotubes
NW	Nanowire
OCP	Open Circuit Potential
PECVD	Plasma Enhanced Chemical Vapor Deposition
PT	Power Test
QCM	Quartz Crystal Microbalance
Redox	Reduction-Oxidation Reaction
S/m	Siemens per meter
SC	Specific Capacity
SEM	Scanning Electron Microscopy
SEI	Solid Electrolyte Interphase
SHE	Standard Hydrogen Electrode
SOC	State of Charge
TEM	Transmission Electron Microscopy
VACNF	Vertically aligned carbon nanofiber
XPS	X-ray Photoelectron Spectroscopy

Select Elements of the Periodic Table

Li	Lithium	Cr	Chromium
N	Nitrogen	Mn	Manganese
C	Carbon	Fe	Iron
O	Oxygen	Co	Cobalt
F	Fluorine	Ni	Nickel
Na	Sodium	Cu	Copper
Mg	Magnesium	Zn	Zinc
Al	Aluminum	Ge	Germanium
Si	Silicon	Ru	Ruthenium
P	Phosphorus	Ag	Silver
S	Sulfur	Sn	Tin
Cl	Chorine	Sb	Antimony
Ti	Titanium	Bi	Bismuth

Acknowledgements

I owe a debt of gratitude to my research advisor, Professor Jun Li, for his immeasurable patience, guidance, and continued support of these projects throughout the years. He provided me the freedom to pursue my own ideas while providing guidance and tutelage to improve my skills and professionalism. I would not have found a more interesting field to be part of without his efforts and experience. I would also like to thank my collaborator, Ronald Rojeski, of Catalyst Power Technologies, who has been so beneficial in acquiring the resources needed for the projects and his efforts in filing patents that make this body of work much more yielding. Thank you as well to the Kansas State University Research Foundation (KSURF) for their support in our technology transfers and to its board for their gracious scholarship program that supported my research. Thank you to Clifton E. Meloan Analytical Graduate Student Fund and the Scott Fateley Memorial Fund for their assistantship in my scholarly work.

Special thanks to my group members, past and present: Dr. Lateef Syed, Jeremy Essner, Qin Li, Dr. Jianwei Liu, Dr. Yifen Li, Dr. Yueping Fang, Yichen Zheng, Dr. Gaind Pandey, Dr. Luxi Swisher, Dr. Foram Madiyar, Yiqun Yang, Emery Brown, and Paul Harrison. Special thanks to Dr. Gary Malek and Professor Judy Wu at the University of Kansas for their contribution and materials expertise. I would like to also thank Professors Kenneth Klabunde, Christopher Culbertson, Daniel Higgins, and Larry Erickson for being on my committee and D. V. Satish Chandra for serving as its chair. Much appreciation goes out to the Department of Chemistry, its Faculty and Staff, Phi Lambda Upsilon - Alpha Epsilon, the Graduate School, and all my friends. What can I say...y'all have been great! Your support of my research over the last five years has been exceptional and I could not ask for a better community to allow me so willingly to develop my talents.

I wish to acknowledge the following agencies for their support for my research: National Science Foundation - Experimental Program to Stimulate Competitive Research in Kansas (Kansas NSF-EPSCoR) award EPS-0903806, National Science Foundation - Civil, Mechanical and Manufacturing Innovation Division (NSF-CMMI) grant 1100830, Kansas Space Grant Consortium, National Aeronautics and Space Administration (NASA) grant NNX13AD42A, and the matching support from the State of Kansas through Kansas Technology Enterprise Corporation.

Dedication

Perseverance- Steadfastness in doing something despite difficulty or delay in achieving success. (Oxford Dictionary, 2015)

My five and a half years in graduate school has certainly been a test of perseverance, if not, my resolve to continue in the face of adversity. Hurdle after hurdle emerged, causing moments of frustration, anger, and pain; but I learned how to handle them better each time. As some would say, “that’s just life”, but I on the other hand would call it “character building”. I may have lost a step or two, but as perseverance would have it, I pushed to get back up, give a big smirk and press on. These trials have rewarded me with a stronger temperament and true understanding that good things do come to those who work for it and never give up. So, here lays my dissertation, a ‘partial fulfillment of the requirements for the degree of Doctor of Philosophy’ for you to read while I handle more pressing issues.

My Story

I will take this moment to remember those who helped get me here. First and foremost are my mother and father, Mary and Glen Klankowski. As the youngest son of a math teacher and a diesel mechanic, I developed an striking perspective to the world, one with a deep respect for education and its ability to truly ‘set one free’, instilled by my mother. A mother that would always ask, “Is your schoolwork done?” as I headed out the back door to play (and it usually was). The same question would lead me to chuckle one evening when I heard those words again during my last semester of college. She was proud of me and did everything she could to make sure I succeeded. To say the least, she helped me through the tough times, supported me on whatever I attempted, even if she didn’t know the issues at hand; and allowed me to proceed in the career that best suited my talents. That back door led to a garage, housing every shop tool imaginable. Golly, if I didn't know my arithmetic, I would certainly know how to turn a wrench. It was there that I learned how to repair everything; my Father and I would work on the family cars, built a room full of model railroads, and took care of any issues with the house. I learned about electricity, craftsmanship, and dealing with life's little stresses. Naturally, all of that steered me toward engineering, starting out in the Composite Materials Program at Winona State University, where I learned about composite materials that are now ubiquitous to our daily life. The interdisciplinary coursework of that major drove me to learn more about the materials themselves and wanting to complete the chemistry program as well, for which I majored in both. I was destined to find a career in industry, but an entirely different unearthly power had me thinking about graduate school: a fireball of an ex-girlfriend. Needless to say, I followed my heart to Kansas and got burned like the prairies of the Flint Hills in early spring. Not unlike the native grasses that grow there, the scorching allowed me to clear away the old and put up new shoots, which have resulted in my success in the field of electrical energy storage. The journey has taught me to take some leaps of faith, knowing I have the skills to survive and will make best of what I receive. Kansas, you have provided me the best adventure I could ever ask for; one that I will remember for the rest of my life.

The most defining moment of my life and tenure at Kansas State University was the unexpected death of my mother on July 28th, 2010. I lost the strongest, most trusting supporter in my life to a little bacterium known as MRSA. The situation was disorientating; I was overcome by grief, anger, and had a loss of reason in things I did. As I look back at that time in my life, the lessons that show through are that this one life is really short and that family and friends are the most important things one can have. Probably the best lesson came from an old schoolmate of mine who gave me the most inspiring perspective on all of it, "We are all made of energy, and since energy must be conserved in this universe, your Mother's energy did not leave me, but only returned to world around us...remember that she is now all around you." God, she's going to be a renowned chemist one day. A solemn demand from my mother that I must complete graduate school has become the single most concrete reason why this dissertation sits before you.

To my mother, my father, my brother and sisters, and my whole family, I dedicate my dissertation to you. May it not be a symbol that I spent five years to only Pile it Higher and Deeper than the rest of you, but to hopefully a better future through my work. As we have all learned to do.

Outlook

From this ridge top, I can clearly see that our society has an uncontrollable thirst for energy, and that we would consume whatever natural resources available till we don't have even a tree leaf to wipe our own with. With crude oil prices below $60 a barrel and polices being enacted that block clean, renewable energy initiatives from being implemented, this wave of enthusiasm to change our ways will burn up like the flame from a refiner's flare stack. We need to kindle that enthusiasm and begin utilizing the natural resources on this Earth more effectively which not only would enhance our life, but also preserve our race. It will take perseverance when the worst of doubters show up to criticize our work, but with strong, scientific evidence I will help stand up to them and show how as a society we need to change or risk losing everything. From our sources of energy, to policy reform, to our at-home family values, there is plenty of work to be done. We need to step beyond our petty differences and far-winged politics to cooperate more intelligently and move forward with a renewed vision of the place we want for our grandkids. My dissertation is just one step in that path of change, with hope that my work in energy storage systems will spur a long and useful process that leads to a greater debate of energy management, which will be needed as part of renewable energy sources.

I vow to dedicate my life to making sure my family, and yours, will have a better world to live in than the one I see forthcoming. One step at a time, for that is all we can do.

Hey Greeno! We’ve got some work to do.

Preface

As part of the work performed under the Kansas NSF-EPSCoR initiative, Climate Change and Renewable Energy and in collaboration with industrial partner Catalyst Power Technologies, this research began with a focus on developing energy storage systems (ESS) that could store and deliver more electrical charge, at faster rates, and at reduced weight. This lofty goal was positioned to benefit various sectors that require the use of electrochemical energy storage, as well those that can be aided by its implementation since current technologies cannot meet their demands. With the use of advanced nanoscale materials and a three-dimensional scaffold that functions as the current collector, this research looked to enhance ESS performance through increased electrode/electrolyte interface, reduced ion diffusion lengths, and improved electrical interconnectivity between the active materials. Investigations concentrated on both the physical and electrochemical characterization of the electrode materials, which determine the performance of a particular system, and the benefits of the vertically aligned carbon nanofiber (VACNF) array as a scaffold, supporting the highly active energy storage coating. Chapter 1 will introduce the principles behind the use of silicon, titanium oxide, and manganese oxide, while detailing various methods in the literature to overcome shortfalls in energy density and power density. Chapter 2 introduces the features of the VACNF and describes the overall methods of material fabrication, assembly, and analysis of the fabricated electrodes. Chapter 3 will present the characterization of the Si-coated electrode while Chapter 4 focuses on the rate dependence phenomenon seen from the electrode. Chapter 5 will demonstrate the characteristics of the TiO_2-coated electrode with Chapter 6 describing the performance of it with the Si-coated electrode to create a Si-TiO_2 battery-supercapacitor hybrid. Chapter 7 will demonstrate other capabilities of the VACNFs by use in aqueous systems to improve rate performance and capacity of an MnO_2-

coated electrode. Chapter 8 will summarize all the work performed and give a perspective as to where the field and vertically aligned carbon nanofibers will go next.

Chapter 1 - Introduction

The dissertation documents the fabrication and characterization of three-dimensional electrodes designed around the use of a vertically aligned carbon nanofiber (VACNF) array serving as a scaffold to improve the electrochemical performance of energy storage materials. The work strived to develop electrodes that could store more energy when operated at higher current rates, while having a long service life. Chapter 1 presents an overview of advanced energy storage electrodes, their principles, and how transitioning to nanoscale materials improved performance. The focus will then narrow in on the primary materials used in this work: silicon, titanium dioxide, and manganese oxide.

1.1 Motivation

1.1.1 Our Addiction to Producing CO_2

Humans have consumed Earth's natural resources since the dawn of their existence, even learning how to manipulate those resources to develop new materials that help satisfy their ever-increasing individual desires. What were amenities in the past are now everyday necessities to conducting business and living; all of which require some form of energy to be utilized. For that energy, society has become exceedingly dependent on some of Earth's most lucrative resources, e.g. oil and coal, to meet demands; however, that addiction has come with some lasting consequences. The burning of fossil fuels is the largest source of carbon dioxide (CO_2) emission to the atmosphere, producing around 21.3 billion tons per year and climbing.[1] It is estimated that Earth's natural processes can only absorb half of that amount, leaving a net increase each year. In December of 2014, the National Oceanic and Atmospheric Administration (NOAA) announced that atmospheric CO_2 concentrations at the Mauna Loa Observatory in Hawaii reached a historic 400-ppm during the months of April, May, and June of that year, and are projected to climb even higher for 2015.[2] The increased CO_2 concentrations allow for more radiative forcing, which contributes to warmer temperatures globally and cause of significant change to the Earth's climate and ecosystem. With energy demands on the rise from industrializing nations and the collective consciousness knowing that oil and coal reserves are limited, the need to implement and establish alternative sources of energy has never been greater.

Fortunately, the gantlet has been picked up and looks to be reaching a turning point. Over the last five years, the greatest influx of renewable energy installations has occurred, with wind and solar dominating the new production spectrum.[1] People are asking for more fuel-efficient vehicles, with all electric and fuel cell powered cars becoming more economical with their scale up. Buildings are being designed around energy efficiency and business practices are being based around both economical principles as well as environmental impact. Nevertheless, there are some legacy players within the energy sector that continue to fight this progress, in order to maintain their prominence and show a profit to their shareholders, however, support is building for a more sustainable energy economy, but that enthusiasm can be easily destroyed.

1.1.2 Clean Energy Storage

With approximately 40% of the total United States energy consumption devoted to electrical generation and an additional 30% to transportation,[3] the installation of clean electrical generation technologies will be critical to reducing fossil fuel consumption (and CO_2 emissions) and to supporting a more sustainable and energy efficient future. Although major utilities have begun diversifying their portfolios, with reports showing wind and solar comprising 55% of their newly added electric generation capacity for 2014;[4] production from renewable sources still accounts for a little less than 14% (6.3% - Hydroelectric) of the total US energy production per year.[5] Although harnessing of wind and solar energy is straight forward, their electrical generation is greatly affected by weather conditions, with periods of fluctuation or complete unavailability. One solution that has been slow to implement is the combination of these generation systems with large energy storage platforms, capable of storing additional charge during peak hours of generation and delivering it during periods of high demand or low production. The elimination of fossil fuels from generation will rest on this requisite.

Currently, capital costs have limited implementation of larger energy storage platforms from being constructed, but are in the pipeline as their benefits are well noted. Bulk power management has been primarily achieved using pumped hydroelectric and compressed air energy storage, however, these systems are limited to geographical specific sites. Other platforms are currently handled by more mature systems, such as lead acid and Zn-based flow batteries, since footprint and weight are not a significant issue.[6] Interestingly enough, plans are being made to use battery modules pulled from old hybrid electric cars and utilize the remaining life for the large energy storage farms or for electrical backup during power outages.

The automotive industry is set to change the most from alternative energy sources as manufacturers are already focused on developing cleaner propulsion systems that operate on bio fuels or completely electric drives. From biofuels, to advanced hybrid engines, to all-electric vehicles, they are utilizing different methods to improve fuel mileage and in hope to gain market share. Key to this will be the development of a new electrical energy storage (EES) systems capable of handling the very large currents demanded during acceleration and regenerative braking, as well as to store more energy for longer trips without the driver experiencing range anxiety and undesired recharging time. To accomplish this, significant advances will need to be made to find the right materials chemistry to provide this kind of power in a smart, compact volume. All of this connects back to the use of cleaner electrical generation, for more electric cars will utilize the grid more extensively for charging, and without renewable energy production, electric cars will be the slight of hand for the transportation industry to tout zero emission operation vehicles. Currently, the relative high cost per kilowatt-hour and unfortunate massive weight of electrical energy storage devices of today are the biggest hurdles to greater acceptance of electrically driven vehicles. With cost estimates of ~$410/kWh[7] for Li-ion battery packs, the total price of vehicle with good range (60 kWh, ~200 miles @ 305 Wh/mile, $24,600 just for the batteries)[7] is still not competitive with the internal combustion engine. With current petrol prices in the lower $2.00 range, the cost per kWh needs to come down significantly (< $200/kWh) before electric vehicles are seen as economical.[7] In that same time, performance of energy storage systems must be improved to provide greater energy density and power output, while showing longer efficiencies than materials can provide today.[8]

1.2 Principles of Electrochemical Energy Storage

1.2.1 Thermodynamics

The following summarizes the thermodynamic aspects of electrochemical energy storage from Bard and Faulkner [9] and Winter and Brodd [10]. Although electrochemical energy storage systems can employ various mechanisms to store energy (principally Faradaic and Non-Faradaic reactions), they are limited by the thermodynamics of reversibility.[10] In order for any electrochemical system to repeatedly store charge, the system is required to be chemically reversible. This means:

$$O + ne \rightleftharpoons R \tag{1.1}$$

where O represents the oxidized species, and R is the reduced species, which form the chemical reduction-oxidation (RedOx) couple, with n number of electrons that are transferred to perform the charge transfer. All electrochemical cells are governed at equilibrium by Gibbs energy equation:

$$\Delta G = \Delta H - T\Delta S \tag{1.2}$$

where ΔG represents the available energy that is released upon reaction, ΔH is change in enthalpy of the system, and TΔS is the absolute temperature of the reaction event and the change in entropy of the system, respectively. Since ΔG represents the free energy available upon reaction, it can equated to the electromotive force of the cell:

$$\Delta G = -nFE_{cell} \tag{1.3}$$

where n is the number of moles of electrons transferred, F is Faraday's Constant of 96,485 C mol^{-1}, and E is the potential difference between the electrodes current redox potentials (V or J/C). When E is positive ($E_{cell} = E_{cathode} - E_{anode}$), the Gibb's free energy becomes negative, which indicates a spontaneous redox reaction between the two electrodes. The Nernst equation provides the link between the potential of the cell and the state of charge or the concentration of reactive species at the electrodes.

$$E_{electrode} = E^{O\prime} + \frac{RT}{nF} ln \frac{C_O}{C_R} \tag{1.4}$$

where $E^{\circ'}$ is the formal potential of the electrode materials, R is the universal gas constant

T is the absolute temperature, n is the number of moles of electrons transferred in the cell reaction, F is the Faraday constant, and C_O & C_R are the chemical activity for the relevant species.

1.2.2 Kinetics

The following summarizes the kinetic aspects of electrochemical energy storage from Bard and Faulkner [9] and Winter and Brodd [10]. Commercial EES systems of today are designed to operate within the limits of their materials properties, allowing maximum current rate and highest potential possible. When current is allowed to flow, oxidation or reduction reactions occur at each electrode near the phase boundary between the electrode/electrolyte. This reaction is governed by Faradays law and will continue as long as the Gibbs free energy is negative between the two electrodes, at a rate given by the Bulter-Volmer equation:

$$i = i_o \exp\left[\alpha nF/RT\right] - \exp\left[\left(1-\alpha\right)nF/RT\right] \tag{1.5}$$

where i_0, α, n F, R, T are exchange current, transfer coefficient, polarization, Faraday constant, universal gas constant ($8.3144621\ \mathrm{J\,K^{-1}\,mol^{-1}}$), and temperature, respectively. The two distinct exponential terms in Equation 1.5 determine the rate of reaction in discharge and charge directions. The sum of these rates gives the net rate of reaction. The exchange current, i_0, depends on the concentrations of reactants and products, temperature, and the nature of the electrode-electrolyte interface. In a reaction with a high exchange current, both the discharge and charge reactions occur rapidly and are deemed reversible. For a large value of i_0, a large current can be obtained with a small over-potential polarization. With carbon electrodes there is very little over polarization within the electrode as the electric conductivity is very high throughout. However, highly capacitive materials based on metal oxides show significantly reduced electric conductivity, causing significant over-potential to be needed before establishing reaction:

$$E_{op} = E_{oc} - \eta \tag{1.6}$$

where E_{op}, is the operating voltage, E_{oc} is the open-circuit voltage (the potential difference between the electrodes) and η is the overvoltage (deviation in the equilibrium open-circuit voltage from its theoretical value, caused mainly by polarization). Therefore, the available energy is at its maximum when the cell voltage is close to the open-circuit voltage, because the cell's value is associated with the cell capacity and average operating voltage:

$$E = Q_{sp} * E_{op} \tag{1.7}$$

where Q_{sp} is the specific capacity E is the available energy.

1.2.3 Quantization of Energy Storage

The quantization of energy storage is useful in comparing technologies, defining the amount of charge that a particular device/electrode can store. The Coulomb is the derived unit of electric charge (Q) and the net change in charge on an electrode is related to current:

$$Q = \int I\, dt \tag{1.8}$$

where I represent current in Amperes, t represents time. The capacitance of the device is related to amount of charge developed on the electrodes divided by the voltage (V):

$$C = Q / V = I * t / V \tag{1.9}$$

where the capacitance C equals one Farad if the cell was charged with one Coulomb of charge through a potential difference of one Volt. This value is primarily used to represent non-faradaic, linear capacitance in devices. Capacitance is proportional to the area A and inversely to the distance d between the plates:

$$C = \varepsilon_r \varepsilon_0 (A/d) \tag{1.10}$$

however, for electric double layer capacitance (EDLC), that distance d becomes significantly shorter because the Helmholtz diffuse layer is only a few Ångströms thick. The effective energy stored (E_{eff}) and power (P_{eff}) for a supercapacitor:[11]

$$E_{eff} = C (V^2_{max} - V^2_{min}) / 2 \tag{1.11}$$

$$P_{eff} = V^2 / 8R_{ESR} \tag{1.12}$$

For batteries, faradaic reactions cause the linear capacitance equation (Equation 1.9) to break down, requiring charge to be integrated. In the terms of Ampere-hour, a battery's capacity represents the amount of energy a device can deliver at a given current rate, C/n, from full capacity over n hours. The capacities of some commercial Li batteries are frequently listed for a C/20 rate, or discharge over 20 hours, which is not practical for today's applications. With current rates that can fluctuate depending on use at the time, a devices performance can be better described by several current rates, which creates a unique Ragone curve that describe a devices performance.[12] For better comparison of different materials and devices, gravimetric values are used: Specific energy (Wh/kg) and specific power (W/kg) define the amount of energy and power capabilities of a device with respect to the mass of electrodes. Seen less often, but also very important in nano architectured electrodes are volumetric energy and power densities (Wh/L, W/L). This becomes useful in comparing materials with large volume expansions.

1.2.4 Comparison of Battery and Electrochemical Capacitor

Brain E. Conway has written a historical perspective about the discoveries of Luigi Galvani, Alessandro Volta and many others that led to the key conclusion of how capacitors operate,[13] and up to the time when Volta demonstrated the first electrical battery in 1800.[14] This dissertation is focused on two of the EES systems: batteries and electrochemical capacitors. Although electrochemically similar, each uses a different storage mechanisms (faradaic and non-faradaic) to store energy, where the primary differences are the time constants of their redox reactions and their reversibilities.[10]

Batteries derive their electrical energy indirectly through chemical conversion (RedOx) reactions of species within the electrolyte onto the electrode surface, or in the case of Lithium ion batteries, through an oxidation state change or by electrical stabilization after lithium intercalation or insertion. A battery cell is comprised of the anode (negative electrode) and cathode (positive electrode), which are connected through an ionically conductive electrolyte that can transport the desired species, but electronically insulative to prevent electron transfer and self-discharge.[10] The electromotive force developed between these electrodes is intrinsic to the RedOx potentials on each electrode with respect to the amount of each ion species present. There are two systems: primary batteries which are unidirectionally discharged and discarded, while secondary batteries are capable of RedOx cycling with great efficiency over thousands of cycles. Focusing on the latter case, and more specifically Lithium-ion batteries, the entire electrode mass becomes involved with the storage capacity by means of lithium diffusion into and out of the electrode, causing substantial mechanical stress as phase changes occur throughout during cycling.[15] These inter-conversions must take place for charge storage to occur, while the electrodes must subsist to such interconversions for long-term reversibility of cycling.

As for capacitors, their capacitance is derived from the direct buildup of electrical charge at the electrode surface, separated from the oppositely charged particles. The charge storage capacity of parallel plate designs is limited to largest possible surface area and smallest separation between electrode possible. Thus, electrolytic capacitors have an advantage, by developing charge at the electrode/electrolyte boundary through the use of charged species to form an electric double layer (EDL).[13] The charge buildup is proportional to the surface area of the electrode and thus electrodes with high specific surface area are key towards greater capacitance, values that can reach several hundreds of Farads per gram.

However, unlike simple EDLC's that store charge electrostatically between the electrode and the ions, certain materials are capable of allowing ions to cross the electric double layer and perform a faradaic reaction with material below the surface of the electrode, developing additional storage that has become known as pseudocapacitance.[13] Not unlike battery's faradic response, this charge storage is much quicker in dispensing charge, as the electrode is designed to allow greater access to materials and that ion has not diffused far within the host material, which allows pseudocapacitors to charge and discharge at much higher rates.

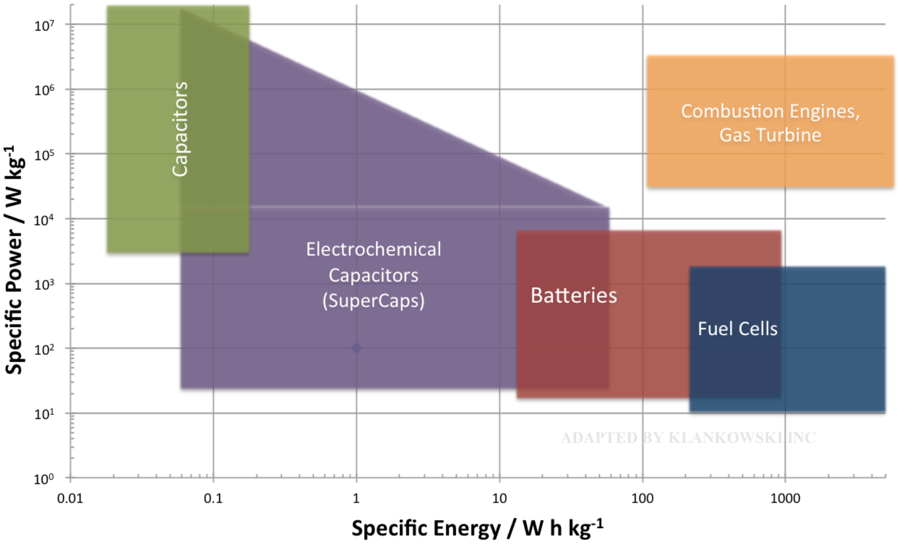

Figure 1.1 – Simplified Ragone plot of various electrochemical energy storage systems compared to combustion engines. Adapted by permission from M. Winter and R. J. Brodd, *Chemical Reviews*, 2004, 104, 4245-4270. Copyright 2004 American Chemical Society.

The differences in power rates and energy storage can be observed by means of the Ragone Plot (Figure 1.1). All energy storage devices can be characterized by the energy and power available for use, with different types of energy storage devices being typically located in respected regions.[12, 16] Here, the four primary EES systems are also compared against internal combustion engines. Capacitors show high specific power (10^4-10^7 W kg^{-1}) with very limited capacitance (< 10^{-1} Wh kg^{-1}) while batteries show lower specific power (10^1-10^4 W kg^{-1}), but with much greater energy density (10-1000 Wh kg^{-1}). Devices that are located between capacitors and batteries are usually defined as supercapacitors, and have various compositions (electrode and electrolyte materials) but are specifically designed with enhanced performance in one characteristic while attempting to maintain the other. Fuel cells are similar to batteries in showing high energy density but are different in that they need a continuous source of fuel (hydrogen, natural gas, etc.) and oxygen to sustain the reaction. Conversion rates are also dependent on diffusion of the feedstock across the membrane to react, which makes power density scaled to surface area and diffusion rate.

For this body of work, higher rate performance was sought through the incorporation of VACNF arrays in hopes to provide fasted electron transfer between the active material and the current collector, shorter ion diffusion lengths thorough nanoscale material, and increase in overall active surface area. The VACNF array is showcased as a robust platform of high performance materials to perform more effectively than thin film electrode. The growth and materials properties of the VACNF array will be described later in Chapter 2.

1.3 Lithium-ion Batteries

A significant portion of this dissertation work involved the initial development and characterization of three-dimensional Li-ion battery electrodes comprised of the VACNF array sputtered with 500 nm of Si or TiO_2. This section will provide a backdrop to the mechanisms and some common materials used in Li-ion batteries

1.3.1 Principles of the Lithium ion Battery

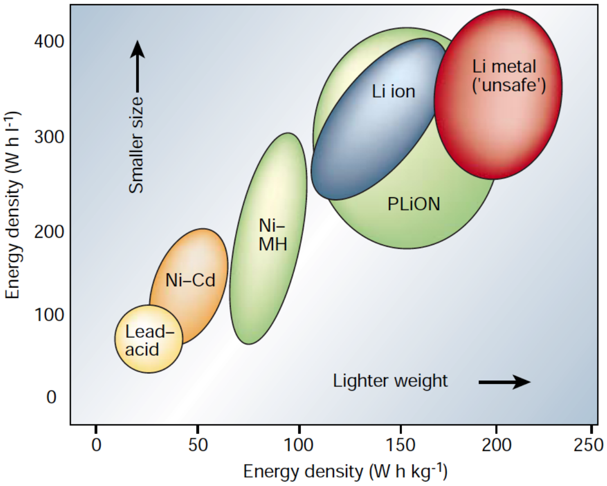

Figure 1.2 – Comparison of the different battery technologies in terms of volumetric and gravimetric energy density. Reprinted by permission from J. M. Tarascon and M. Armand, *Nature*, 2001, 414, 359-367. Copyright 2001 Macmillan Publisher Ltd.

Li-ion batteries are a type of secondary (rechargeable) batteries, which uses Li^+ as the charge carrying species and are shuttled from the anode to the cathode upon discharge only to be returned upon charging. First demonstrated in the 1970's, by M Stanley Whittingham, using Li metal and TiS_2, his work showed that the reaction into the cathode occurs rapidly and was highly reversible at ambient temperatures.[17] This was not coincidental, as Li is one of the most electrochemically active elements on the periodic table, with a standard reduction potential of -3.04 V vs SHE,[9] and has the highest energy per electron found of any solid element. Li also has the lowest density of the alkali metals at 0.53 g cm^{-3}, allowing it to have the highest number of valence electrons per unit mass. All of this allows for one of the lightest and most powerful secondary battery by both gravimetrically and volumetrically (Figure 1.2), now second only to Lithium-air batteries.[18]

It was soon realized that lithium metal could not be used for rechargeable Li^+ batteries, as redeposition of Li onto the solid electrode was not uniform due to previous formation of surface films from the reduction of electrolyte.[19] Rather, Li would form sharp dendrites that grow outward from the electrode and inevitably connect with the cathode causing a short (Figure 1.3).[19] This presented a safety issue with the risk of a fire, and accordingly, the Li-metal anode was abandoned for the secondary batteries (primary Li batteries still utilize pure lithium metal). This spurred research to find both suitable anodes and cathodes that could perform the rocking chair chemistry, which has become this technology's hallmark.

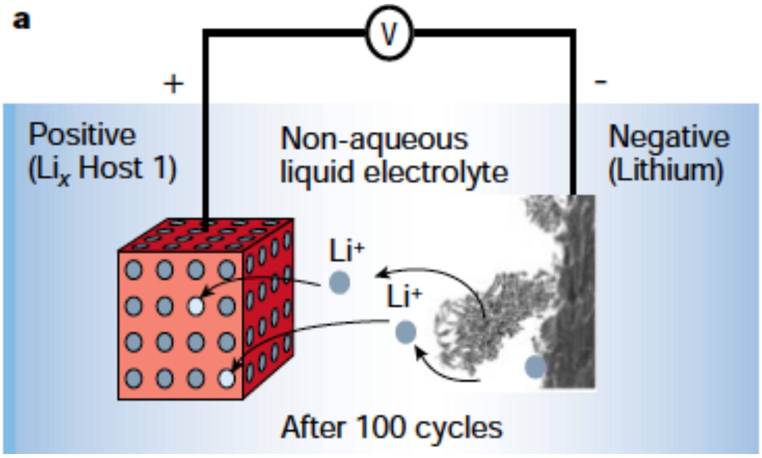

Figure 1.3 – Rechargeable Li-metal battery with dendrite formation off of Li surface. Reprinted by permission from J. M. Tarascon and M. Armand, *Nature*, 2001, 414, 359-367. Copyright 2001 Macmillan Publisher Ltd

Anode Reaction

$Li_xC_6 \rightleftharpoons xLi^+ + 6C + xe^-$

Cathode Reaction

$Li_{(1-x)}MO_2 + xLi^+ + xe^- \rightleftharpoons LiMO_2$

Complete Reaction

$Li_{(1-x)}MO_2 + Li_xC_6 \rightleftharpoons LiMO_2 + 6C \quad (x \leq 1)$

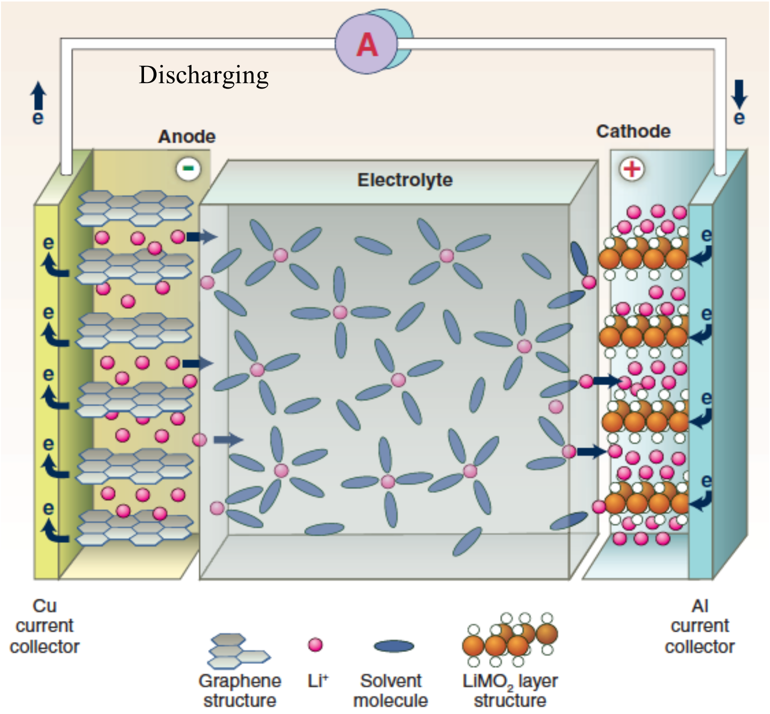

Figure 1.4 – Schematic of a Li-ion Battery, discharging. Reprinted by permission from B. Dunn, H. Kamath and J. M. Tarascon, *Science*, 2011, 334, 928-935. Copyright 2011 AAAS.

Li ion batteries are set apart by the use of both an anode and cathode capable of serving as hosts for Li^+ intercalation/insertion and extraction processes. The reaction of Li^+ occurs when the potential of the electrode is above or below the intrinsic RedOx potential for Li^+ insertion and current equilibrium. The electrodes are separated by an ionic conducting electrolyte that contains a lithium-salt used to shuttle Li^+ in-between, which is usually supported by an electronically insulating membrane that maintains separation of the two electrodes. To charge the cell, a current must be developed that drives the reaction past the equilibrium potential difference, causing Li-ions to oxidize and diffuse from the cathode to the anode, where the Li-ion will diffuse into and become reduced. The thermodynamically favorable reaction of both electrodes in series causes the spontaneous reaction to continue that leads to complete discharge of the cell, as shown in Figure 1.4. The electrons, which are forced to travel outside the cell, are capable of performing the intended work on the attached load based on the voltage developed and current flow allowed by the battery design. The reaction at the electrode follows a basic reaction scheme are represented by a carbon anode and a lithiated metal oxide cathode. The reaction mechanism as the Li-ion battery is discharged and recharged, follows the simple rocking chair analogy, as Li ions are passed from one electrode to another.

In commercial batteries, an electrode is typically a thin film of several tens to hundreds of microns thick, cast onto the respective substrates. Copper is widely used as the anode substrate for its high conductivity and low reactivity to the active materials. Aluminum in predominantly used as the cathode substrate for its ultra-stable, non-passivating oxide layer formed during initial cycling, which prevents further oxidation of the bulk substrate during cycling (standard reduction potential for Al/Al^{3+} is +1.38 V vs. Li/Li^+) and allows moderate electrical conduction to the electrode. Sometimes, nickel-plated foil is also used to limit this corrosion. Another branch of research is dedicated to finding suitable electrolytes with improved properties over the organic carbonates or highly viscous ionic liquids used presently.[20]

1.3.2 Lithium-ion Battery Anodes – Alloys

Various anode materials have been investigated over the decades with very few capable of matching the cycle performance and reliability of the carbonaceous anode.[15] Although refined over the years to improve performance, graphite or graphitic carbon are still the most reliable and stable electrode materials, with the lowest Li^+ extraction voltage plateau of all intercalatable materials and good rate performance while being abundant and low cost. However, the electrical storage capacity of graphitic carbons is limited to 372 mAh g^{-1} (theoretical) due to Li's formation of a LiC_6 compound.[21] Other polymorphs of carbon have been examined, such as hard carbons, carbon nanotubes, and graphene sheets, but their lower Coulombic efficiencies and higher cost make them prohibitive. Transition metal-based materials capable of alloying with Li have been prominent in the literature, showing very high specific capacities and stable cycling.[22] Table 1.1 shows a comparison of the theoretical capacities, operating potential, and other properties for several Li-alloyed materials, with Silicon (Si)[23-25] and Tin (Sn)[26, 27] being most intensively studied. Transition metals are capable of forming Li rich alloys, coordinating with multiple Li^+ to form the alloy, most having two or more. The Li insertion potentials of various metals a range of 0.4 V up to 0.9 V vs. Li/Li^+, which are suitable to counter cathodes already in use, providing a large potential for sustained power output.

Table 1.1 – Comparison of Various Lithium-Alloy Materials Used as LIB Anode. Adapted by permission from W. J. Zhang, *Journal of Power Sources*, 2011, 196, 13-24. Copyright 2011 Elsevier.

Material	Li	C	Mg	Al	Si	Sn	Bi	Sb
Lithiated Phase	Li	LiC_6	Li_3Mg	LiAl	$Li_{22}Si_5$	$Li_{22}Sn_5$	Li_3Bi	Li_3Sb
Density (g cm^{-3})	0.53	2.25	1.30	2.70	2.33	7.29	9.78	6.70
Theo Specific Capacity (mAh g^{-1})	3862	372	3350	993	4198	994	385	660
Theo. Vol. Capacity (mAh cm^{-3})	2047	837	4355	2681	9786	7246	3765	4422

Volume Change (%)	100	12	100	96	320	260	215	200
Potential vs. Li/Li$^+$ (V)	0.00	0.05	0.10	0.30	0.40	0.60	0.80	0.90

Unfortunately, these alloys undergo a very large volume expansion during lithiation, as large as 296% for Si,[22, 30] which causes great structural stress within the expanding material. Inevitably, this leads to fractures and mechanical failure, which significantly limits the lifetime of the Li-alloy anodes.[21, 24] Upon expansion, the solid electrolyte interphase (SEI) that covers the surface of the electrode becomes stretched and torn, exposing new surfaces to electrolyte. This area is subsequently covered by new SEI layer formation through a series of reaction with Li$^+$ at such low potentials. This SEI formation is important for the stability of the electrode material, providing electrical insulation as well, but at the expense of Li$^+$ being consumed and loss in capacity. Several aspects of SEI formation and its function are beyond the scope of this dissertation and will be touched on minimally.

1.3.2.1 Silicon as Anode

$$\mathrm{ySi} + x\mathrm{Li}^+ + \mathrm{xe}^- \rightleftharpoons \mathrm{Li}_x\mathrm{Si}_\mathrm{y} \qquad (1.13)$$

Since a significant portion of this dissertation will focus on characterization of the Si-coated VACNF anode, this section will present the underlying literature that justifies its design. Electrochemical alloying of Li with Si is unlike conventional intercalation and insertion processes, by the way of forming intermetallic phases, which for crystalline Si would progress in a series from pure Si, to LiSi, $Li_{12}Si_7$, Li_7Si_3, $Li_{13}Si_4$, to $Li_{15}Si_4$, to $Li_{22}Si_5$.[21, 31] However, lithiation at ambient temperatures usually results in amorphic lithium silicides being formed with very little evidence of crystallinity after several cycles. The alloying of Li with the Si makes the electrode inherently safer than carbonaceous ones due to the Li being bound to the Si more strongly and would form Li-SiO_X if exposed to oxygen and moisture. As Table 1.1 shows, a pure

Si electrode could achieve the highest theoretical charge capacity of all Li-alloyed materials at 4198 mAh g^{-1} or 9786 mAh cm^{-3}; 11 fold that of a graphite based electrode (372 mAh g^{-1}).[32] Also, Si has a very low extraction voltage of ~0.3-0.4 vs. Li/Li^+, allowing it to provide a large potential window with conventional cathodes. Si is also far more abundant and environmentally benign, but requires a high level of purification to operate; no a concern with such purification processes already established in the semiconductor industry. The primary issue with using Si as an electrode, or any transition metal alloy, is the large volume expansion that occurs during lithiation; for Si that is 296%.[31]

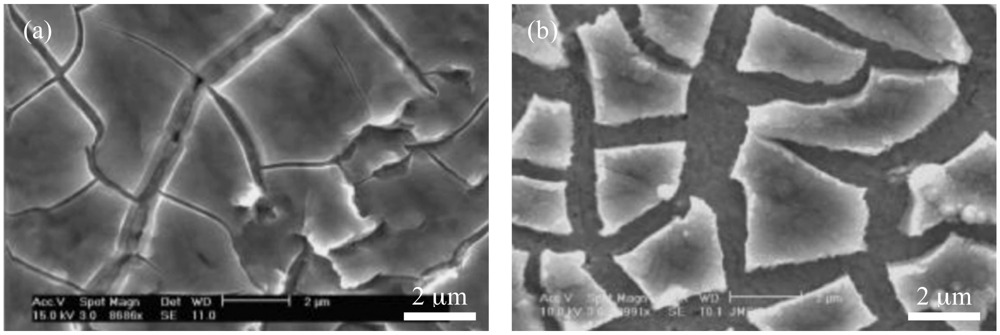

Figure 1.5 – SEM images of 250 nm thick amorphous Si film on copper cycled at C/2.5 for (a) one cycle, and (b) 30 cycles. Reprinted by permission from J. P. Maranchi, A. F. Hepp, A. G. Evans, N. T. Nuhfer and P. N. Kumta, *Journal of the Electrochemical Society*, 2006, 153, A1246-A1253. Copyright 2006 The Electrochemical Society.

It has been shown that ultrathin (~50 nm) amorphous Si film can provide the highest capacity at ~3750 mAh g^{-1} and maintain this value for 200 cycles,[33] however, the small mass per area limits the overall amount of charge stored. Increasing the Si film thickness for higher cell capacity becomes limited by rapid degradation and loss in performance. For one study, the Si film thickness was increased to ~250 nm, obtaining a reversible capacity of ~3000 mAh g^{-1}, however, after a few tens of cycles the capacity declined considerably.[34, 35] Stress gradients that develop upon insertion and extraction inevitably lead to fractures and mechanical failure of the Si material, with signs of delamination from the substrate that resulted in poor connection (Figure 1.5).[21, 24, 36-39] Si powders comprised of 10 µm particles were also examined. However, the first cycle efficiency was only 35% with an extraction capacity of ~1200 mAh g^{-1}, which quickly faded to less than 200 mAh g^{-1} by the 10th cycle.[40] Reducing the particle size to ~80 nm achieved a capacity of ~1500 mAh g^{-1}, and 20 nm particles could attain ~2500 mAh g^{-1} for over 40 cycles.

1.3.2.2 Nanostructured Silicon

The recent approach to addressing the mechanical strain in bulk and thin-film materials is by implementation of nanostructures with enhanced surface-to-volume ratio that can accommodate the lattice stress. Pillars, particle films, and several composites that include binders and conductive additives have all been examined,[41] showing improvement in the cycling performance over the previously published designs; however, each were still limited in cycling lifetime. The concept of 1D Si structures, such as nanowires and nanorods, showed promise with other anode materials,[24] as they enhanced the surface-to-volume ratio to accommodate the lattice stress. Chan et al., showed improved mechanical stability and better electrical connection were obtained with Si nanowires (NWs) through reversible expansion/contraction in both radial and longitudinal direction (Figure 1.6b).[24, 42]

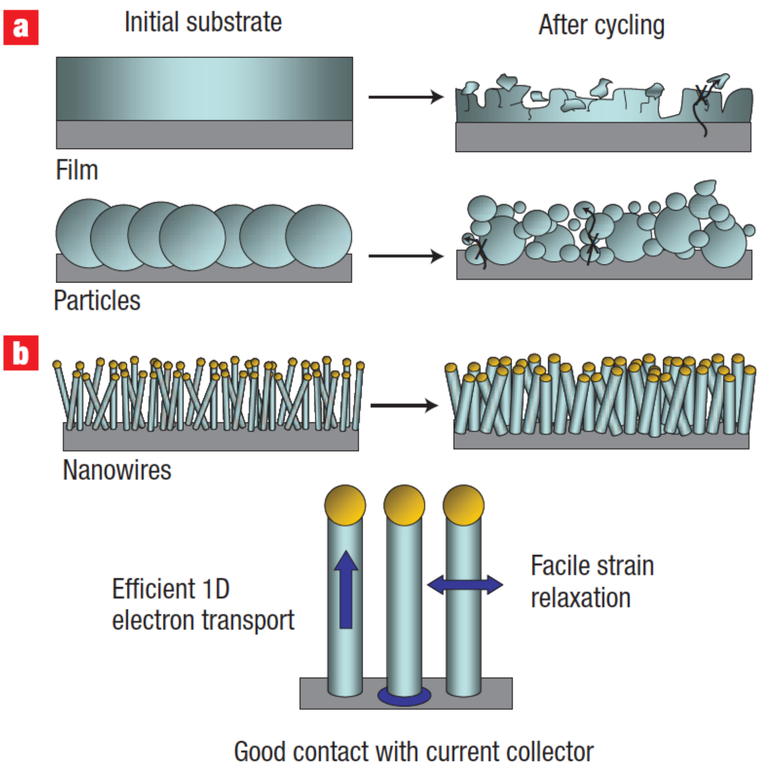

Figure 1.6 – Schematic of morphological changes that occur in Si during electrochemical cycling. (a) Thin films and particles tend to pulverize during cycling. (b) NWs grown directly on current collector do not pulverize or break during cycling. Reprinted by permission from C. K. Chan, H. Peng, G. Liu, K. McIlwrath, X. F. Zhang, R. A. Huggins and Y. Cui, *Nat Nanotechnol*, 2008, 3, 31-35. Coppyright 2008 Nature Publishing Group.

A high capacity of ~3,500 mAh g^{-1} was obtained over 20 charge-discharge cycles at a low charge-discharge rate of C/20, dropping to ~2,500 mAh g^{-1} and even lower as the rate was increased to C/2.[24] It should be noted that the normal charge-discharge rate for commercial Li-ion batteries varies between C/5 and C/1, depending on manufacturer. Therefore, the slow kinetics and the degradation of the electrical connection still limited the available power density in the Si NW anodes, as resistivity of individual NWs was noted to increase by 150 fold after lithiation.[24] To maintain both structural integrity and improve electrical connection, a hybrid structure was employed with a stable carbon core to support the active Si. This was demonstrated by depositing Si shells on randomly stacked carbon nanofibers (CNFs) produced by conventional thermal pyrolysis (Figure 1.7).[43, 44]

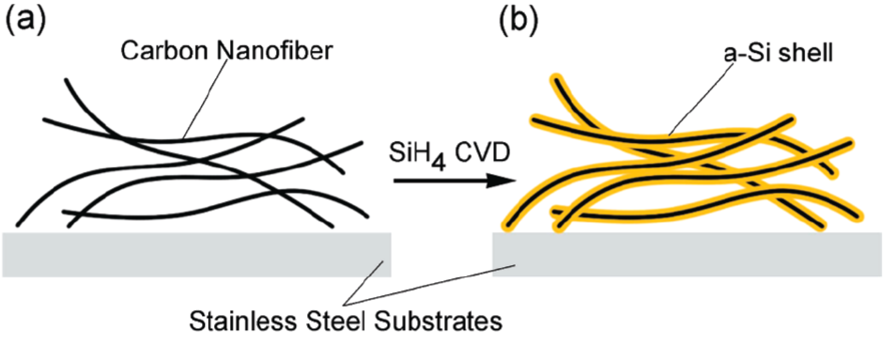

Figure 1.7 – Schematic illustration of Si coating onto carbon nanofibers (a) Bare CNFs. (b) C-Si core-shell NWs. Reprinted by permission from L. F. Cui, Y. Yang, C. M. Hsu and Y. Cui, *Nano Lett*, 2009, 9, 3370-3374. Copyright 2011 American Chemical Society.

The reversibility was significantly improved at a C/5 rate with over 98% Coulombic efficiency achieved in 55 charge-discharge cycles.[43] However, the maximum capacity was only ~2,000 mAh g^{-1} [43] or even lower[44] at C/5 rate and was roughly 800 mAh g^{-1} at C/1 rate.[43] This was likely due to the non-uniform Si coating in these hybrid structures. Si tended to accumulate at the very top surface and did not penetrate deeply into the randomly arranged CNF.[43, 44] Wang et al. explored depositing Si on vertical aligned multiwalled carbon nanotubes (MWCNTs) using chemical vapor deposition (CVD) to form a hybrid Si-MWCNT structure consisting of ~54-57 wt.% of Si.[45] The initial specific capacity (normalized to Si mass) was as high as ~3,300 mAh $(g_{Si})^{-1}$ at ~C/19 rate. However, it dropped to ~1,500 mAh $(g_{Si})^{-1}$ at ~C/2 rate and retained less than 70% of the initial capacity after 100 cycles.[45] The waving and partially entangled structure may still have prevented uniform Si deposition deep into the MWCNT arrays. More uniformly aligned vertical NW arrays proved to be a better candidate for structural support, as demonstrated with straight Cu core NW arrays.[46] This hybrid structure was able to retain 95% of the capacity after 35 cycles, but the Si coating only presented ~25% of the theoretical capacity at C/1 rate.[46]

The goal of this dissertation was to expand on these ideas and improve on the issues, primarily with the use of the VACNF array as a highly conductive three-dimensional scaffolding to support the more active Si (see Chapter 2). The open structure of the VACNF arrays makes it possible for Si to reach deep down into the array, to form a thick, conformal shell around each of the fibers. The sputtering method also proved more useful as it created a shell structure comprised of polycrystalline nanoneedles that developed greater active surface and shorter diffusion lengths.

Various other nanostructured Si materials have very recently been studied, including hollow spheres, egg yolk, porous films, porous nanowires, etc. These materials continue to be studied to reduce the effect of the internal stress and make use of a larger specific surface area and short Li^+ diffusion length, but most are trying to improve mass loading of the electrode and increase overall cell capacity.[21, 24, 32]

1.3.3 Lithium-ion Battery Cathodes

Table 1.2 – Various Electrode Materials Used as LIB Cathode.[47] Adapted by permission from W. J. Zhang, *Journal of Power Sources*, 2011, 196, 13-24. Copyright 2011 Elsevier.

Material	Li	$Li_4Ti_5O_{12}$	$LiCoO_2$	$LiMn_2O_4$	$Li(MnCoNi)O_2$	$LiFePO_4$
Density (g cm^{-3})	0.53	3.5	5.05	4.2	4.7	3.45
Theoretical Capacity (mAh g^{-1})	3862	175	160	110	200	170
Theo. Vol. Capacity (mAh cm^{-3})	2047	613	808	462	940	586
Volume Change (%)	100	<1%	-	-	< 2%	<7%
Potential vs. Li/Li^+ (V)	0	1.6	3.9	4.1	3.8	3.45
Shape of Dis. Curve	Flat	Pseudo	Flat	Flat	Sloping	Flat

A much wider investigation has been performed for cathode materials, with a significant portion of current research spent on computational modeling and high-throughput calculations to narrow in on suitable materials that either have a more stable insertion plateau or a higher operating voltage without compromising safety.[48, 49] Most cathodes are based on transition metal complexes that accept the Li^+ by reducing the oxidation state of the metal in order to maintain charge neutrality.[50] In the past two decades $LiCoO_2$ was the primary choice of cathode, but due to the limited supply of cobalt and its associated costs, alternative materials are being sought which use more Earth abundant elements, like iron[51], titanium,[52] nickel,[53] and/or manganese,[54] that have shown improved stability and higher rate capabilities.[55] Table 1.2 summarizes the properties of various transition metal cathode materials. These cathodes are commonly separated in the literature by their crystal structure: Layered ($LiCoO_2$, $LiTiO_2$), spinel ($LiMnO_2$), and olivine ($LiFePO_4$), as well as mixed metal ($Li[Mn_xCo_yNi_z]O_2$). TiOx is of current interest, showing a flat redox insertion potential that is almost two volts lower than most other metal oxides, which makes it an intermediate electrode capable of operating as an anode or a cathode. TiO_2 electrodes also show large pseudocapacitive contributions that occur when particle size reaches the nanoscale regime, contributing far greater capacity through redox adsorption at the surface than by insertion.[56] This is of interest for high power density applications.[57] Transition metal phosphates have also been promising, with $LiFePO_4$ being prominent having an ultra-flat discharge profile caused by a two-phase transition at a fixed active. The Fe can be replaced with Mn, Co, and even Ni, which affect the plateau voltage and rate performance of the electrode. Li insertion/extraction appears to occur with minimal displacement to the oxide layers of the electrode, creating a better cycle life for the Li-ion battery.[58]

1.3.3.1 Titanium Oxide as Cathode

$$TiO_2 + x\mathrm{Li}^+ + \mathrm{xe}^- \rightleftharpoons \mathrm{Li}_x\mathrm{TiO}_2 \quad X \leq 0.5 \tag{1.15}$$

Building on the same principles seen for Si NWs led this work to the deposit of other Li active materials onto VACNFs. TiOx was chosen for its unique pseudocapacitance behavior while having a Li^+ redox reaction of 1.5-1.8 V vs. Li/Li^+. Being naturally abundant and environmentally benign, this low cost material has been extensively studied for use as an anode. But the loss of more than 1 V in cell voltage (versus standard cathode material) reduces the available power output for the cell compared to one with a graphite or metal alloy anode, recoverable only by its much faster surface capacitance reaction. There are safety advantages for an electrode with a higher redox potential, include no issues of lithium plating and reduced SEI formation on the electrode.

Various compositions of titanium oxides have been demonstrated for use in LIBs, including lithium titanites ($LiTi_2O_4$ and $Li_4Ti_5O_{12}$) and assorted polymorphs of lithiated TiO_2 (Rutile, Anatase, Brookite, & Bronze), mostly as high-safety anodes.[52, 59] The theoretical Li^+ storage capacity is ~175 mAh g^{-1} (at 1.34-1.55V vs. Li/Li^+) for $LiTi_2O_4$ and ~335 mAh g^{-1} (at 1.5-1.8 V vs. Li/Li^+) for $Li_4Ti_5O_{12}$.[59] Lithiation of bulk anatase TiO_2 to the final form of Li_xTiO_2 (with x = 0.5) at ~1.7 V gives a theoretical specific capacity of 168 mAh g^{-1}.[52, 57] The electrode potentials of Ti-based materials lie in the middle of typical anode and cathode materials. Hence it could be used as either electrode.

Overall, Ti-based oxides show excellent Li^+ insertion/extraction reversibility with very minimal volume expansion (10% to 25%) upon lithiation; however, rate capability is low due to heavy polarization within the material at high rates, which is the directly related to the oxides' poor electrical conductivity and sluggish ion diffusion.[52] To address this problem, nanostructured

TiO_2 (<100nm) was used to improve performance by providing a short Li^+ diffusion length with the added bonus of a large electrode/electrolyte surface area for a larger flux capability.[59] Additionally, it is known that active material at this scale enables some extrinsic pseudocapacitance, which lifts the global capacity to even greater values than theoretical values.[57, 59]

1.4 Electrochemical Capacitors

To demonstrate the robustness and high rate performance that the VACNF arrays can provide, electrodes were sputtered with 50 to 600 nm of manganese and subsequently oxidized to form a nanostructured MnO_2 coating that provides excellent rate performance while maintaining a suitable energy density in aqueous electrolyte. This section will provide a background on the principles and materials used in electrochemical capacitors.

1.4.1 Principles of the Electrochemical Capacitor

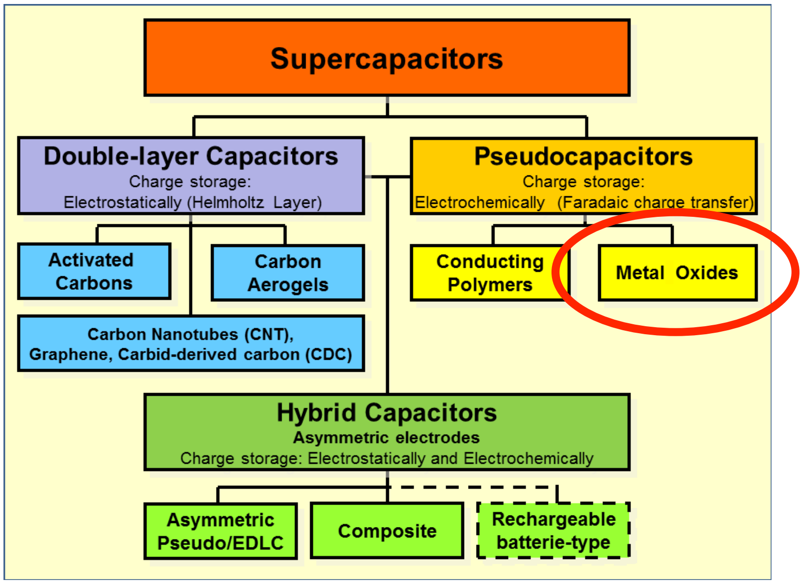

Figure 1.8 – Family tree of supercapacitor types. Double-layer capacitors and pseudocapacitors as well as hybrid capacitors are defined over their electrode designs. Reprinted under Creative Commons 1.0 Universal (CC0 1.0).

An electrochemical capacitor (EC), also referred to as a supercapacitor, is an EES device that can produce both the high-energy storage capability of a battery with the high power deliverance of a capacitor (Figure 1.8). Hermann von Helmholtz was the first to realize that ions form layers in solutions on a charged electrode immersed in electrolyte. In 1853, he presented a model that became the basis for electric double layer capacitance (EDLC).[60] The model has been improved over the years, to what it is today (Figure 1.9).[61-64] Unlike conventional electrostatic parallel capacitors, the EDLC is the buildup of charged ions in two explicit regions near the electrode surface, i.e. the inner compact region, and the diffuse layer. The inner region (Inner and Outer Helmholtz Planes) also known as the Stern Layer, consists of strongly adsorbed ions (generally anions) at the electrode/electrolyte interface, while the diffuse layer consists of a continuous circulation of ions that actively screen the remaining charge at the surface.[10, 13] The thickness of the electric double layer (d), and therefore capacitance, depends on several factors including the type of salt in the electrolyte, size of the ions, and concentration. A flat electrode in a highly concentrated electrolyte could demonstrate a capacitance of only 10–20 mF cm^{-2}. To increase the capacitance, a sufficiently larger surface area is required, resorting to a more three-dimensional electrode. For the cell to operate, two electrodes with opposing charge are required effectively storing the charge in the double layer.

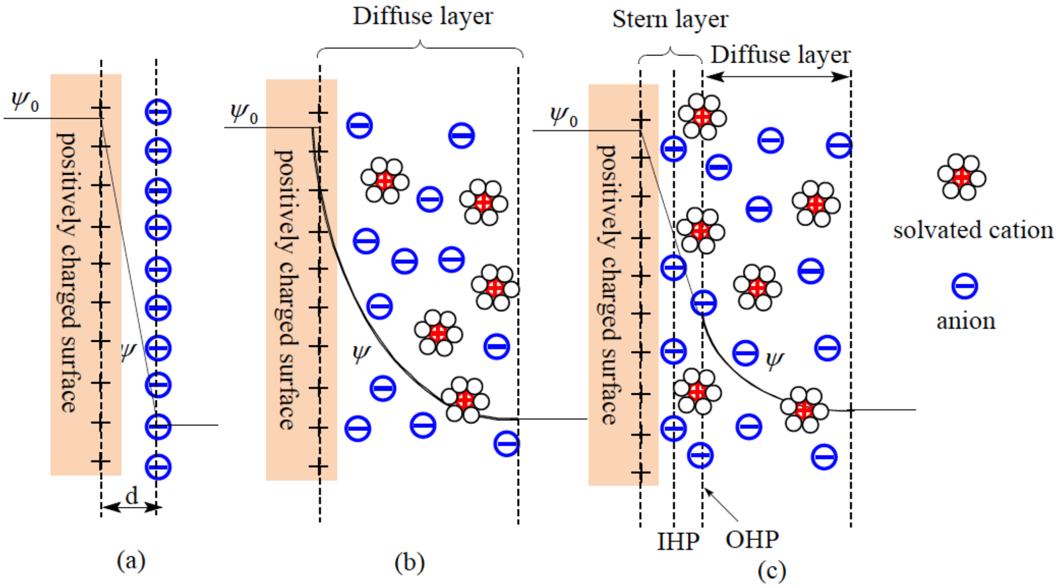

Figure 1.9 – Models of electrical double layer at a positively charged surface: (a) the Helmholtz model, (b) the Gouy-Chapman model, and (c) the Stern model showing the IHP and OHP. Reproduced by permission from L. L. Zhang and X. S. Zhao, *Chem Soc Rev*, 2009, 38, 2520-2531. Copyright 2009 The Royal Society of Chemistry.

Activated carbons with high surface area (1000-3500 m^2 g^{-1}) are widely used for commercial applications; however, limited by porosity issues where not all of the surface area is accessible to the electrolyte.[65] As a result, carbon nanotubes (CNTs) are also used, owing to their tubular nature in allowing electrolyte to access all areas of the material and have a reasonably large surface area (120-500 m^2 g^{-1}) with ultra-high electron conductivity.[66] Lately, freestanding graphene sheets have been of interest, with surface areas up to 2600 m^2 g^{-1}. They can achieve good capacitance while allowing the electrode to be pliable. However, unreliability in production and overall high cost have made them impractical at his time.[66] Each material shows various improvements in porosity, electronic connection, and tunable surface area to improve capacitance; however, energy density of a device can be significantly improved by the use of pseudocapacitive materials.

1.4.2 Metal Oxides as Pseudocapacitive Material

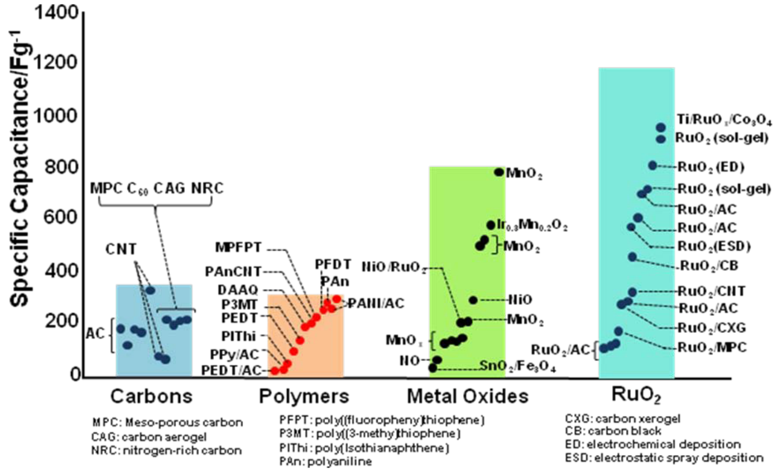

Figure 1.10 – The capacitive performance for carbon and pseudocapacitor electrodes. Reproduced by permission from K. Naoi, P. Simon, J Electrochem. Soc., 2008 17, 34-37. Copyright 2008 Electrochemical Society.

Pseudocapacitive materials are different than simple carbon EDLC materials, since they utilize fast and reversible faradaic reactions to store charge at their surface. These materials are separated into two classes: conducting polymers (polypyrrole, polyanaline, polythiophene), and transition-metal oxides (SnO_2, PbO_2, TiO_2, Fe_3O_4, VO_x, RuO_2, & MnO_2).[67, 68] Distinguished by their conjugated carbon backbone consisting of alternating single and double bonds, conducting polymers are capable of the Redox reactions on this chain of carbon by accepting or extracting electrons, allowing the remaining electrons to become more conductive in order to maintain electroneutrality, thus storing the charge. Not unsuspectingly, conducting polymers suffer from lower cycle life than carbon electrodes because redox sites in the polymer backbone are not sufficiently stable.[62] On the other hand, metal oxides utilize an oxidation state change of the transition metal plus the diffused electrolyte cation to perform faradaic reactions and store charge. Their pseudocapacitive reactions can yield a capacitance that is significantly larger than simple EDLCs, but are known to suffer from lower power densities due to limited conductivity and reduced stability during cycling. Since pseudocapacitance occurs primarily at the surface of these materials, the development of an electrode design with high surface area and short electron pathways for faster transport are crucial.

1.4.2.1 Manganese Oxide as Electrode

In the late 1970's, B.E. Conway performed extensive studies on ruthenium oxide, finding it ideal with pseudocapacitive properties, along with good conductivity and excellent reversibility. However, high cost of ruthenium has deterred its broader application. Therefore, lower cost alternatives, such as manganese oxide (MnOx), have been studied with most focused on the phase change of Mn^{4+} (MnO_2) to Mn^{3+} (Mn_2O_3) since this readily occurs in the potential window of water. Various methods have been used to prepare MnO_2 with ornate structures and morphology, which include thermal decomposition, hydrothermal synthesis, sol-gel, electrochemical deposition, and electrochemical oxidation, etc.[69-75] It has been shown that ultrathin MnO_2 films are capable of achieving capacities close to the theoretical value of 1370 F g^{-1}; however, proton diffusion through the bulk of MnO_2 materials is not fast and only a limited fraction of MnO_2 is electrochemically active, leaving capacitance to be less than desirable at 150 – 250 F g^{-1}.[76] Thus, composite electrodes have been studied that incorporate conductive carbons to support the MnO_2 by provided highly effective electron transport pathways while allowing all the material to become more electrochemically active with little additional mass.[77, 78]

Chapter 2 - Materials and Methods of Electrode Fabrication

This chapter will focus on the unique characteristics and fabrication methods involved in the growth of vertically aligned carbon nanofibers and the subsequent sputtering of Si, TiO_2 and Mn onto the fiber's surface, as well as the fabrication and assembly into cells for electrochemical characterization.

2.1 Vertically Aligned Carbon Nanofibers

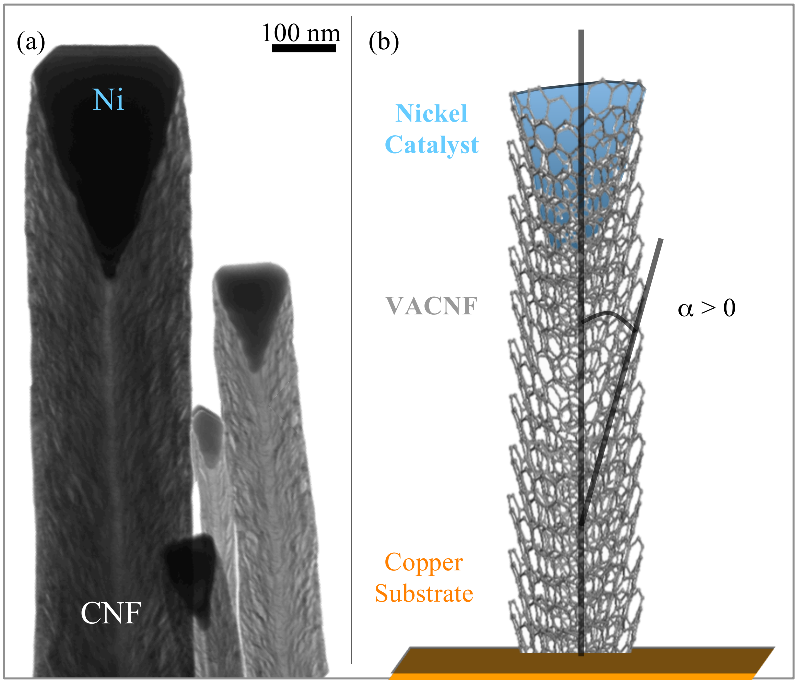

Figure 2.1 – (a) TEM image showing the internal structure of CNFs that where grown on graphite paper with (b) schematic of VACNF internal structure depicting the stacked graphene cups and α the angle between fiber axis and graphene sheet. Scale bar is 100 nm.

A subclass of nanostructured carbon, the Carbon Nanofiber (CNF) is a special type of multi-walled carbon nanotube (MWCNT), distinct by its internal morphology consisting of conical graphene (or graphitic) sheets that are stacked to form a continuous cylindrical fiber instead of concentric seamless tubes, as shown in the Figure 2.1.[79-82] They are distinctive by the difference in angle (α) between the fiber's axis and the graphene sheet at the sidewall, with the CNF having $\alpha > 0^o$.[81] The fiber's diameter can be varied anywhere from 50 nm to 300 nm and even wider, through variation of several parameters. Diameter is critical to providing the desired mechanical strength and integrity during material deposition and subsequent wet electrochemical processes. The length of the CNF can also be varied from a few hundreds of nanometers to well over 20 microns, depending on the time allowed for growth. Along the fiber's sidewall are wealth of broken graphitic edges that act as nucleation sites for the more active materials to bind to the CNF (Figure 2.1b), unlike the smooth basal surface of a carbon nanotube (CNT).[83] Stable electron transport is vital for a long a service life, but due to its herringbone structure, the CNF has both "in-plane" and "interplane" transfer components, which reduces the electron conductivity along the axis to $\sigma = 2.5\text{x}10^5$ S/m, compared to multi-wall CNTs with $\sigma = 10^6\text{-}10^7$ S/m and copper with $\sigma = 5.96\text{x}10^7$ S/m.[84] The CNF also forms a mechanically strong and Ohmic contact with the substrate similar to the shallow roots of a tree.[81, 84, 85]

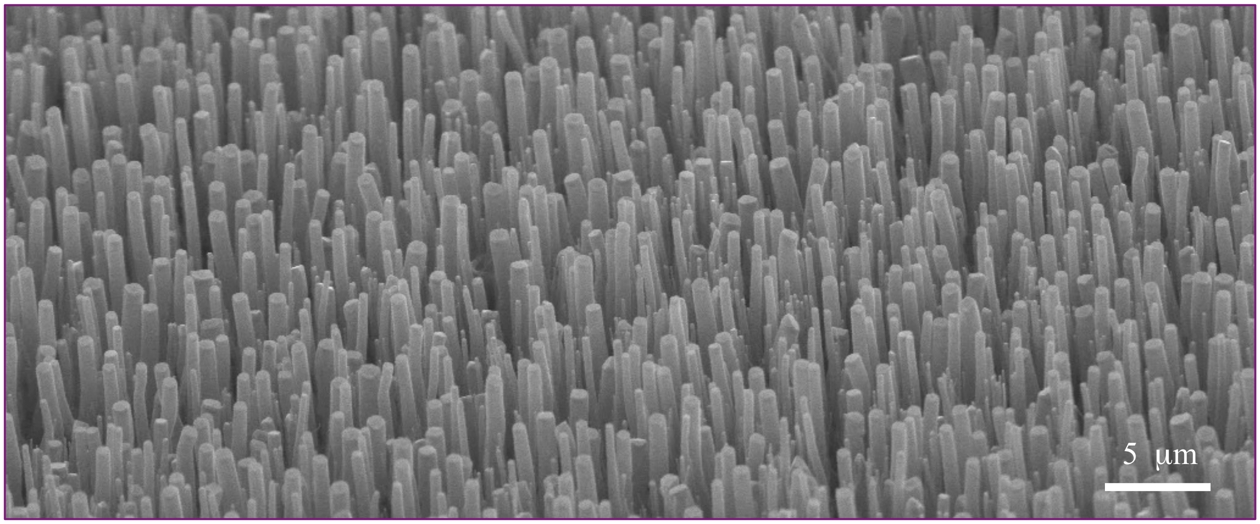

Figure 2.2 – SEM image of VACNF random array. Scale bar is 5.0 µm.

Growth of CNFs can be performed by various thermal and catalytic methods. The VACNFs for this body of work were grown by plasma-enhanced chemical vapor deposition (PECVD) using a Nickel catalyst that was sputtered onto the current collector. The kinetics and parameters for superior CNF growth are well summarized in reviews by Meyappan[85] and

Melechko[81], requiring precise control over temperature, pressure, plasma generation, and feedstock control. With PECVD, the plasma sheath helps to reduce the activation energy of deposition process, allowing growth of the CNF to be more facile. To achieve better growth, an etchant was used (Ammonia) to enhance growth by removing amorphous carbon from the surface of the growing fiber. The vertical alignment of the CNF is a product of the Ni catalyst's interaction with the high electric field that is generated within the plasma sheath. This helps by pulling the catalyst in the direction of the field, forming long cylindrical fibers that are well separated from each other without entanglement, forming a brush-like structure referred to as VACNF array, as shown visually in Figure 2.2. The open space between the VACNFs enables the active material to be easily deposited onto each CNF and form the coaxial shell. The design enables the whole shell to be electrically connected through the CNF core and to remain fully active during the charge-discharge cycling.

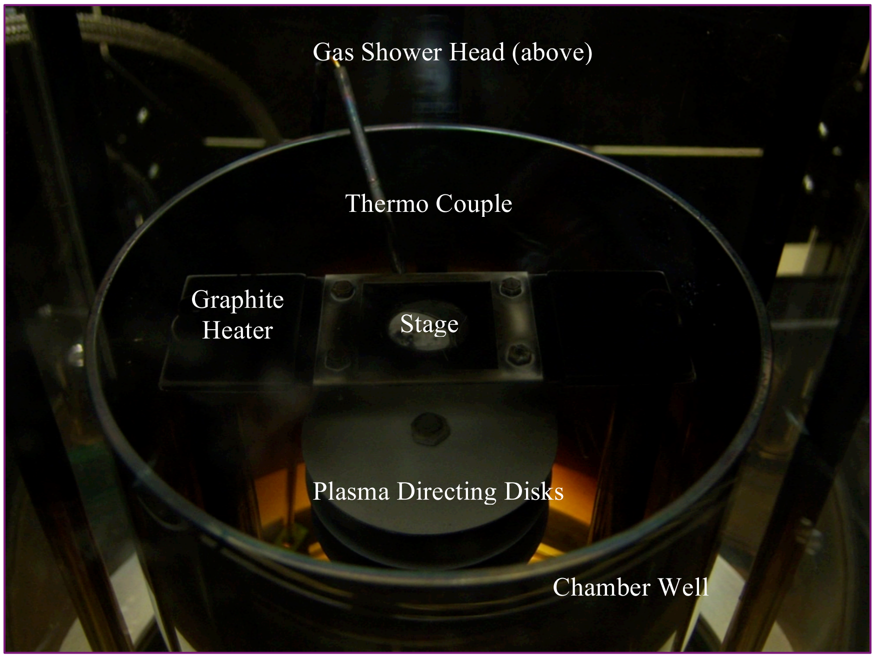

Figure 2.3 –PECVD Growth Chamber, (Nano Instruments, Aixtron, CA)

All of the VACNF growth was performed using a commercial DC-biased PECVD system (AIXTRON, CA). A pre-coated current collector consisting of the Ni catalyst on top of a

Chromium barrier layer (to prevent Ni-alloy formations) is placed inside the reactor chamber and processed following an established protocol, with minor changes depending on the substrate used. A host of parameters can be tuned to improve growth, thicken or lengthen CNFs, and increase areal density. Application of the VACNFs is of endless pursuit, with their use as a form of electrode for batteries,[26, 86-89] capacitors,[90] and photovoltaics;[91, 92] as well in biosensors,[93, 94] and pathogen detection.[95-97]

2.2 Conditions for VACNF Growth

2.2.1 Growth on Copper for Lithium-ion Battery Experiments

Oxygen-free pure copper foils (Copper 102, Hamilton Precision Metals, PA) with the thickness of 84 μm (and in certain cases, 12.7 μm) were employed, which were cut into 15 cm x 29 cm sheets. After a light cleaning with chemical etching in 0.1% citric acid, a 300 nm thick chromium barrier layer followed by a 30 nm nickel catalyst layer was deposited using a high-vacuum Perkin Elmer 4400 series magnetron sputtering system (UHV Sputtering Inc., Morgan Hill, CA). These Ni/Cr/Cu sheets were then punched into disks of 18 mm in diameter, the size required for the testing apparatus.

2.2.2 Growth on Titanium for Pseudocapacitor Experiments

Copper is known to easily oxidize and dissolute into solution at the operating potentials used for the manganese oxide electrodes (standard reductions potential of +0.34 V versus SHE).[98] Titanium was found to be less problematic since a very protective and highly insulative titanium (IV) oxide layer would form by +0.10 V versus SHE (well below the +0.2046 V of the Ag/AgCl reference electrode), allowing very little oxidation to further penetrate the substrate.[98] Ti was also compatible with PECVD growth conditions. Thus, oxygen-free Ti foil with the thickness of 25 μm (Titanium Grade 2, Hamilton Precision Metals, PA) was cut to a 15 cm x 15 cm sheet. A 300 nm thick chromium barrier layer followed by a 30 nm nickel catalyst layer were deposited using a high-vacuum Perkin Elmer 4400 series magnetron sputtering system at UHV Sputtering Inc. The Ni/Cr/Ti sheet was then cut into disks of 18 mm in diameter for test cell use.

2.2.3 General Parameters for VACNF Growth Plasma Enhanced CVD

VACNFs with average lengths of 3.0 μm, and 5.0 μm (one set of experiments using 10 μm fibers), were grown on the respective foils using the PECVD system (AIXTRON, CA) following a modified procedure in literature.[80, 81, 92] The growth chamber was purged with UHP nitrogen then vacuumed down to 75 mTorr before start of recipe. A pre-treatment procedure was applied first by thermally heating the Ni/Cr/Cu substrate to 500 °C in 250 sccm NH_3 at a pressure of 3.9 Torr and then applying plasma at 40 Watts for 60 seconds. The combined effects of thermal dewetting and NH_3 plasma etching break down the Ni film into randomly distributed nanoparticles that catalyze the growth of VACNFs.[80, 81, 92] After the pre-treatment, a mixture of acetylene (at 70 sccm) and ammonia (at 250 sccm) was used as the precursors at 750 °C for copper, (740 °C for titanium) and a pressure of 4.6 Torr. The plasma power was kept at 45 Watts for 20 minutes to grow ~3.0 μm long VACNFs, 30 minutes to grow ~5.0 μm long VACNFs and almost 120 minutes to grow ~10 μm long VACNFs. The processed electrode was allowed to cool by convection under evacuating N_2 flow (1000 sccm) to 80 °C before removal from reactor, and stored in atmosphere till use. SEM images were taken of several samples to confirm dimensions, shown by Figure 2.4. The average diameter of the VACNF arrays was measured by hand and calculated to be ~147 nm. The average length of the VACNF was estimated ~ 3.0 μm.

2.2.4 Calculation of VACNF Array Mass

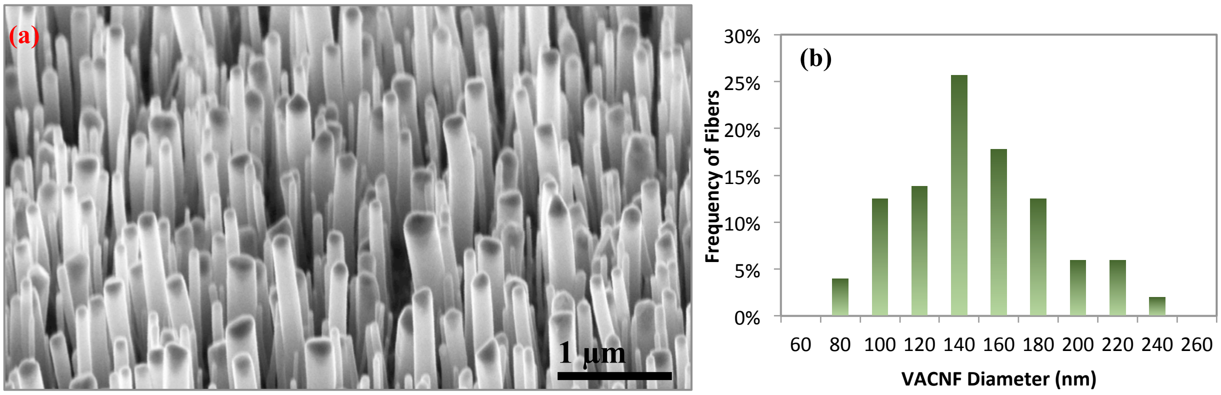

Figure 2.4 – (a) SEM image of VACNFs on Copper, from which diameter of all fibers in image were measured. (b) Histogram of the diameter distribution of 3.0 μm long "as-grown" VACNF array. Scale bar is 1.0 μm.

To provide use useful comparison with other technologies, the mass of all materials needed to be carefully measured. The mass of carbon in the VACNFs could not be reliably measured by weighing the sample before and after PECVD (due to many factors such as thermal history, oxidation of Cu, moisture adsorption, etc.). There is no reliable in-situ measuring technique (such QCM) as well. Hence it has to be estimated from the average structure observed by TEM and SEM, giving ~2.65×10^{-4} g per sample (or ~1.1×10^{-4} g cm^{-2}) for a 3 μm long VACNF array. For a 5 μm long VACNF array, the estimated mass observed was ~4.60×10^{-4} g per sample (or ~1.1×10^{-4} g cm^{-2}), and for a 10 μm long VACNF array, the estimated mass observed was ~7.29×10^{-4} g per sample (or ~1.1×10^{-4} g cm^{-2}). It needs to be noted that this method is quite conservative and likely overestimated the carbon mass, with the real carbon mass being less, not more. The mass of VACNFs is added, when noted, to the mass of active material coating and substrate to calculate specific mass capacities.

2.3 Sputtering Deposition of Shell Material

The shell materials for all projects were deposited by some method of sputtering. The term sputtering denotes the erosion of a target material by particle bombardment (usually UHP Argon or blended gas) and the sequential deposition of material onto a substrate.[99] This is usually performed under ultra high vacuum with very controlled deposition rates. For Si and TiO_2, each were deposited using a magnetron sputtering system where a radio frequency plasma field is generated on the target material. The energized ions bombarded the target, evaporating the material and causing it to slowly diffuse toward the substrate where it will condense. The continued deposition forms a thin film where morphology depends on substrate temperature, rate of deposition, and other target materials properties. For the TiO_2, a for of reactive sputtering was performed where a stream of oxygen is added to the chamber gas, which upon bombardment causes a chemical oxidation to the titanium atom, forming the oxide layer as deposition occurs.

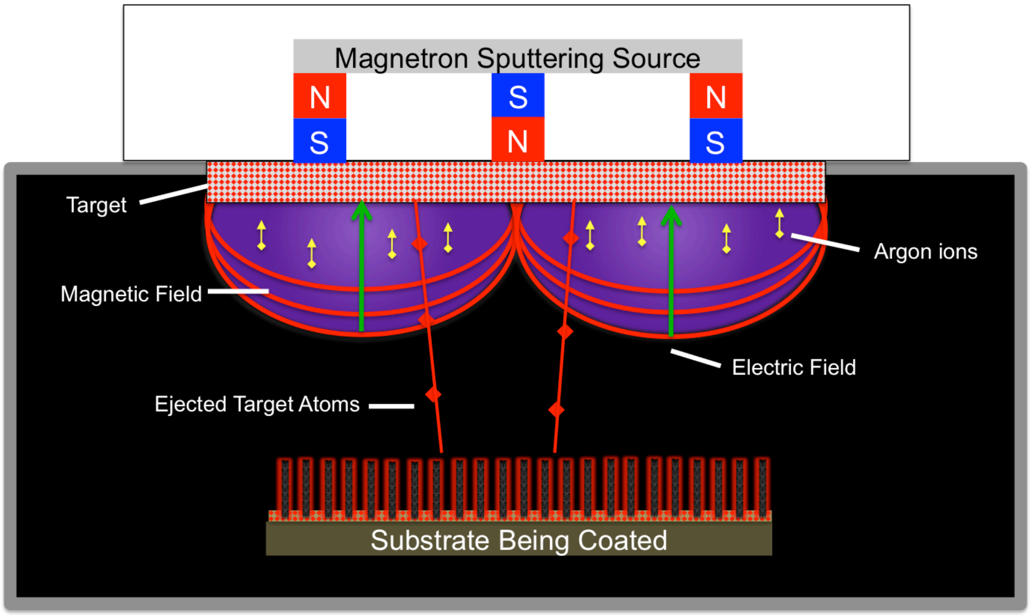

Figure 2.5 – Illustration of a magnetron sputtering deposition systems similar to that of the Perkin Elmer 4400 series with target above the VACNF substrate.

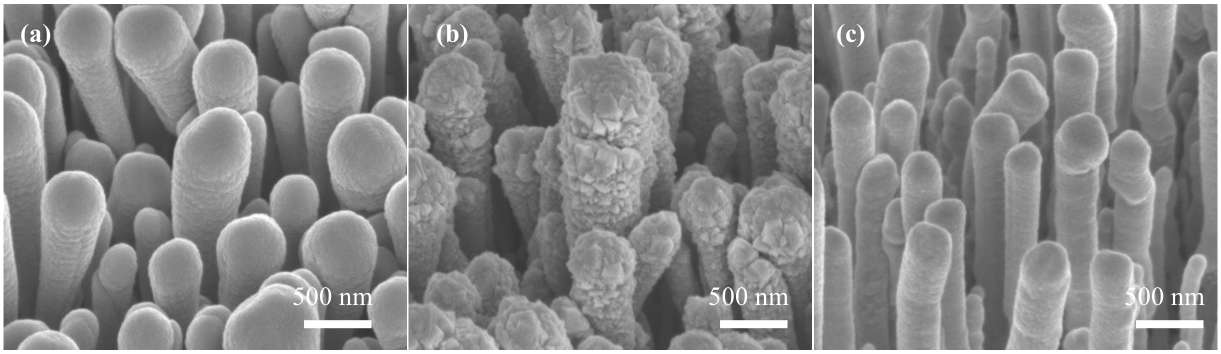

Figure 2.6 – SEM images of (a) Si-coated VACNF array, (b) TiO_2-coated VACNF array, and (c) Mn-coated VACNF array after deposition of shell materials.

2.3.1 Silicon and Titanium Dioxide for Lithium-ion Battery Experiments

Silicon (99.999%) and titanium oxide were deposited on VACNF arrays to form the core-shell nanowire arrays by high vacuum magnetron sputtering at UHV Sputtering Inc. (Morgan Hill, CA). Si deposition was performed under an ultra-high pure Argon atmosphere at a rate 30.0 nm/min till a nominal thickness (equivalent to the film thickness on a flat surface) of 500 nm was measured in-situ with a quartz microbalance (QCM). It was validated by SEM measurements of a Si wafer placed beside the Cu substrate during deposition (see equation 2.1). Titanium oxide deposition was performed in similar fashion, using a 50% mixture of UHP Oxygen to UHP Argon, which reactively formed TiO_2 during sputtering. At rate 3.125 nm/min, the TiO_2 deposition required two passes with a cool down period in-between passes. A constant temperature in the sputtering chamber was not maintained, but did not exceed 150°C. Even though sputtering is not a conformal deposition technique, the open structure of brush-like VACNF arrays made it possible for material to reach deep down into the array. As a result, it formed a thick coating at the CNF tip followed by a gradually thinned coaxial shell around the lower portion of the CNF, presenting an interesting tapered core-shell structure similar to a cotton swab (Figure 2.6a and 2.6b). The mass of the deposited shell coating was directly measured by two independent methods. First, in situ QCM was used to measure the Si and TiO_2 mass during deposition with magnetron sputtering to control the desired thickness. Magnetron sputtering is a reliable process that can uniformly deposit materials over a large area of 16” in diameter. The Cu disks with VACNFs and the QCM are placed within this area and should have received the same amount of material deposition. Second, a more precise mass was determined by examining the thickness of the sputtered material on a flat Si(100) wafer that was placed next to the Cu disks. Due to the uniform deposition, the area-specific amount of material sputtered onto the VACNFs on Cu disks should be the same as in the area next to them. Thus nominal thickness is used to represent the area-specific amount of Si or TiO_2 deposited on VACNFs on Cu. The nanostructure only affects how the material is distributed within an area but does not alter the total quantity in this area.

For a Si layer with 456 nm nominal thickness and density of 2.33 g/cm^3, the mass per electrode (~17.5 mm in dia.):

$$\text{Si Mass} = (4.56\times10^{-5}\text{cm}) * 3.14 * (1.75/2\text{ cm})^2 * 2.33\text{ g/cm}^3 = 2.55\times10^{-4}\text{ g} \qquad (2.1)$$

For a TiO_2 layer with 500 nm nominal thickness and density of 3.50 g/cm^3, the mass per electrode:

$$\text{TiO}_2\text{ Mass} = (5.00\times10^{-5}\text{cm}) * 3.14 * (1.75/2\text{ cm})^2 * 3.50\text{ g/cm}^3 = 4.19\times10^{-4}\text{ g} \qquad (2.2)$$

2.3.2 Manganese for Pseudocapacitor Experiment

Pure Mn (99.95%) was deposited on VACNF arrays using a custom built sputtering chamber. The substrate was mounted in an on-axis configuration relative to the sputtering gun. Before Mn deposition, the chamber was flushed with UHP N_2 gas and then pumped down to a base pressure of ~10^{-6} Torr. It was then filled with UHP Ar gas to a pressure of approximately 20 mTorr. Sputtering was conducted at room temperature with a power of 48 W and at a rate of

0.67 nm s^{-1} as determined by profilometry (KLA Tencor P-16 Profiler). The nominal thicknesses of Mn were controlled to thicknesses of 50, 100, 200, 300, and 600 nm, which were validated with SEM by measurement of the cross-section of the Mn films deposited on reference Ti foils. For a MnO_2 layer with 100 nm nominal thickness and density of 5.026 g/cm^3, the mass per electrode (~13.3 mm in dia.):

$$MnO_2 \text{ Mass} = (1.00\times10^{-5} \text{ cm}) * 3.14 * (1.33/2 \text{ cm})^2 * 5.026 \text{ g/cm}^3 = 4.19\times10^{-4} \text{ g} \qquad (2.3)$$

As shown in Figure 2.5, the coaxial coating on all three materials show excellent stability in binding to the CNF.

Chapter 3 - High-Performance Lithium-ion Battery Anode Based on Core-Shell Heterostructure of Silicon-coated Vertically Aligned Carbon Nanofibers

Reproduced with permission from The Royal Society of Chemistry from S. A. Klankowski, R. A. Rojeski, B. A. Cruden, J. Liu, J. Wu and J. Li, Journal of Materials Chemistry A, 2013, 1, 1055. DOI: 10.1039/C2TA00057A

3.1 Introduction

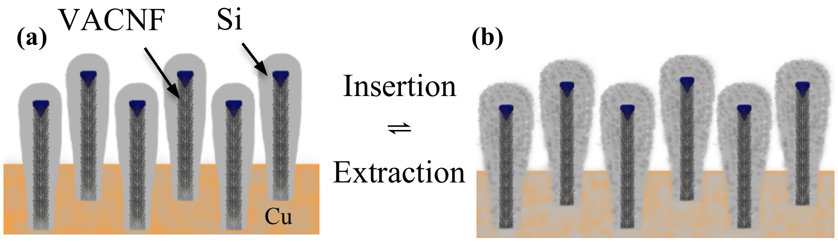

Figure 3.1 - Schematic illustration of the reversible structural changes in the coaxially coated Si on VACNFs in (a) extracted (discharged) and (b) inserted (charged) states during half-cell tests.

Here we report on an approach to fabricating hybrid core-shell NW architecture as a high-performance Li-ion anode by utilizing the vertically aligned carbon nanofiber (VACNF) arrays on Cu foil to support coaxially coated Si shells, as illustrated in Figure 3.1. As summarized in Chapter 2, VACNFs are a special type of MWCNTs grown by PECVD, which causes them to be aligned vertically on the substrate surface and remain well separated from each other, forming an untangled brush-like structure. The easily accessible open space from above allowed Si to be coated onto each carbon nanofiber (CNF) and form rather uniform coaxial shells over the whole sample.[79, 81, 85]

Besides efficient electrical connection to the Si shell, this structure can effectively accommodate the volume expansion/contraction of Si in the radial direction during charge-discharge cycles. The short path of Li^+ transport across the thin Si shell allows much higher charge-discharge rate and significantly improved power density. In this chapter, we demonstrate that the Si material in this core-shell NW structure is fully active, providing high Li^+ storage capacity in the range of 3000 to 3650 mAh $(g_{Si})^{-1}$, even at a C/1 rate. Furthermore, the capacity is retained at this level for over 100 charge-discharge cycles. The charge-discharge rate, the corresponding capacity, and cycle stability are all significantly improved from previous reports on anode materials based on Si NWs and hybrid Si-C nanostructures.[24, 43, 44, 100]

3.2 Experimental Details

3.2.1 VACNF Growth and Silicon Deposition

Following the generalized procedures in Chapter 2, VACNF arrays were grown on Cu foils to a length of 3.0 μm long and sputtered with pure Si to a nominal thickness of 0.5 μm. For comparison, VACNFs were also grown to a length of 10 μm long and sputtered with Si to three separate nominal thicknesses: 0.5 μm, 1.5 μm, and 4.0 μm.

3.2.2 Electrochemical Cell Assembly and Charge-Discharge Tests

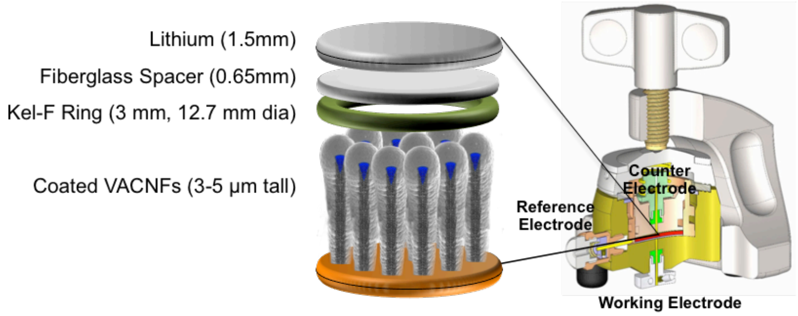

Figure 3.2 – Diagram of El-Cell three-electrode electrochemical test fixture and electrode stack. A fiberglass spacer and a Kel-F ring that helps to protect the coated CNFs from collapse separate the Si-coated VACNF electrode and lithium counter electrode. A small punch of Li metal acts as reference electrode.

A reusable electrochemical cell (El-Cell, Hamburg Germany) with three-electrode design (Figure 3.2) was used for the half-cell tests. The Cu disks covered with VACNFs (with or without further Si coating) were used as the working electrode against an 18 mm diameter lithium disk (1.5 mm in thickness) as the counter electrode. A lithium wire was used as the reference electrode. A polyethylene spacer (0.65 mm in thickness) was placed between the working and counter electrodes. A Kel-F ring (18 mm outer dia., 3.0 mm thick) with one side machined into a wedged shape was used to separate the working electrode from the polyethylene spacer so that the vertical nanowires were not compressed. The exposed working electrode area was 17.5 mm in diameter. The cell was assembled in an argon-filled dry-box (Mbraun LabStar50). The electrolyte consisted of 1.0 M lithium hexafluorophosphate ($LiPF_6$) in a mixture of 1:1:1 volume ratio of ethylene carbonate (EC), ethyl methyl carbonate (EMC) and dimethyl carbonate (DMC) plus 2% vinylene carbonate (Novolyte, Ohio). Before testing, the electrolyte was injected by a syringe through a 0.30-mm dia. hole to fill between the electrodes. A small punch of pure lithium was then pressed into the hole to make direct contact with the electrolyte and served as the reference electrode. Cyclic voltammetry (CV) and galvanostatic charge-discharge cycles were performed using a PARStat 2273 potentiostat controlled by PowerSuite Software (Princeton Applied Research, OakRidge, TN), a CHI760D potentiostat controlled by CHI Electrochemical Software (CH Instruments, Austin, TX), and a MTI 8 channel battery analyzer (MTI Corporation, Richmond, CA). Additional half-cell tests of the 10-μm long VACNF arrays were performed by cutting the 50.8 mm x 50.8 mm samples to appropriate size for a 2032 button cell. CV and galvanostatic charge-discharge measurements of these samples were performed with an Arbin battery testing system (College Station, TX.)

3.2.3 Microscopy and Spectroscopy Characterization

Both the as-prepared electrodes and those disassembled from the cells after Li-ion half-cell tests were stored and transferred in air before inspection with SEM (FEI Nano430). Some bare VACNFs and Si-coated VACNFs were scraped off from the Cu substrate, suspended in isopropanol by gentle stirring and then casted onto carbon film coated Cu grids for transmission electron microscopy (TEM) (FEI Tecnai F20 XT) measurements. Raman spectroscopy measurements were carried out with a Raman microscope (Thermo Scientific DXR system) with a 10X 0.25NA objective and a 532 nm laser at 5 mW power.

3.3 Results and Discussion

3.3.1 Structural Characterization of Silicon-coated VACNF Anode

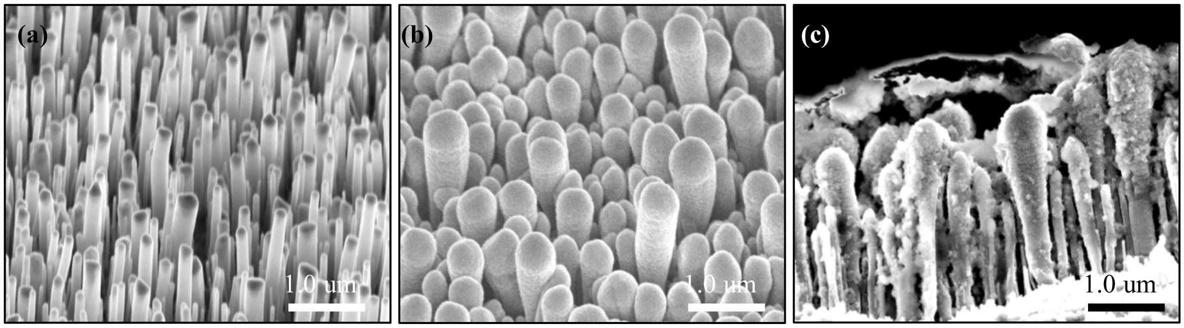

Figure 3.3 - SEM images of (a) an "as-grown" VACNF array with an average length of 3 μm, (b) Si-coated VACNF at the nominal thickness of 0.50 μm, and (c) the Si-coated VACNF array in the extracted (discharged) state after 100 charge-discharge cycles. (a) and (b) are 45° perspective views and (c) is the cross-sectional view. All scale bars are 1.0 μm.

Figure 3.3 shows the SEM images of an "as-grown" VACNF array on a Cu foil, the VACNF array coated with a layer of Si, and the Si-coated VACNF array in the extracted (discharged) state after experiencing 100 lithium insertion-extraction (or charge-discharge) cycles, respectively. In the "as-grown" sample (Figure 3.3a), CNFs were firmly attached to the Cu surface with uniform vertical alignment. The distribution of CNF positions was random but overall the sample had a reproducible areal density of 1.1×10^9 CNFs cm^{-2} (counted with top-view SEM images). This translated to an average nearest-neighbor distance of ~330 nm. The average length of the CNFs in Figure 3.3 was ~3.0 μm with >90% of CNFs in the range of 2.5 to 3.5 μm in length. The diameter spread from ~80 nm to 240 nm with an average of ~147 nm, as shown in the histogram in Figure 2.4. An inverse teardrop shaped Ni catalyst particle for CNF growth presents at the tip of each CNF and caps the hollow central channel. The size of the Ni catalyst particle is known to define the diameter of the CNF.[79, 81, 85] In addition, it has been reported that nickel does not react with Li.[24]

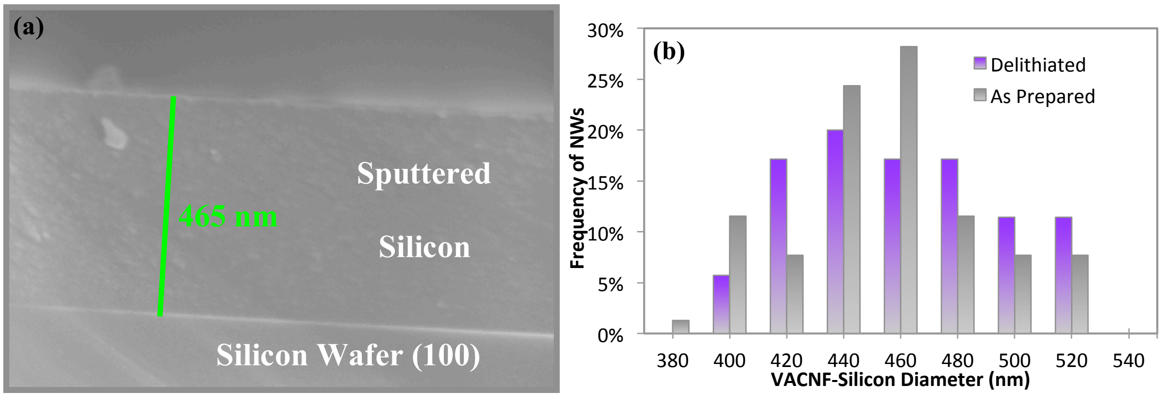

Figure 3.4 – (a) SEM image of the cross section of a Si wafer after sputtering ~465 nm Si. (b) Histogram of the diameter distribution of Si-coated VACNF array sputtered with 0.50 µm nominal Si thickness in the "as-prepared" state (grey) and in the delithiated (discharged) state after 100 charge-discharge cycles (purple). The vertical axis is the percentage of appearance within the discrete diameter ranges.

After magnetron sputtering, it formed a thick Si coating at the VACNF tip and a gradually thinned coaxial Si shell moving down the CNF, presenting a tapered core-shell structure similar to a cotton swab. In this chapter, the total amount of Si deposited onto the VACNFs was represented by the nominal thickness equivalent to the Si films onto a flat surface, which was measured with a QCM and was further validated with cross-sectional SEM measurements of a Si wafer placed at side of the Cu substrate during deposition. At 0.50 mm nominal thickness, the Si-coated VACNFs remained well-separated from each other, presenting an open core-shell NW array structure as shown in Figure 3.3b, which allows the electrolyte to freely access the entire Si surface. The average tip diameter was ~457 nm, much bigger the ~147 nm average diameter of "as-grown" VACNFs (see Figure 3.4). Thus the average radial Si thickness at the tip was estimated to be ~155 nm. It was apparently much smaller than the 0.50

μm nominal Si thickness since Si was spread along the full length of VACNFs. The cross-sectional SEM image in Figure 3.3c indicates that the Si shell covers the whole CNF length.

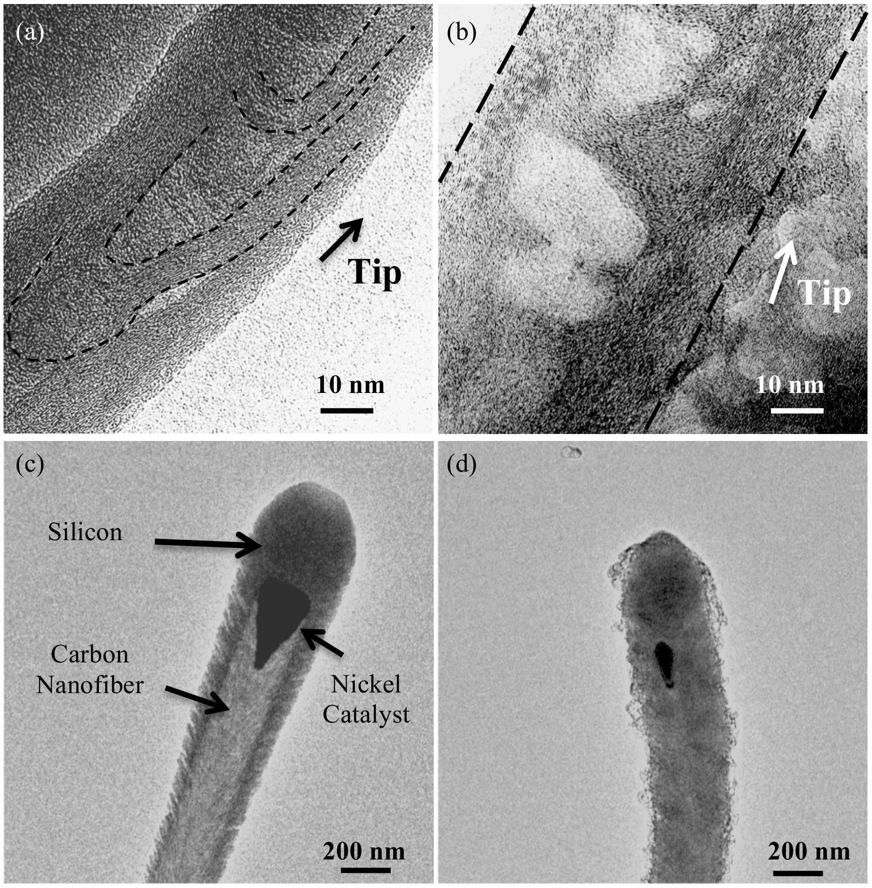

Figure 3.5 – TEM images of "as-grown" VACNFs before (a) and after (b) lithium intercalation/extraction cycles in the delithiated (discharged) state. The thin dashed lines in (a) are visual guidance of the stack of cup-like graphitic layers inside the VACNFs. The long dashed lines represent the sidewall surface of the CNF. Scale bar for (a-b) is 10 nm. Images (c) Si-coated VACNF with Si of 500 nm nominal thickness in the `and (d) a Si-coated VACNF in the delithiated (discharged) state after lithium insertion/extraction cycles. The CNFs in each TEM measurement were randomly picked for representing the physical effects of the processes, but not for directly comparing the sizes. Scale bar for (c-d) is 200 nm.

The TEM images in Figure 3.5 further illustrate the detailed structure of the "as-grown" and Si-coated VACNFs before and after charge-discharge cycles as Li-ion anodes. As discussed earlier, these PECVD grown VACNFs have a unique interior microstructure distinct from the concentric tube structure of ordinary MWCNTs or the solid fibrous structure of pyrolyzed carbon nanofibers in other studies.[43, 44] One of the most prominent characteristics is that these CNFs consist of a series of bamboo-like nodes across the mostly hollow central channel. The TEM image in Figure 3.5a indicates that these nodes are consisted of a stack of 5-15 cup-like graphitic layers, consistent with what has been reported in literature.[81, 85] The resolution and contrast was limited by the large CNF diameter (mostly between 100 to 200 nm) in this study. The large diameter, however, is beneficial in ensuring that the CNFs are mechanically robust and able to retain the vertical array structure through Si deposition and wet electrochemical tests. The cup-stacking graphitic structure of the VACNF is schematically illustrated in Figure 2.1b. The unique microstructure and brush-like configuration are key differences between this study and other nanostructured carbon materials in literature.[43, 44, 100] It is noteworthy that the VACNF has relatively high electrical conductivity (up to ~2.5×10^5 S/m) along the axis and is known to form stable Ohmic contact with the conductive substrate.[84]

In Figure 3.5c, about 390 nm thick Si was observed on top of the tip of a ~210 nm diameter VACNF, forming a cotton-swab-shaped shell. The largest portion was ~430 nm in diameter near the very end of the CNF tip. The tapered Si shell extended over the whole length of the CNF. The coaxial Si shell below the CNF tip showed a feather-like texture with modulated contrast, different from the uniform Si deposits above the tip. This might be related to the broken graphitic edges along the sidewall of the PECVD-grown VACNFs as observed in our previous studies[101, 102] and other literature.[79, 81, 103] The broken graphitic edges may be critical in forming a good interface between the VACNF core and the Si shell to facilitate fast electron transfer.

3.3.2 Lithium-ion Intercalation and Extraction in "As-Grown" VACNF Electrodes

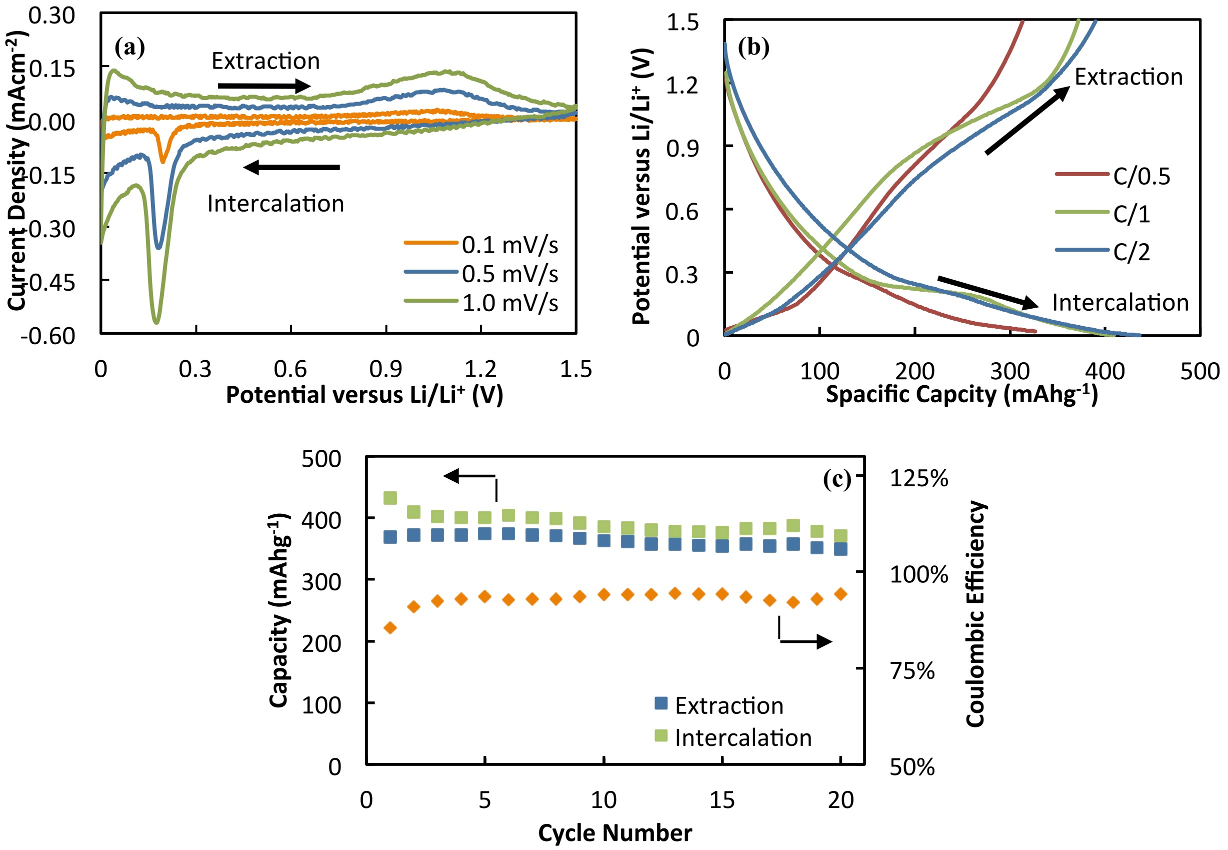

Figure 3.6 – Characterization of lithium intercalation and extraction of "as-grown" 3.0-μm long VACNFs. (a) Cyclic voltammograms from 1.5 V to 0.001 V versus a Li/Li$^+$ reference electrode at 0.1, 0.5 and 1.0 mV s^{-1} scan rates. A lithium disk was used as the counter electrode. All data were taken from the second cycle and normalized to the exposed geometric surface area. (b) The galvanostatic charge-discharge profiles at C/0.5, C/1 and C/2 power rates, corresponding to current densities of 647, 323, and 162 mA g^{-1} (normalized to estimated carbon mass) or 71.0, 35.5, and 17.8 μA cm^{-2} (normalized to the geometric surface area), respectively. (c) Intercalation and extraction capacities (left vertical axis) and Coulombic efficiency (right vertical axis) versus the cycle number at C/1 charge-discharge rate.

The cup-stacking graphitic structure of VACNFs allows Li$^+$ intercalation into the graphitic layers at the sidewall. The Li$^+$ transport path across the CNF wall is very short (~290 nm), quite different from the long path from the open ends in commonly used seamless carbon nanotubes (CNTs). Indeed, the electrochemical characterization in Figure 3.6 illustrated such phenomenon. A freshly assembled half-cell typically showed the open circuit potential (OCP) of the “as-grown” VACNF anode was ~2.50-3.00 V vs. Li/Li^+ reference electrode. The CVs measured between 0.001 V and 1.50 V show that Li^+ intercalation starts as the electropotential is below 1.20 V. The first cycle from OCP to 0.001V involved the formation of a necessary protective layer, i.e. the solid electrolyte interphase (SEI), by the decomposition of solvent, salts, and impurities,[104-107] and thus presented a large cathodic current. Subsequent CVs showed smaller but more stable currents. The cathodic current associated with Li^+ intercalation rose slowly as the electrode potential was swept to negative until a sharp cathodic peak appeared at 0.18 V. As the electrode potential was reversed to positive after reaching to the low limit at 0.001 V, lithium extraction was observed in the whole range up to 1.50 V, indicated by the continuous anodic current and a broad peak at 1.06 V.

The CV features of VACNF arrays were somewhat different from those of staged intercalation into graphite[31, 32] and slow Li^+ diffusion into the hollow channel of CNTs[33]. Li-ion insertion into VACNFs is likely through intercalation between graphitic layers from the sidewall due to its unique structure. Interestingly, the TEM image in Figure 3.5b indicates that the graphitic stacks in the bamboo-like nodes inside the CNF seem to be disrupted during Li^+ intercalation/extraction cycles, possibly due to large volume change. Some debris and nanoparticles were left inside CNFs as well as at the exterior surface.

The galvanostatic charge-discharge profiles in Figure 3.6b showed that the Li^+ storage capacity decreased as the power rate was increased from C/2 to C/0.5 (also referred to as “2C”). To make it easier to compare the rates (particularly for those higher than C/1), we use the fractional notation C/0.5 in this chapter instead of “2C” that is more popularly used in literature. The Li^+ intercalation and extraction capacities were normalized to the estimated mass of the CNFs (~1.1×10^{-4} g cm^{-2}) that was calculated based on a hollow VACNF structure with the following average parameters: length (3.0 mm), density ($1.1x10^9$ CNFs cm^{-2}), outer diameter (147 nm), and hollow inner diameter (49 nm, ~1/3 of the outer diameter). The density of the solid graphitic wall of the VACNFs was assumed to be the same as graphite (2.2 g cm^{-3}).[108] At the normal C/2 rate, the intercalation capacity was 430 mAh g^{-1} and the extraction capacity is 390 mAh g^{-1}, both of which are slightly higher than the theoretical value of 372 mAh g^{-1} for graphite,[109] which may be attributed to SEI formation and the irreversible Li^+ insertion into the hollow compartments inside the VACNFs. But the uncertainty in mass estimation does not allow a firm conclusion at this stage. The extraction capacities were found to be more than 90% of the intercalation values at all power rates and both of the intercalation and extraction capacities decreased by ~9% as the power rate increased from C/2 to C/1 and by ~20% from C/1 to C/0.5, comparable to graphite anodes.

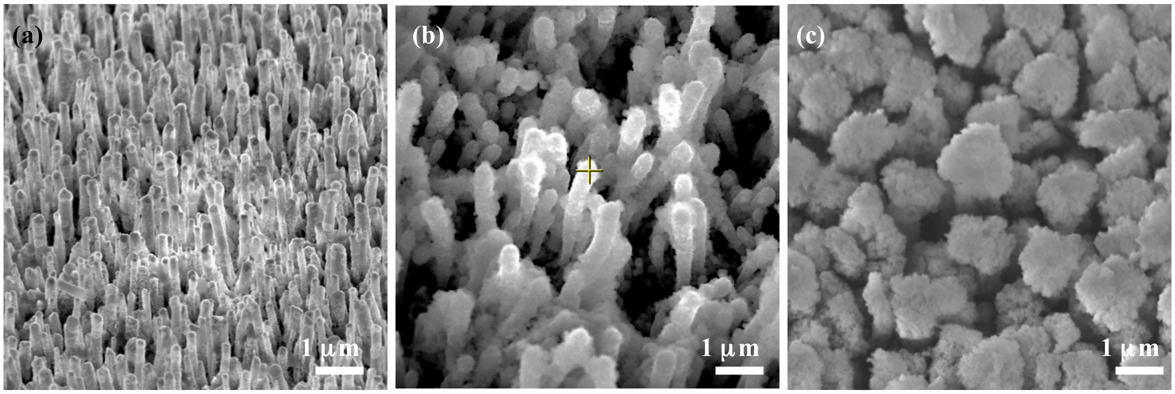

Figure 3.7 – SEM images of (a) 3.0 µm long VACNFs in the delithiated state after cycling, and Si-coated VACNF core-shell NW arrays after 100 cycles in the (b) delithiated state (c) lithiated state. All images are 45° perspective views. All scale bars are 1 µm.

Upon charge-discharge cycling, the intercalation capacity was found to slightly drop from 410 mAh g^{-1} to 370 mAh g^{-1} after 20 cycles at C/1 rate, while the extraction capacity maintained between 375 to 355 mAh g^{-1}. The overall Coulombic efficiency (i.e. the ratio of extraction capacity to intercalation capacity) was ~94%, except in the first two cycles due to SEI formation on the CNF surface. The SEI film is known to form readily on carbonaceous anodes during the initial cycles, which allows lithium-ion diffusion but is electrically insulating, leading to an increase in series resistance.[107] The TEM image (Figure 3.5b) and SEM image (Figure 3.7a) show that a non-uniform thin film was deposited on the CNF surface during charge-discharge cycles. The SEI may actually serve as a sheath to increase the mechanical strength of the VACNFs, preventing them from collapsing into microbundles by the cohesive capillary force of solvent as observed in the study with other polymer coatings.[110]

The most exciting results were obtained with the Si-coated VACNF core-shell NW array as Li-ion battery anodes shown in Figure 3.8. The CVs in Figure 3.8a present very similar features to that of Si NWs.[24] Comparing to the "as-grown" VACNF array, both of the cathodic wave for Li^+ insertion and the anodic wave for Li^+ extraction shift to lower values (below ~0.5 and 0.7 V, respectively). The peak current density increases by 10 to 30 times after Si coating and is directly proportional to the scan rate. Clearly, alloy-forming Li^+ insertion into Si is much faster than intercalation into VACNFs that was limited by the slow diffusion of Li^+ between graphitic layers. The cathodic peak at ~0.28 V was not observed in the previous study on pure Si NWs.[24] The three anodic peaks representing the transformation of Li-Si alloy into amorphous Si are similar to those with Si NWs[111] despite shifting to lower potentials by 100 to 200 mV.

3.3.3 Lithium-ion Insertion and Extraction in Silicon-coated VACNF Core-Shell Nanowire Electrodes

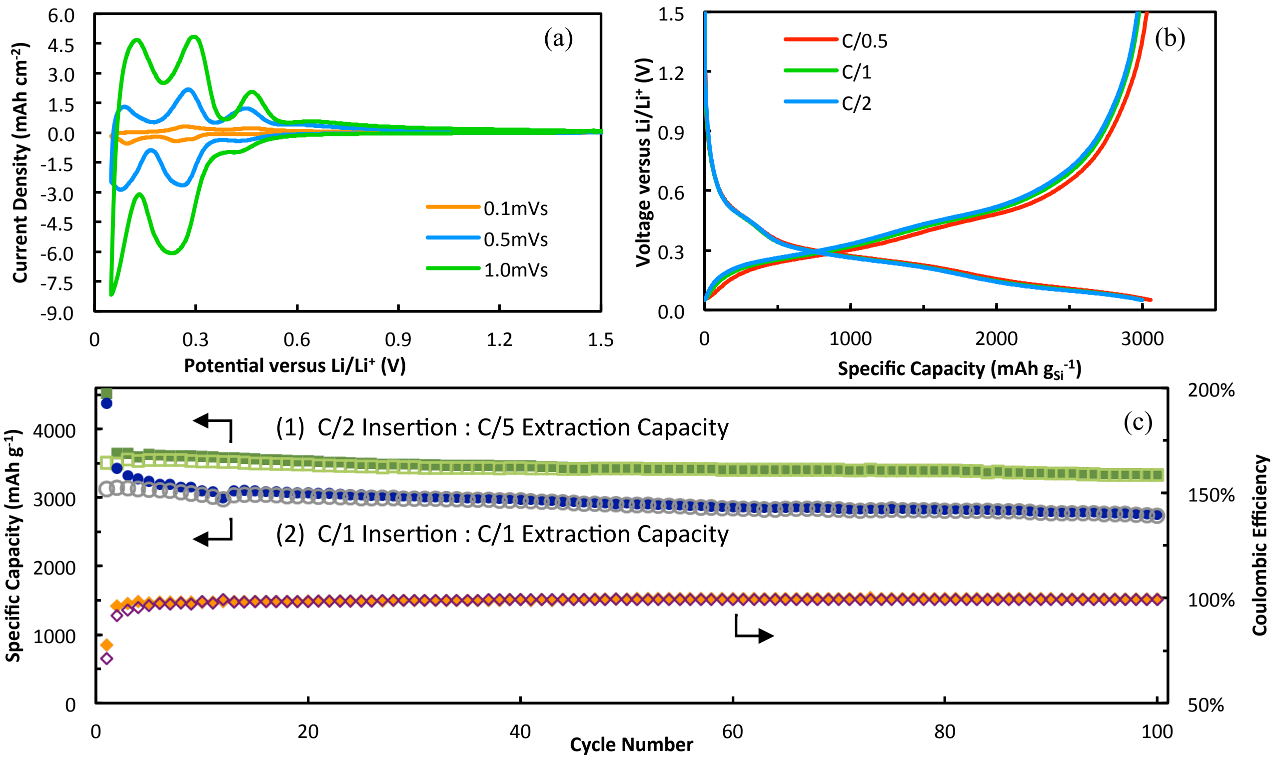

Figure 3.8 – Electrochemical characterization of lithium insertion and extraction of Si-coated 3.0-μm long VACNFs at the nominal Si thickness of 0.50 μm. (a) Cyclic voltammograms between 1.5 V and 0.05 V versus Li/Li$^+$ at 0.10, 0.50 and 1.0 mV s^{-1} scan rates. The measurements were made after 150 charge-discharge cycles and the data of the second cycle at each scan rate are shown. (b) The galvanostatic charge-discharge profiles at C/0.5, C/1 and C/2 power rates after 120 cycles. All profiles were taken from the second cycle at each rate. (c) Insertion and extraction capacities (left vertical axis) and Coulombic efficiency (right vertical axis) of two electrodes versus the charge-discharge cycle number. The first electrode was first conditioned with one cycle at C/10 rate, one cycle at C/5 rate, and two cycles at C/2 rate. It was then tested at C/2 insertion rate and C/5 extraction rate for 96 cycles. The filled and open green squares represent the insertion and extraction capacities, respectively. The second electrode was first conditioned with two cycles each at C/10, C/5, C/2, C/1, C/0.5 and C/0.2 rates. It was then tested at C/1 rate for 88 cycles. The filled and open blue circles represent the insertion and extraction capacities, respectively. Coulombic efficiencies of both electrodes are represented by filled (1st electrode) and open (2nd electrode) diamonds, which mostly overlap at 99%.

The galvanostatic charge-discharge profiles of Si-coated VACNF core-shell NW array (Figure 3.8b) showed two remarkable features: (1) high Li$^+$ insertion (charge) and extraction (discharge) capacity of ~3000 mAh $(g_{Si})^{-1}$ was obtained at C/2 rate even after 120 cycles; and (2) the Li^+ capacity was nearly the same at C/2, C/1, and C/0.5 power rates. The total Li^+ storage capacity after Si deposition is about 10 times of that of "as-grown" VACNFs even though the low potential limit for charging cycle was increased from 0.001 V to 0.050 V. As a result, the amount of Li^+ intercalation into the VACNF core was negligible. The specific capacity was calculated by dividing only the mass of Si that was calculated from the measured nominal thickness and the bulk density of 2.33 g/cm^3. This method was chosen as an appropriate metric to compare the specific capacity of the Si shell to the theoretical value of bulk Si. For the 3.0-mm long VACNF arrays deposited with Si of 0.456 mm nominal thickness, the areal mass density of Si coating was ~1.06×10^{-4} g/cm^2, comparable with that of VACNFs (~1.1×10^{-4} g/cm^2). The corresponding Coulombic efficiency in Figure 3.8b is greater than 99% at all three power rates, much higher than that of the "as-grown" VACNFs.

Both the CVs and charge-discharge measurements indicated that the Li^+ insertion into the Si shell was fast and highly reversible, which are desired for high-performance Li-ion battery anodes. This was further demonstrated with two long cycling tests on two identical samples at different testing conditions: (1) slow asymmetric tests with C/2 rate for insertion and C/5 rate for extraction; and (2) fast symmetric test at C/1 rate for both insertion and extraction. Both sets of data showed >98% Coulombic efficiency over the long cycling except for the initial conditioning cycles (4 cycles in the former and 12 cycles in the latter at varied low rates). In the slow asymmetric tests, the insertion capacity only dropped by 8.3% from 3643 mAh g^{-1} at the 5th cycle to 3341 mAh g^{-1} at the 100th cycle. Even at the fast C/1 charge-discharge rate, the insertion capacity only drops by 11% from 3096 mAh g^{-1} at the 13th cycle to 2752 mAh g^{-1} at the 100th cycle. The difference in the Li^+ capacity between these two sets of data was mostly attributed to the initial conditioning parameters and small sample-to-sample variations. This was indicated by the similar values of insertion/extraction capacity during the first few conditioning cycles in Figure 3.8c at C/10 and C/5 rates. The fast rates (C/0.5 for 9th and 10th cycles and C/0.2 for 11th and 12th cycles in sample #2) were found to be harmful and caused irreversible drop in the capacity. However, the electrode became stabilized after long cycling. As shown in Figure 3.8b, the charge-discharge profiles are almost identical at C/2, C/1, and C/0.5 rates, which were measured with sample #1 after going through 120 cycles. To our knowledge, such remarkable cycle stability and high-rate capability are only attainable with ultrathin (<50 nm) Si films.[33]

The specific capacity of the Si shell in the range of 3000 to 3650 mAh g^{-1} is consistent with the highest values of amorphous Si anodes summarized in the comprehensive review by Szczech and Jin.[112] It is remarkable that the entire Si shell in the VACNF-Si core-shell NW array was active for Li^+ insertion and remained nearly 90% of the capacity over 120 cycles, which to our knowledge has not been achieved before except with ultrathin (<50 nm) Si films.[33] The specific capacity obtained in this study is significantly higher than those using other nanostructured Si materials at the similar power rates, including ~2500 mAh g^{-1} at C/2 rate and ~2200 mAh g^{-1} at C/1 rate with Si NWs,[24] and ~800 mAh g^{-1} at C/1 rate with randomly oriented carbon nanofiber-Si core-shell NWs.[43] Clearly, the coaxial core-shell NW structure on well-separated VACNFs provides an enhanced charge-discharge rate, nearly full Li^+ storage capacity of Si, and a long cycle life. The more uniform Si shell and better electrical interface with the VACNFs may be the key for the enhanced performance. As shown in Figure 3.8c, an anomalously high insertion capacity (~4500 mAh g^{-1}) was always observed in the initial cycles, which was 20-30% higher than later ones. In contrast, the extraction values were relatively stable over all cycles. The extra insertion capacity can be attributed to the combination of three irreversible reactions: (1) the formation of a thin SEI layer (of tens of nanometers);[112-114] (2)

reactions of Li with SiO_x presented on the Si surface ($SiO_x + 2xLi \rightarrow Si + xLi_2O$);[46] and (3) the conversion of the starting crystalline Si coating with higher theoretical capacity (~4200 mAh g^{-1}) into amorphous Si with lower capacity (<3800 mAh g^{-1}).[112] The TEM image (Figure 3.5d) and SEM image (Figure 3.7b) showed that a non-uniform SEI might have been deposited on the surface of Si shell after the charge-discharge cycles. This elastic SEI film likely helped to retain the Si shell on the VACNF surface as it went through the large volume expansion/contraction cycles. The dramatic difference between the SEM images in Figures 3.7b-c indicates the large expansion of the Si shell in the lithiated (charged) state as the electrochemical cell was dissembled, although some of the expansion may be due to later oxidation of Li by the air.

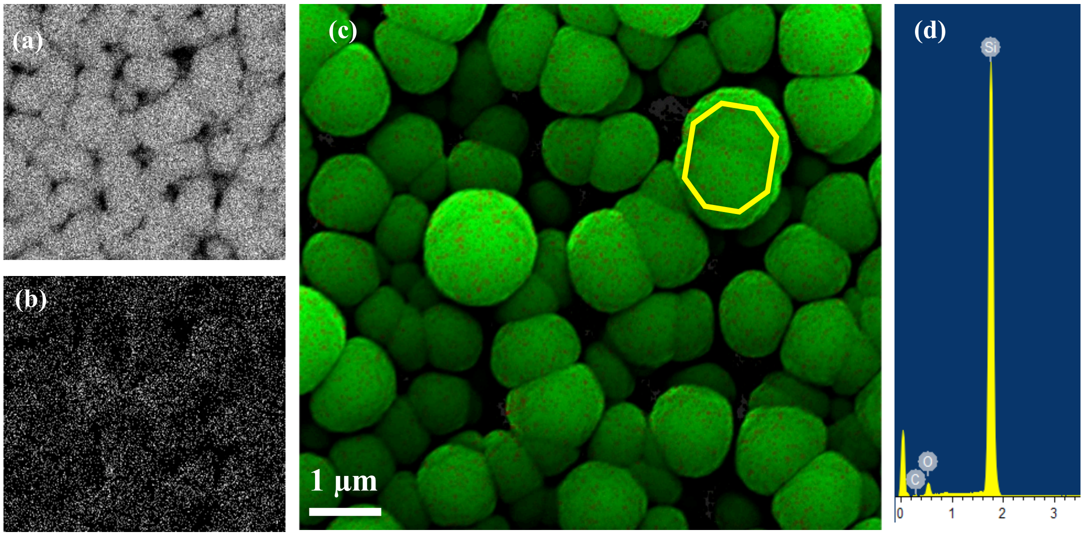

Figure 3.9 – Energy Dispersive X-ray Spectroscopy (EDS) showing composition mapping of (a) silicon, (b) oxygen, and (c) both silicon (green) and oxygen (red), on a 3.0 µm long VACNF array coated with Si of 1.5 µm nominal thickness. The sample was transported and stored in ambient conditions for about one month before the EDS measurements. (d) The EDS spectrum of the area circled by the yellow octagon in (c) indicates the oxygen to silicon atomic ratio of ~0.22:1. Some carbon signal was also observed from the beneath carbon nanofiber core.

The energy dispersive X-ray spectroscopy (EDS) measurements in Figure 3.9 at the tip of a Si-coated VACNF array indicates that the atomic ratio of oxygen to Si was ~0.22:1 in the Si shell, which was expected since the samples were stored in the air from a few weeks to several months before the measurements.

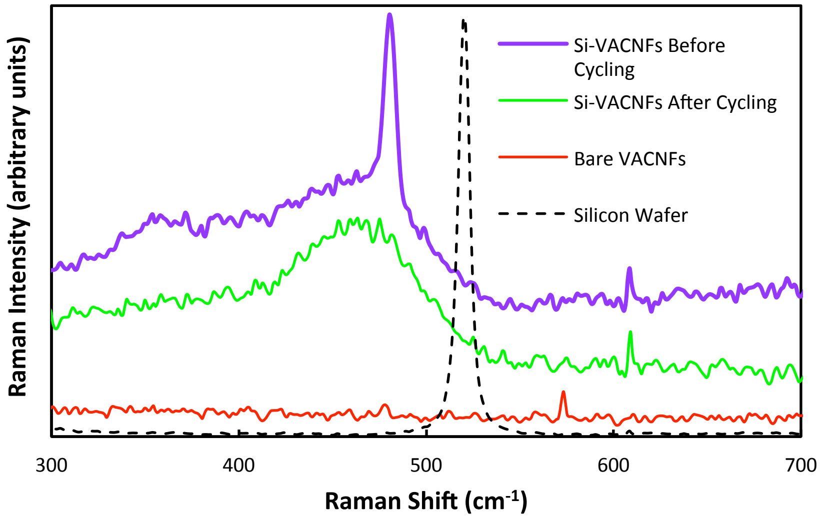

Figure 3.10 – Raman spectra of a bare VACNF array (red line) and a Si-coated VACNF array before (purple line) and after (green line) charge-discharge cycling in a Li-ion half-cell test in comparison to a reference using Si(100) wafer (black dashed line).

The crystalline and amorphous structure of the Si shell was revealed by Raman spectroscopy. As shown in Figure 3.10, the pristine Si-coated VACNF array showed multiple broad bands overlapped in the range of 350 to 550 cm^{-1} corresponding to amorphous Si, and a much higher sharp band at 480 cm^{-1} corresponding to nanocrystalline Si.[46, 115] After charge-discharge tests, the sharp peak disappeared while the broad bands merged into a single peak at 470 cm^{-1}. The bare VACNF sample did not show any feature in this range. Interestingly, the crystalline Si peak downshifted by ~40 cm^{-1} from that measured with a single-crystalline Si(100) wafer and by ~20-30 cm^{-1} from other micro-crystalline Si materials.[46, 115] The shift was likely due to much smaller crystal size and large disorders. The original Si shell likely consisted of nanocrystals embedded in amorphous matrix associated with the feather-like TEM image in Figure 3.5c. After initial cycles, the Si nanocrystals were converted into amorphous Si, consistent with the featureless TEM image after the cycling test (see Figure 3.5d). However, the

Si shell apparently did not slide along the CNF, in contrast to the large longitudinal expansion (by up to 100%) in pure Si NWs.[24] The volume change of the Si shell during Li^+ insertion was dominated by radial expansion, while the CNF-Si interface remained intact.

3.3.4 The Effects of VACNF Length and Silicon Shell Thickness

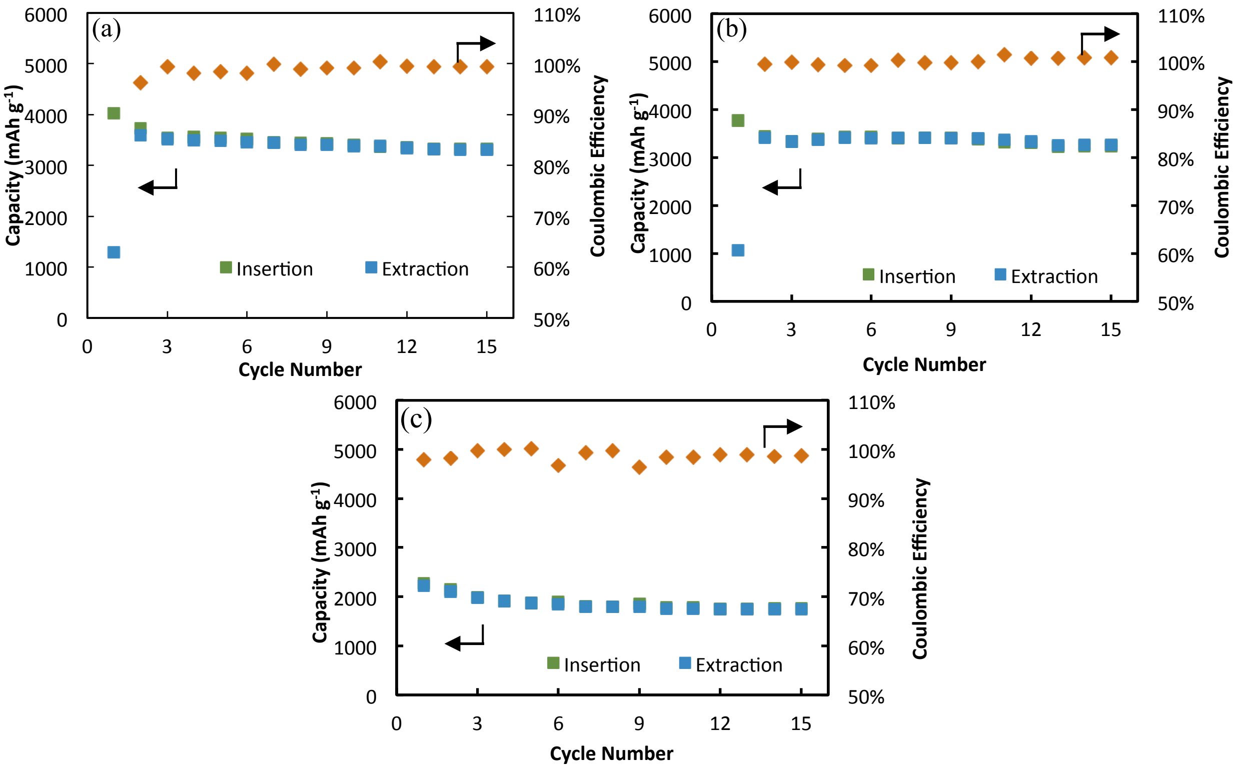

Figure 3.11 – The lithium insertion and extraction capacities and Coulombic efficiency versus the cycle number with a 10-µm long VACNF array coated with Si at varied thicknesses. The nominal Si thickness is (a) 0.5 µm, (b) 1.5 µm, and (c) 4.0 µm, respectively. The samples were first conditioned at C/10 charge-discharge rate for the first cycle, C/5 rate for the second cycle, and C/2 rate for Li+ insertion but C/5 rate for Li+ extraction in the remaining cycles.

From previous results and discussions, it is clear that the open space between the core-shell NWs is critical for high cycling stability by allowing the Si shell to freely expand/contract. Since an optimum electrode structure depends on both the VACNF length and Si shell thickness, it is always desirable to use longer VACNFs and thicker Si coatings in order to obtain higher total Li^+ storage capacity. We have found that longer VACNFs indeed improve the core-shell structure and storage capacity. Figure 3.11 shows the variation of Li^+ insertion/extraction capacities and the Coulombic efficiency over 15 charge-discharge cycles with three 10 μm long VACNF samples deposited with Si at the nominal thickness of 0.50, 1.5 and 4.0 μm, respectively. After conditioning at C/10 rate for the first cycle and C/5 rate for the second cycle, asymmetric rates (C/2 for insertion and C/5 for extraction) were used in subsequent cycles similar to the measurements of Sample #1 in Figure 3.8c. This protocol provided nearly 100% Coulombic efficiency and minimum degradation.

The specific capacities as high as 3597 mAh g^{-1} and 3416 mAh g^{-1} were obtained with 0.50 and 1.5 nm Si coating, respectively, very similar to that with 0.50 nm Si on 3.0 mm long VACNFs (see Figure 3.8c). The capacity remained nearly constant over 15 cycles. However, the electrode with 4.0 μm nominal Si thickness showed significantly lower specific capacity at only 2221 mAh g^{-1}. This indicates that, with expansion, the Si coatings from adjacent CNFs began to run into each other, limiting them from further expansion. As a result, only a fraction of the Si coating was active in lithium insertion. The cycle stability was correspondingly worse than the sample with thinner Si coatings. Interestingly, the same amount of Si (500 nm nominal thickness) on 10-mm VACNF arrays gave nearly the same amount of Li+ storage capacity (3597 mAh g^{-1}, see Figure 3.10a) as that of 3-mm VACNF arrays (3643 mAh g^{-1}, see Figure 3.7c), even though the carbon mass is more than 3 times higher. This is very strong experimental evidence that the contribution of VACNFs is negligible in calculating Li^{+} storage. It is likely that very little Li^{+} ions were intercalated into VACNFs in the Si-coated sample, which is why the core-shell structure was very stable during long charge-discharge cycles.

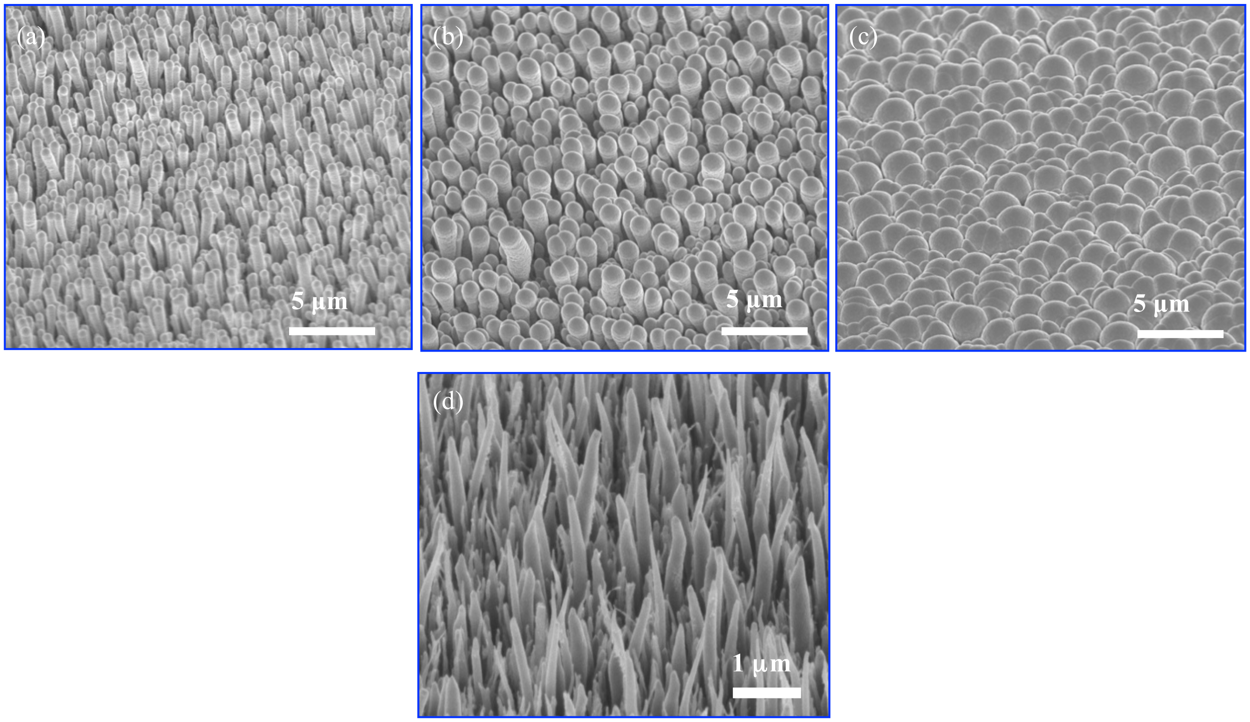

Figure 3.12 – SEM images of the freshly prepared VACNF-Si core-shell nanowire arrays (~10 µm long CNFs). The nominal Si thickness is (a) 0.50 µm, (b) 1.5 µm, and (c) 4.0 um, and (d) "as-grown" 10-mm long VACNF array. All images are 45° perspective views.

The variation of the specific Li^+ storage capacity in the three samples correlated well with their structures revealed by the SEM images in Figure 3.12. At 0.50 mm nominal Si thickness, the average tip diameter was found to be ~388 nm on the 10 mm long VACNFs, much smaller than the ~457 nm average diameter on the 3.0 mm long VACNF arrays. The Si shell was thinner but more uniformly spread along the 10-mm long VACNFs. This can be attributed to two reasons: (1) As the same amount of Si was spread over longer VACNFs, the thickness of Si shells was reduced; and (2) The structure of 10-mm VACNFs differed in some aspects from the 3-mm VACNFs. It is noted that growing 10-mm VACNF took 120 min., about six times as long as growing the 3-mm VACNFs. Some Ni catalysts were slowly etched by NH_3 during the long PECVD process, resulting in continuous reduction in Ni nanoparticle size and leading to the tapered VACNF tip (as shown in Figure 3.12d). The CNF length variation also increased in long VACNF arrays. These factors collectively reduced the shadow effects of the VACNF tip. As a result, even at 1.5-µm nominal Si thickness, the VACNF-Si core-shell NWs are well separated from each other. The SEM image of 1.5 mm Si on 10-mm VACNF arrays (Figure 3.12b) is very similar to that of 0.50 mm Si on 3.0-mm VACNF arrays, (Figure 3.3b). But as the nominal Si thickness was increased to 4.0-µm, the Si shells clearly merged with each other and filled up most of the space between the VACNFs (see Figure 3.12c). This reduced the free space needed to accommodate the volumetric expansion of the Si shell. As a result, the specific Li^+ storage capacity significantly dropped. The VACNF array with thick Si coating behaved somewhat similar to other hybrids of Si with nanostructured carbon.[43, 44, 100]

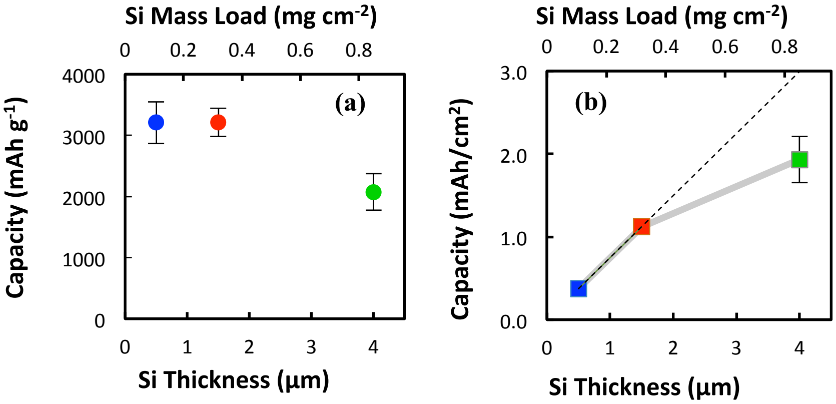

Figure 3.13 – Specific lithium insertion capacity normalized to (a) mass of Si coating and (b) geometric electrode area. The measurements were carried out with 10-µm long VACNF arrays at C/2 rate for Li^+ insertion and C/5 for Li^+ extraction. Both the nominal Si thickness (µm) and the areal Si mass load (mg cm^{-2}) on the samples are shown in horizontal axes. A total of 9 samples were measured, with three at each nominal Si thickness of 0.5, 1.5, and 4.0 µm. The dashed line in (b) represents the speculated linear relationship between the area-specific capacity and the nominal Si thickness.

The effect of Si thickness is further illustrated in Figure 3.13 which compares the mass-specific capacity (normalized to the total Si mass) and area-specific capacity (normalized to the geometric surface area of the Cu substrate) for lithium insertion with nine 10-mm VACNF samples at the three Si thicknesses. As shown in Figure 3.13a, the samples with 0.50 and 1.5 µm nominal Si thicknesses have comparable mass-specific capacities of 3208±343 and 3212±234 mAh g^{-1}, respectively. The samples with 4.0 µm nominal Si thickness give much lower capacity at 2072±298 mAh g^{-1}. Clearly, the thinner Si coatings are fully activated and provide the maximum Li insertion capacity that amorphous Si could afford. On the other hand, the area-specific capacity in Figure 3.13b increases proportionally with the Si thickness from 0.373±0.040 mAh cm^{-2} at 0.50 μm Si to 1.12±0.08 mAh cm^{-2} at 1.5 μm Si, but drops off from the linear curve to give 1.93±0.28 mAh cm^{-2} at 4.0 μm nominal Si thickness. Clearly, only a fraction of the extra Si in the thick Si coating is actively involved in Li storage. The electrochemical results are consistent with the structure shown by SEM images in Figure 3.12.

From this study, it is expected that the optimum structure for this electrode is to coat uniform thin Si shells (~200-300 nm radial thickness) on very long VACNFs (30-40 microns) with smaller diameters (~50 nm), and grown on thinner metal foils (10 microns). This remains to be a challenging research topic at this stage. We are currently investigating varying the parameters, including VACNF length, density and Si coating thickness on low-density VACNF samples, as well as more conformal deposition techniques (such as CVD, atomic layer deposition, and electrochemical deposition) for Si and other Li-ion active materials.

3.4 Conclusion

Here, we have demonstrated a high-performance hybrid lithium-ion anode material based on coaxially coated Si shells on VACNF cores. VACNF arrays are not only a good nanostructured template with excellent mechanical robustness, but also provide effective electrical interface with the entire Si shell due to the unique cup-stacking graphitic microstructure. Thick Si layers (equivalent to 1.5 μm nominal thickness on a flat surface) were deposited onto 10-μm long VACNF arrays, which can still maintain the open vertical core-shell nanowire structure with individual nanowires well separated from each other. This unique hybrid architecture allowed the Si shell to freely expand/contract in the radial direction during Li^+

insertion/extraction. High-performance Li storage with the mass-specific capacity of 3000 to 3650 mAh g^{-1} was obtained even at C/1 rate. The capacity matched the maximum value that amorphous Si could afford, indicating that the Si shell was fully active. This 3D nanostructured architecture enables effective electrical connection with bulk quantities of Si material while maintaining short Li^+ insertion/extraction path. As a result, high capacity near the theoretical limit was attained in over 120 charge-discharge cycles and there was little change as the rate was increased 20 times from C/10 to C/0.5 (or 2C). The high capacity at significantly improved power rates and the extraordinary cycle stability make this novel structure a very promising anode material for future high-performance Li-ion batteries. The same core-shell concept may be applied to cathode materials by replacing the Si shell with TiO_2, $LiCoO_2$, $LiNiO_2$, $LiMn_2O_4$, $LiFePO_4$, etc. Assembling hybrid structures using the well-defined VACNF array template is a viable approach for energy storage technologies.

Chapter 4 - Anomalous Capacity Increase at High-Rates in Lithium-ion Battery Anodes Based on Silicon-coated Vertically Aligned Carbon Nanofibers

Reprinted with permission from Elsevier from S. A. Klankowski, G. P. Pandey, B. A. Cruden, J. Liu, J. Wu, R. A. Rojeski, J. Li., Journal of Power Sources, 2015, 276, 73–79. DOI: 10.1016/j.jpowsour.2014.11.094.

4.1 Introduction

In chapter 3, we reported the fabrication and initial characterizations of core-shell NW arrays composed of a forest-like arrangement of vertically aligned carbon nanofibers (VACNFs) that were coaxially coated with intrinsic Si by magnetron sputtering. That study was concentrated on the ultra-high capacity obtained at normal power rates (C/10 to 2C). This chapter is focused on the understanding of the performance at higher rates (up to ~10C) of this core-shell NW anode, detailing how the pine-needle-textured Si shell improves the capacity retention at very high power rates, which is desirable for advanced LIB hybrids.

4.2 Experimental Details

4.2.1 VACNF Growth and Silicon Deposition

Following the generalized procedure in Chapter 2, VACNF arrays were grown on Cu foils for a longer time of 30 minutes to a reach length of ~5.0 μm long and sputtered with pure Si to a nominal thickness of 0.5 μm. Experimental conditions are the same as Chapter 3, unless noted.

4.2.2 Electrochemical Cell Assembly and Charge-Discharge Tests

A reusable electrochemical cell (El-Cell, Hamburg Germany) with three-electrode design (Figure 3.2) was used for the half-cell tests. The Cu disks covered with Si-VACNFs were used as the working electrode against an 18-mm dia. lithium disk (1.5 mm in thickness) as the counter electrode. A lithium wire was used as the reference electrode. A polyethylene spacer (0.65 mm in thickness) and a Kel-F ring (18 mm outer dia., 3.0 mm thick) was placed between the working and counter electrodes with 1.0 M lithium hexafluorophosphate ($LiPF_6$) in a mixture of 1:1:1 volume ratio of ethylene carbonate (EC), ethyl methyl carbonate (EMC) and dimethyl carbonate (DMC) plus 2% vinylene carbonate (Novelty, Ohio) as electrolyte. Cyclic voltammetry (CV) and galvanostatic charge-discharge cycles were performed using a CHI760D potentiostat controlled by CHI Electrochemical Software (CH Instruments, Austin, TX), and a MTI 8 channel battery analyzer (MTI Corporation, Richmond, CA). The charge-discharge measurements of Si-VACNF hybrids were set from 1.5 to 0.05 V vs. Li/Li^+ to minimize Li^+ intercalation into VACNF cores. Previous study (Chapter 3) has demonstrated that the contribution to the total capacity by Li^+ intercalation into VACNF core is negligible (<10%).[116] AC impedance spectroscopy was performed using a CHI 760D potentiostat controlled by CHI Electrochemical Software (CH Instruments, Austin, TX) with a 10 mV_{pp} AC potential over a frequency range from 100 kHz to 0.01 Hz. Electrochemical Impedance model fitting and simulation was performed using ZSimpWin, Version 3.1 (Princeton Applied Research, Oak Ridge, TN, USA). The outputted admittance values are listed in Tables 4.1, 4.2, and 4.3. An R(QR)WQ model (see Figure 4.6c) showed very good agreement between experimental and the calculated results with the chi-squared (χ^2) minimized below 10^{-3}. χ^2 is the function defined as the sum of the squares of the residuals.

4.2.3 Microscopy and Spectroscopy Characterization

Both the as-prepared electrodes and those disassembled from the cells after Li-ion half-cell tests were stored and transferred in air before inspection with SEM (FEI Nano430). Some Si-coated VACNFs were scraped off from the Cu substrate onto carbon film coated Cu grids for transmission electron microscopy (TEM) (FEI Tecnai F20 XT) measurements. Raman spectroscopy measurements were carried out with a Raman microscope (Thermo Scientific DXR system) with a 10X 0.25NA objective and a 532 nm laser at 5 mW power.

4.3 Results and Discussion

4.3.1 Detailed Characterization of Si-coated VACNF Anode

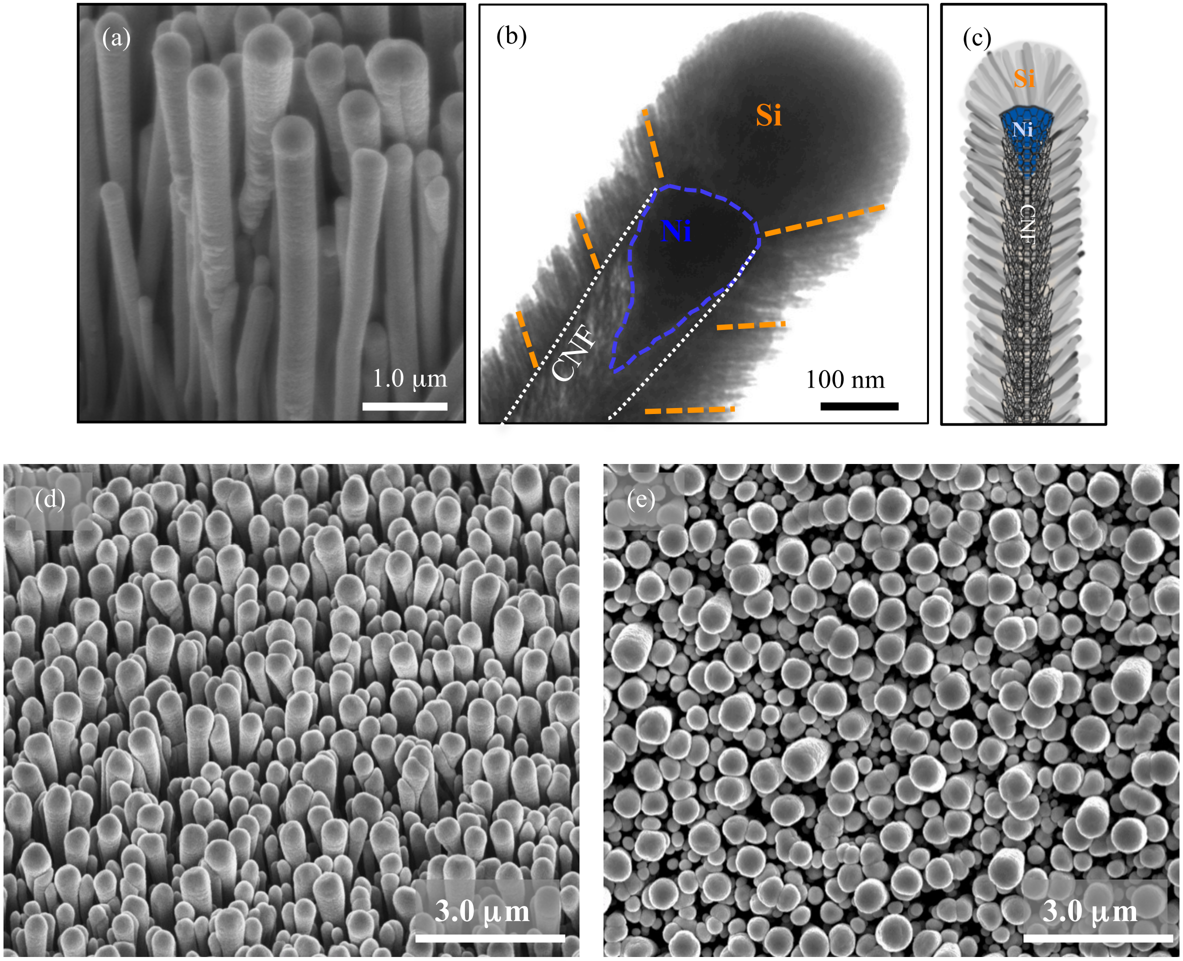

Figure 4.1 – SEM image (a) showing a landscape view of the uniform coaxial coating of Si shells on the random CNF array. TEM image (b) and schematic (c) that illustrate the nanocolumnar microstructure of Si shell and the conical graphitic stacking structure of the VACNF core. Sputtering deposition of Si created the nanocolumnar microstructure extending out from the CNF shaft (white dotted lines) at an upward oblique angle (orange dashes) while the Si at the CNF tip showing a solid amorphous feature. A Ni catalyst particle (blue dotted line) is shown at the CNF tip. SEM images (d) and (e) are representative views of the Si-coated VACNF NW arrays at 45° and 90° (top view), respectively.

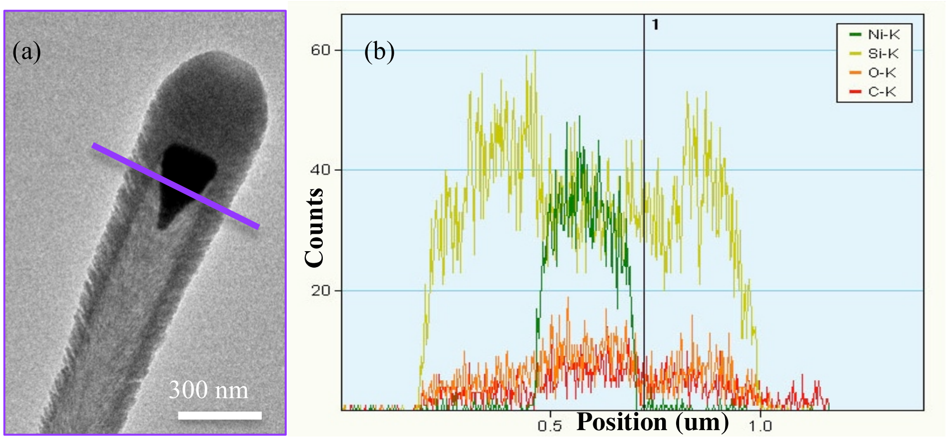

(Figure 4.2 – (a) TEM image of a Si-coated VACNF that shows the characteristic features of the CNF structure and the microstructure of the Si-coating. A cross-section elemental analysis using Energy-dispersive X-ray spectroscopy confirmed the material composition along the purple line with (b) showing signals for the Si-coating (gold line), the Ni catalyst (green line) and increased carbon presence (red line) by CNF over the continuous carbon film on the TEM grid. The presence of oxygen (orange line) due to adsorption from the air or formation of SiO_2 since the electrode was exposed to the atmosphere during handling.

At the first glance, the individual CNFs after sputter-coating with a Si layer of 500 nm nominal thickness show a cotton swab appearance, with a large Si mass at the tip that tapers gradually down the CNFs (Figure 4.1). A rough and billowy texture extends across the shell surface, representing a distinctive feature of thick sputtered films.[117, 118] More interestingly, transmission electron microscopy (TEM) revealed that the Si-coated CNFs have a unique pine-leave structure (Figure 4.1b), composed of many Si 'needles' of ~10-20 nm in diameter and 80-100 nm in length protruding from the CNF surface at an oblique upward angle. These fine structures are similar to the columnar microstructure formed in thick sputtered films on flat surfaces.[117-119] At the conditions where the substrate temperature T is much lower than the melting point T_m of the coating materials (normally with $T/T_m < 0.3$) as satisfied in this study ($T = 50–150$ °C and $T_m = 1,414$ °C for Si), the deposited materials tend to form arrays of vertical nanocolumns separated by voided open boundaries following Thornton's Structural Zone Model.[117] Such microstructure is a fundamental consequence of atomic shadowing acting in concert with the low adatom mobility at low T/T_m deposition conditions and the formation is known to be enhanced by the surface irregularities,[101] such as the broken graphitic edge at the VACNF sidewall.

It is also well known that VACNFs, grown by plasma enhanced chemical vapor deposition (PECVD), present a unique microstructure similar to a stack of graphitic cones and thus there are many graphitic edges at the sidewall as schematically illustrated in Figure 4.1c.[81] These graphitic edges are active sites facilitating fast electron transfer at the Si/CNF interface, making it distinct from the smooth but electrochemically inert graphite-basal-plane-like sidewalls of CNTs. Here the graphitic edges at the CNF surface may also serve as atomic surface irregularities to facilitate the formation of nanocolumnar structures. The sputtered atoms strike the substrate from the surface normal, making the incoming deposit flux at a glancing angle relative to the VACNF surface, which significantly augmented the atomic shadowing effect. Interestingly, the nanocolumns did not present at the very top of the CNF tip which directly faced the sputtered atom flux. It is noteworthy that previous studies found that Si coating on vertically aligned CNTs by chemical vapor deposition (CVD) formed very different structures, i.e. non-continuous solid clusters anchored on the CNTs similar to a pearl chain structure.[45] A similar nanocolumnar microstructure was observed by another group in the Si shells sputter-coated on PECVD-grown VACNFs.[120] This microstructure seems to be a result from the combination of sputtering and the unique sidewall structure of VACNFs.

While the nanocolumnar structure with a large void space is undesired for some applications, it provides a unique means to integrate macro- (Cu foils), micro- (VACNF length), and nano- (VACNF diameter and nanocolumns) structures for the most efficient Li^+ diffusion in LIB processes. In fact, the Li^+ diffusion length across the solid Si is reduced to less than 10 nm with this hierarchical structure, whose significance was not emphasized in previous literature.[120] Raman spectra of the Si-coated VACNFs (Figure 3.10) before half-cell lithiation tests confirmed the nanocrystalline structure in the Si shell, as indicated by the sharp peak at 480 cm^{-1} shift from 520 cm^{-1} peak in Si(100) wafer.[115, 116, 121] After charge-discharge cycles, the nanocrystalline Si is completely converted into amorphous Si.

4.3.2 High Current Rate Testing of Si-coated VACNF Electrode

Figure 4.3 shows the insertion/extraction capacity and associated columbic efficiency of the Si-coated VACNFs over 500 charge-discharge cycles. To evaluate the high-rate properties, the testing procedure consisted of five power testing (PT) series at varied C-rates while the electrode was progressively stressed with prolonged 1C charge-discharge cycles. The expanded details of the first 250 cycles are shown in Figure 4.3b, and the capacity in relation to the combined mass of Si and VACNFs in Figure 4.3c. Each PT series consisted of measurements at over five different current rates varying between C/8 to 8C, with up to five cycles at each specific rate. A few cyclic voltammograms (CVs) were taken at 0.1 to 1.0 mV s^{-1} scan rates after completing PT3 at Cycle $^{\#}$256.

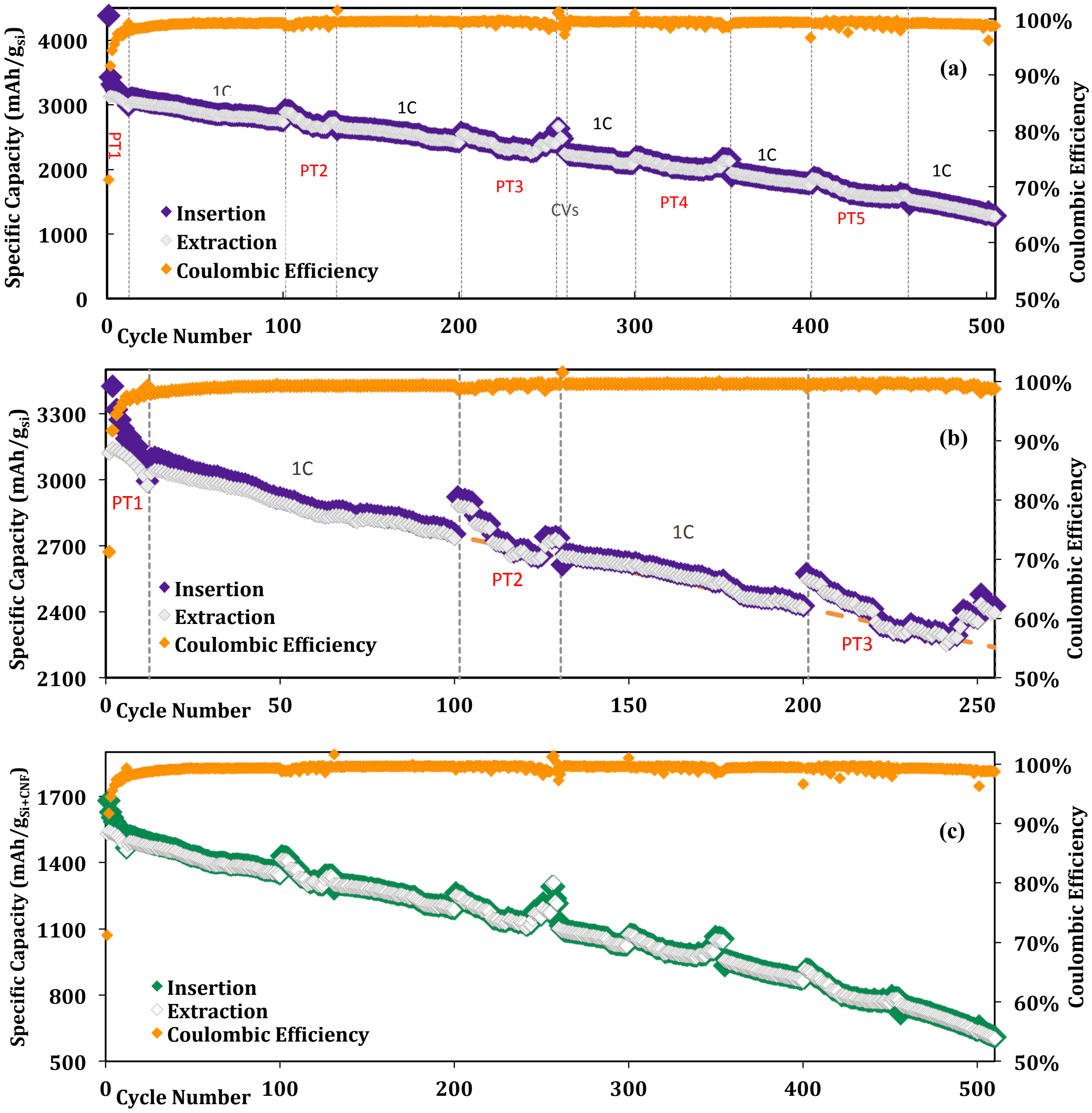

Figure 4.3 – Cycling evaluation of Si-coated VACNF electrode during long cycles. (a) Insertion and extraction capacities and Coulombic efficiency over 500 charge-discharge cycles. (b) The first 250 cycles showing the capacity normalized to only Si mass. (c) The full 500+ cycle profile with the capacity normalized to the total mass of Si and VACNFs. The Si-coated VACNF electrode was first conditioned with two cycles each at C/8, C/4, C/2, 1C, 2C, and 5C rates and subsequently tested at 1C rate for the next 88 cycles. This was repeated from cycle 101 to cycle 200. Starting at cycle 201, the electrode was cycled for five cycles each at C/4, C/3, C/2, 1C, 1.33C, 1.5C, 2C, 3C, 4C, 5C and 6C rates and subsequently tested at 1C rate for 45 cycles. Current rates applied to the cell were recalculated and adjusted after every 100 cycles to correct the capacity fading.

A high insertion capacity of ~4,500 mAh $(g_{Si})^{-1}$ (normalized to the Si mass) was observed in the first cycle at C/8 rate (due to Solid Electrolyte Interphase (SEI) formation, side reactions with residual oxygen, and transformations of crystalline Si to amorphous Si)[116] and then the electrode became fairly stable with an extraction capacity of ~3,140 mAh $(g_{Si})^{-1}$ in the second cycle at the same C-rate. The current rate was then incrementally increased to 5C at the 12th cycle, showing an extraction capacity still as high as 2,973 mAh $(g_{Si})^{-1}$ and a Coulombic efficiency of ~99%. Overall, the Si-coated VACNF electrode showed remarkable stability. Even after stressing at 5C to 8C during the five power tests, the 1C capacity only slowly dropped from 3,078 mAh $(g_{Si})^{-1}$ (cycle $^{\#}$8) to 1,266 mAh $(g_{Si})^{-1}$ (cycle $^{\#}$505), with average columbic efficiency as high as 99.8%. In Chapter 3, we found that the capacity of Li intercalation into the VACNFs is negligible in comparison to the capacity of Li alloying with the Si coating when cycled between 1.5 V and 0.05 V potential window.[116] In the sample of 500 nm Si deposited on 3 μm long VACNFs, the mass ratio is Si:C = ~1:1. Figure 4.3c shows the specific capacity normalized to the combined mass of Si and VACNFs. It is worth to note that the specific capacity at high current rates (4C and 8C) is still the highest reported for an electrode of this Si-sputtered design; to our knowledge. Even the end capacity is 3.4 times of the maximum by graphite anodes.

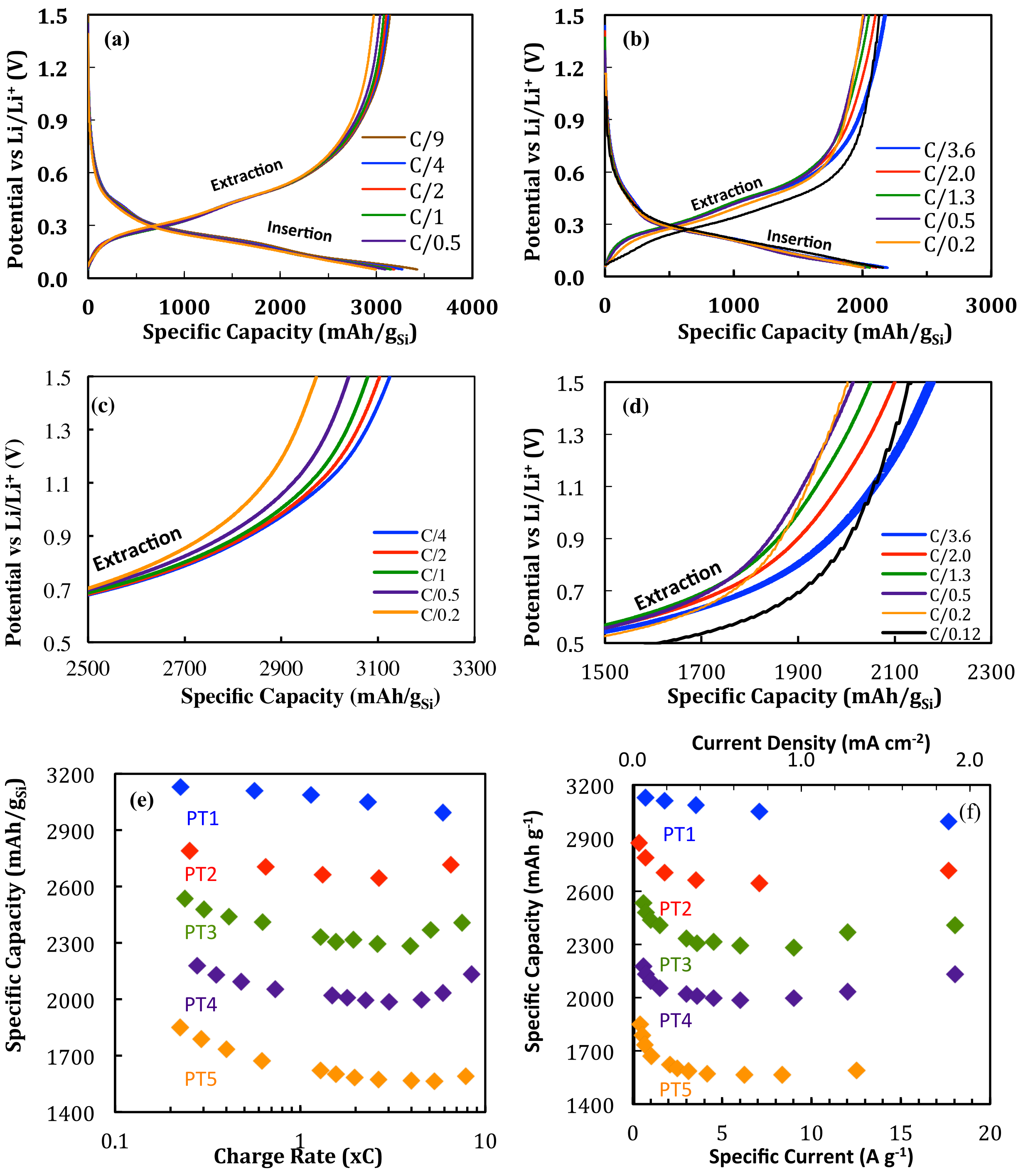

Figure 4.4 – Galvanostatic charge-discharge profiles of Si-coated VACNFs at selected C-rates during (a) the 1st PT series (cycles 1-16) and (b) the 4th PT series (after 300 cycles). (c) and (d) are the zoomed in observation of the extraction tails of the voltage profiles for (a) and (b). All profiles were taken from the second cycle in set of five at each rate. Specific extraction capacities versus (e) C-rate and (f) specific current density (A/g) on lower axis during PT1 (cycles 1-16) (◆), PT2 (cycles 101-125) (◆), PT3 (cycles 201-255) (◆), PT4 (cycles 301-355) (◆) and PT5 (cycles 401-455) (◆) are summarized. The anomalous capacity increase at high C-rates (~3C to 8C) is highlighted in the dashed box.

The power testing results are summarized in Figure 4.4. The first series of 12 cycles consisted of 2 cycles each at C/8, C/4, C/2, C/1, 2C and 5C where the initial current density for C-rates was calculated from the average capacity of 3,535 mAh $(g_{Si})^{-1}$ from our previous studies.[116] As the C-rate was increased, it did show a gradual decrease in capacity, but the total loss was only 5.3% from C/4 to 5C, rarely seen in Si LIB anodes.[32] The small difference is shown in the galvanostatic profiles in Figure 4.4a. The end portions of the extraction profiles are enlarged in Figure 4.4c-d for better view of the small change of extraction capacity from 3,140 mAh $(g_{Si})^{-1}$ at C/4 rate to 2,973 mAh $(g_{Si})^{-1}$ at 5C rate. The profiles show plateaus at 0.4–0.05 V for insertion and 0.2–0.6 V for extraction, consistent with the characteristics of other nanostructured Si anodes.[32]

To our surprise, the C-rate capability was significantly improved after prolonged cycling at 1C rate. As shown in Figure 4.4e, after 100 full 1C cycles following PT1, the electrode was still able to provide an extraction capacity of 2,885 mAh $(g_{Si})^{-1}$ at C/4 rate in the first cycle of PT2, or 91.8% of that in the 3rd cycle at the same C-rate. More importantly, it slightly increased from 2,644 mAh $(g_{Si})^{-1}$ at ~2.67C to 2,717 mAh $(g_{Si})^{-1}$ at ~6.5C in this power test (PT2). To validate this, the 3rd power test (PT3) was performed after another 100 cycles at 1 C (i.e. at Cycle #200), but using 5 cycles at each C-rates to ensure the reliability. A similar trend as in PT2 was observed: the capacity decreased first and then increased (by ~2.8%) while the power rate was increased from C/10 to 8C. A minimum was found around 3C. The C-rate dependence is more evident in extraction profiles than insertion (Figures 4.4b and 4.4d). After 200 cycles, the extraction capacity still remained ~2,548 mAh $(g_{Si})^{-1}$ at C/4 rate or 81.1% of the initial extraction capacity. The specific capacity versus the current density normalized to both of the surface area and Si mass (Figure 4.4f) showed the similar trends as the C-rate dependence in Figure 4.4e, excluding the possibility that the capacity increase at high C-rates was artifacts by resetting C-rate currents after each 100 cycles. The CVs after 256 cycles are similar to the literature on Si-coated NWs.[45, 122]

The 4th and 5th power tests were carried after 300 and 400 cycles, respectively, which showed similar phenomenon, where the capacity increased by 5.6% from 3C to 8C (PT4) and 6.8% from 4C to 8C (PT5), respectively. Overall, in each PT series, the capacity changes were very small (< 10%) while the C-rate was increased by greater than 60 fold. The overall capacity only slightly dropped after each additional 100 cycles. Preconditioning at low C-rates at the beginning was found critical to stabilize the electrode to achieve the high performance. Applying over 5C rate at the initial cycles tended to irreversibly damage the electrode and lower the performance.

Figure 4.4b also shows that, after long cycles, the extraction plateau was lowered by ~90 mV at 8C rate from those at other rates, indicating that it requires less energy to extract the inserted Li. This is unlikely due to Li plating since the low potential limit was set at +50 mV versus Li/Li^+ reference, higher than the usual Li plating potential**.** TEM examination after long cycles did not show any evidence of Li plating, but did show that the nanocolumnar structure of the Si shell was preserved (Figure 4.5). To our knowledge, the capacity increase at high currents has not been reported in literature. The Li storage capacity of most LIB electrodes drops significantly as the rate is increased. We attribute this to the unique VACNF-Si core-shell architecture, which consists of the nanocolumnar Si shell that remains intact after long cycling.

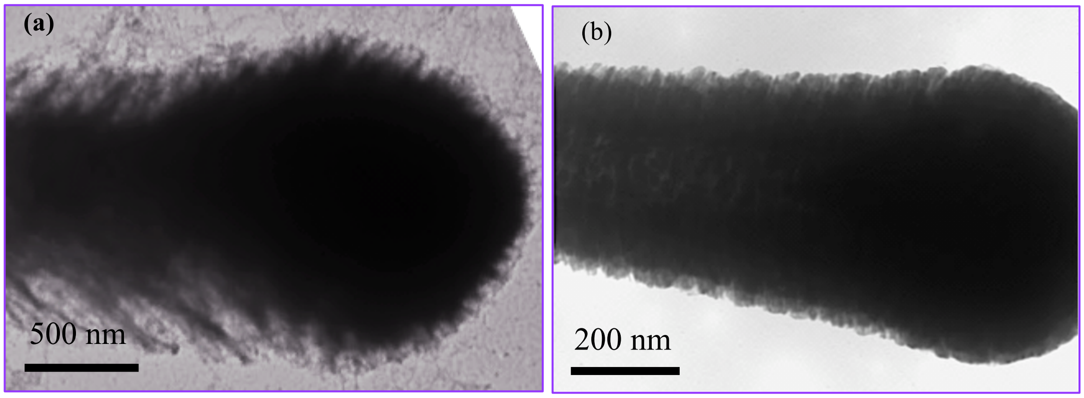

Figure 4.5 – TEM images of the Si-coated VACNF taken out from the cell in the (a) lithiated state after the 138th cycle and (b) delithiated state after 750th cycle. Carbon/Formvar coated grids were used.

The void space between the nanocolumnar Si acts as galleries for fast Li^+ diffusion in electrolyte and significantly shortened the Li^+ path length in solid Si. In addition, an expected thin SEI veil forms over the individual Si needles, providing a flexible sheath that prevents the Si nanoneedles from coalescing or breaking off during lithiation/delithiation-induced expansion/contraction. This SEI layer is enhanced by the addition of 2% vinylene carbonate (VC) to the electrolyte, for which VC is known to become reduce at 0.8 V, causing its polymerization to form a thin and reliable coating that has been shown to enhance the overall stability and cycling performance of Si electrodes.[123, 124] The TEM image (Figure 4.5a) a Si-CNF taken out from the cell in the lithiated form (at 0.05 V) after a long cycling test indeed shows that the Si nanocolumns in the shell was elongated but remained anchored on CNF core. A very thin (20-30 nm) low-density material, likely so-called SEI, can be seen filling the void space between Si nanocolumns and hold them in place. In contrast, the TEM image (Figure 4.5b) of the Si-CNF sample taken out from the cell in the delithiated form (at 1.5 V) after long cycling shows shorter nanocolumnar structure with a clean surface, very similar to that of the pristine sample before used for LIB tests (see Figure 4.5b). These results are consistent with the SEM observation of the reversible expansion/contraction in our previous study (Chapter 3).[116] To further understand the high-power capability, electrochemical impedance spectroscopy (EIS) was employed to characterize the Si/VACNFs at various states of charge (SOC) and after long cycles.

4.3.3 Electrochemical Impedance Spectroscopy of Si-coated VACNF Electrode

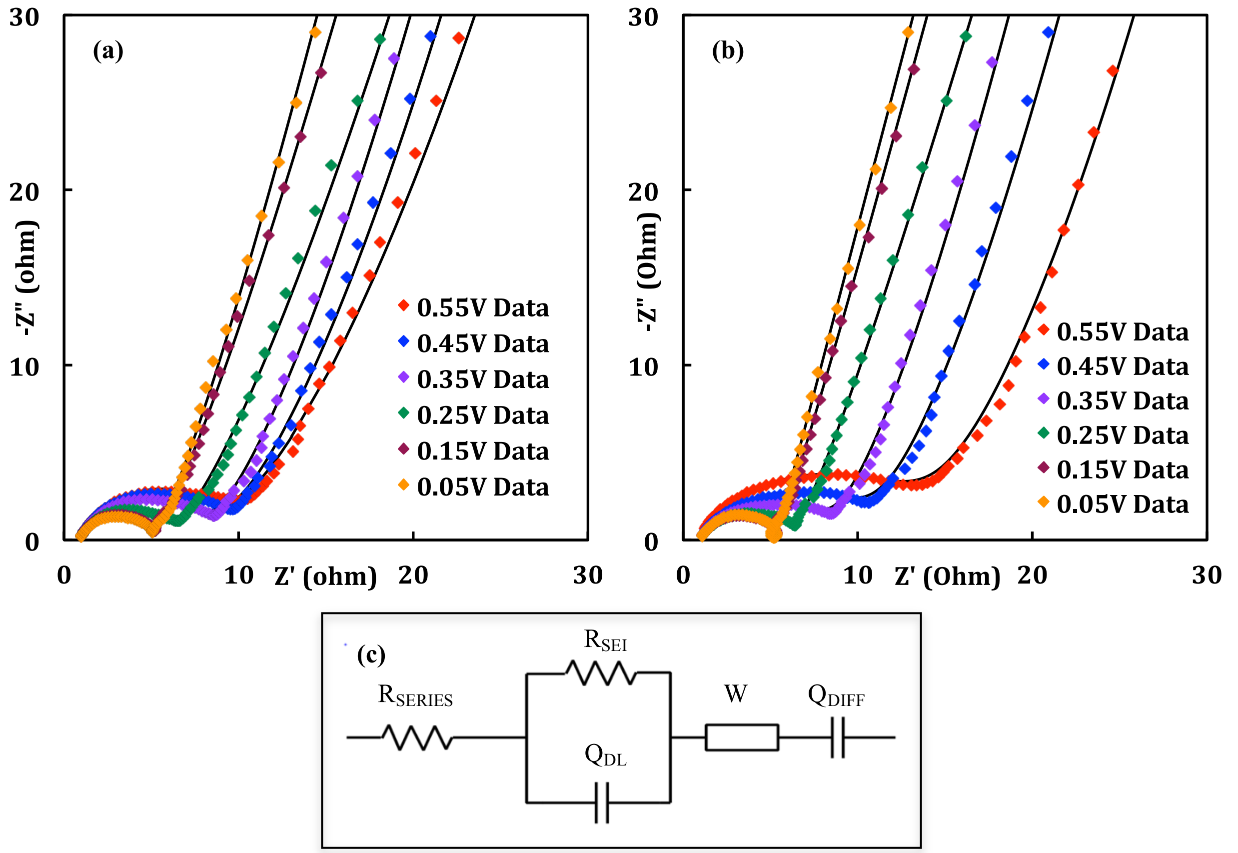

Figure 4.6 – Nyquist plots of Si-coated VACNF LIB anode after (a) 115th cycle and (b) 200th cycle at different static potential from 0.55 V to 0.05 V versus Li/Li$^+$. Solid lines are fitting curves using the equivalent circuit model shown in (c).

Figure 4.6 shows the Nyquist plots measured at potentials from 0.55 V (~30% SOC) to 0.05 V (~100% SOC) after 115 and 200 cycles at 1C. The solid lines are the fitting curves using a Voigt-type equivalent circuit (Figure 4.6c) based on the Frumkin and Melik–Gaykazyan model,[125] which has an extra serial element Q$_{DIFF}$ when compared to a study on Si NW LIB anodes.[126] high frequencies (>10 kHz), the impedance is dominated by the series resistance R$_{SERIES}$ from external circuits, Si/substrate interface, and the ionic conduction in electrolytes. In the medium frequency region (10 kHz to ~10 Hz) it is dominated by the parallel RC elements including the surface resistance R_{SEI} for Li^+ migration through the SEI film at the outer surface of the Si shell and a constant phase element (CPE) Q_{DL} accounting for the fast pseudocapacitive Li reaction with the active Si shell.[127, 128] CPE instead of a capacitor is necessary in order to fit the vertically depressed semicircle caused by the porous structure. A serial Warburg diffusion element (W) is used to account for the slow Li+ diffusion interior Si, represented by the 45° slope (from ~10 Hz to ~1.0 Hz) at end of the semicircle. A second CPE (QDIFF) is used to fit the nearly vertical line at the low frequency end (< 1.0 Hz), accounting for the very slow Li+ diffusion in thicker Si material (diffusion coefficient $D_{Li+} = \sim 3\text{x}10^{-14}$ cm^2/s in bulk solid Si vs. $5.1\text{x}10^{-12}$ cm^2/s in nano-Si [129] and $\sim 1\text{x}10^{-5}$ cm^2/s in volatile organic electrolyte).[130]

The above model fits all EIS curves very well ($\chi^2 = \sim 1\text{x}10^{-3}$). The fitting parameters are summarized in Tables 4.1-4.3. Clearly, R_{SERIES} is very small and only slightly increases with SOC. The value of W is also relatively stable and increases slightly with SOC after long cycles. Q_{DL} values are very similar in two sets of experiments. The most prominent changes are shown in R_{SEI}, which gradually decreases upon lithiation from 7.25 to 4.05 Ω after 115 cycles and from 14.09 to 4.32 Ω after 200 cycles. This trend is opposite to the observation in amorphous Si thin films [131] and single-phase Si NWs [126], in which R_{SEI} increased as SOC was increased. It is likely that, during Li insertion process as the electrode potential is lowered, the expansion of the Li-Si alloy shell in this multi-scale architecture stretches the SEI layer that has been formed at higher potential and causes it to thin, thus allowing for better Li^+ transport.[32] The admittance factor Y_O of Q_{DIFF} increases with SOC, which reflects a decrease in impedance, as Si is lithiated. This can be related to the expanded porous structure of the Si nanocolumns during alloying as well as the doping effects.

Table 4.1 - EIS Fitting Parameters of Si-Coated VACNFs after 16th cycle.

Potential (V)	R_{SERIES} (Ω)	Q_{DL}-Y_0 ($\Omega^{-1}s^{n}$)	Q_{DL}-n	R_{SEI} (Ω)	W-Y_0 ($\Omega^{-1}s^{0.5}$)	Q_{DIFF}-Y_0 ($\Omega^{-1}s^{n}$)	Q_{DIFF}-n	Chi^2
0.300	0.740	0.00031	0.912	5.58	0.0670	0.12330	1.000	1.63E-03
0.250	0.768	0.00032	0.913	5.35	0.1076	0.11910	0.949	1.50E-03
0.200	0.783	0.00043	0.895	4.00	0.3012	0.11580	0.884	1.30E-03
0.150	0.795	0.00049	0.896	3.27	0.3945	0.16030	0.936	1.77E-03
0.100	0.799	0.00057	0.884	2.87	0.7641	0.19170	0.911	1.13E-03
0.050	0.800	0.00062	0.876	2.69	0.7324	0.25790	0.940	1.07E-03

Table 4.2 - EIS Fitting Parameters of Si-Coated VACNFs after 115th cycle.

Potential (V)	R_{SERIES} (Ω)	Q_{DL}-Y_0 ($\Omega^{-1}s^{n}$)	Q_{DL}-n	R_{SEI} (Ω)	W-Y_0 ($\Omega^{-1}s^{0.5}$)	Q_{DIFF}-Y_0 ($\Omega^{-1}s^{n}$)	Q_{DIFF}-n	Chi^2
0.600	0.811	0.00078	0.705	7.25	0.0615	0.07021	0.898	1.09E-03
0.550	0.812	0.00064	0.720	8.10	0.0562	0.07274	0.965	8.57E-04
0.500	0.831	0.00058	0.730	7.96	0.0627	0.07309	0.960	9.37E-04
0.450	0.841	0.00056	0.733	7.72	0.0721	0.07577	0.952	9.32E-04
0.400	0.844	0.00057	0.733	7.38	0.0839	0.07901	0.942	9.11E-04
0.350	0.842	0.00062	0.727	6.98	0.0953	0.08531	0.933	8.43E-04
0.300	0.839	0.00070	0.717	6.39	0.1074	0.09369	0.918	7.02E-04
0.250	0.859	0.00073	0.727	5.16	0.1171	0.10860	0.903	6.29E-04
0.200	0.893	0.00055	0.779	4.39	0.1654	0.12210	0.894	8.56E-04
0.150	0.896	0.00057	0.788	3.99	0.2246	0.13750	0.882	1.02E-03
0.100	0.895	0.00061	0.787	3.82	0.3328	0.15540	0.856	1.16E-03
0.050	0.873	0.00085	0.751	4.05	0.3491	0.20000	0.886	6.90E-04

Table 4.3 - EIS Fitting Parameters of Si-Coated VACNFs after 200th cycle.

Potential (V)	R_{SERIES} (Ω)	Q_{DL}-Y_0 ($\Omega^{-1}s^{n}$)	Q_{DL}-n	R_{SEI} (Ω)	W-Y_0 ($\Omega^{-1}s^{0.5}$)	Q_{DIFF}-Y_0 ($\Omega^{-1}s^{n}$)	Q_{DIFF}-n	Chi^2
0.600	0.717	0.00118	0.626	14.09	0.0541	0.05750	0.973	8.94E-04
0.550	0.740	0.00126	0.621	12.49	0.0643	0.05871	0.957	8.46E-04
0.500	0.756	0.00140	0.614	11.03	0.0797	0.06007	0.935	8.18E-04
0.450	0.772	0.00159	0.605	9.58	0.0937	0.06431	0.929	8.34E-04
0.400	0.791	0.00170	0.604	8.32	0.1050	0.07012	0.927	8.39E-04
0.350	0.812	0.00170	0.607	7.39	0.1253	0.07486	0.916	8.22E-04
0.300	0.831	0.00157	0.617	6.77	0.2163	0.07136	0.859	8.95E-04
0.250	0.900	0.00127	0.653	5.30	0.2518	0.08029	0.854	8.86E-04
0.200	0.968	0.00091	0.715	4.37	0.2929	0.10100	0.874	7.95E-04
0.150	0.990	0.00077	0.745	4.14	0.4072	0.11870	0.872	7.61E-04
0.100	0.993	0.00073	0.755	4.16	0.9574	0.13250	0.848	6.68E-04
0.050	0.982	0.00079	0.747	4.32	1.8140	0.15970	0.853	4.25E-04

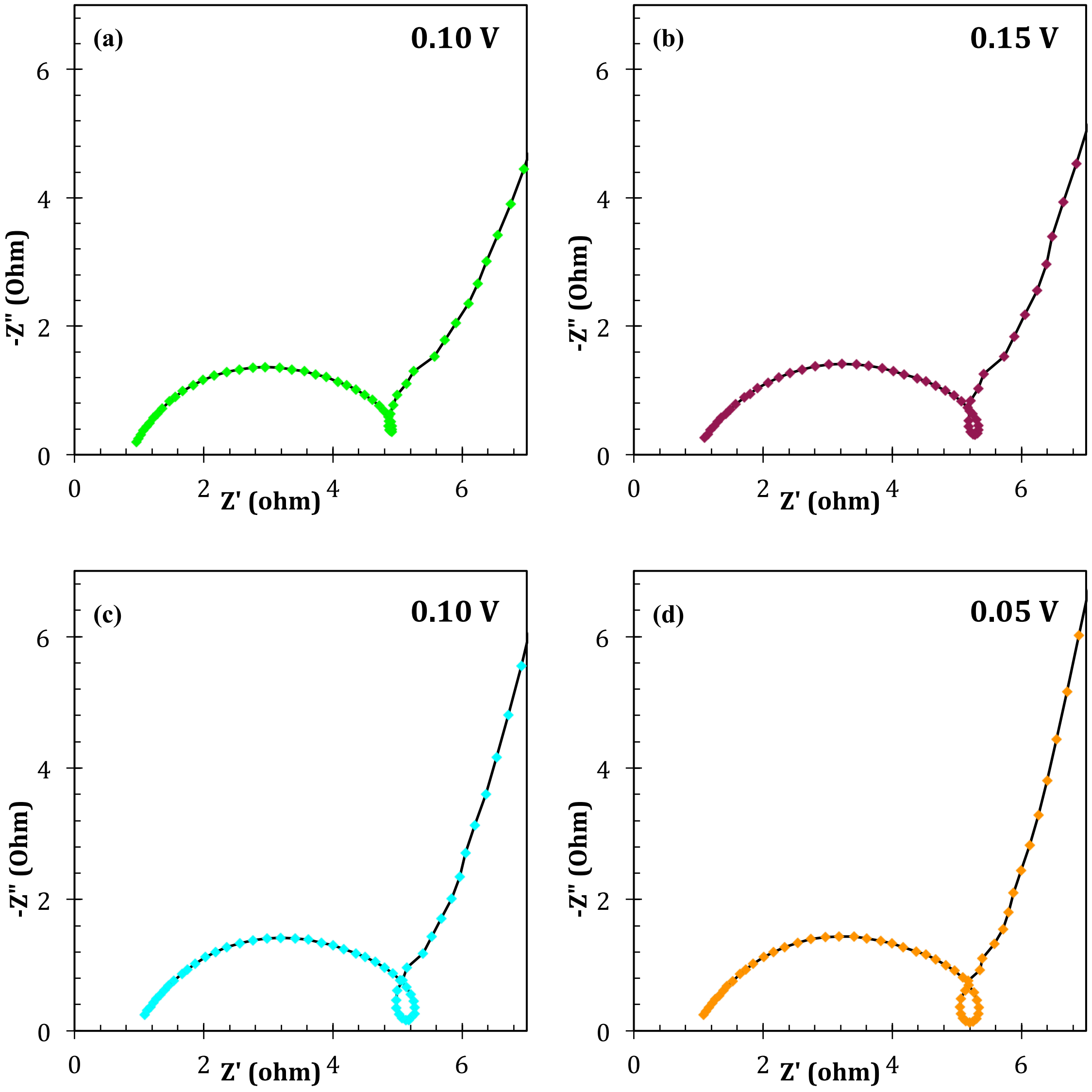

Figure 4.7 – Expanded Nyquist plots at high frequency region: (a) 115th cycle, (b), (c) and (d) 200th cycle at different low potential. Potentials are shown in the figure.

The stability of the SEI layer at Si electrode upon cycling is one of the important issues to realizing the practical electrochemical performance of Si based electrodes.[132, 133] Recently, it has been reported that formation/deposition of SEI products is a dynamic process varying with the electrode potential; in competition with the charge transfer process. Franger and co-workers,[133] studied the SEI behavior on nano-Si electrode by EIS and observed an induction loop at ~1 Hz which appears only when the potential of the electrode is below 0.35 V vs. Li/Li$^+$ (or < 0.20 V vs. Li/Li$^+$, if electrolyte contains additive like fluoroethylene carbonate). The induction phenomenon indicates that both processes, SEI formation and lithiation of the Si electrode, take place simultaneously at low potentials. They concluded that it is mostly the instability of the SEI on the surface of the Si-particles that causes the appearance of the indicative loop on the corresponding EIS spectra. On careful examination of our EIS data, presented in Figure 4.6, a similar indicative loop phenomenon below 0.2 V vs. Li is observed after 200 cycles. The high frequency expanded data of low potential EIS spectra is shown in Figure 4.7. In case of EIS data recorded after 115 cycles, an inductive loop appears only at 0.1 V vs. Li/Li$^+$ (Figure 4.7a). This indicates that SEI layer is stable during initial tens of charge-discharge cycles. As mentioned earlier, the SEI layer formed in VC containing electrolyte possess improved properties and better resists to the stress caused by large volume variations during lithiation/delithiation process [123, 124]. However, after 200 cycles, the inductive loop appears below 0.2 V vs. Li/Li$^+$, as shown in the expanded EIS spectra (Figure 4.7b-d). This inductive loop became more prominent at low potentials (0.1 and 0.05 V). This indicates that the expansion of the Si nanocolumns due to lithiation (at low potential) generates some uncovered Li_xSi surface and, hence formation/deposition of SEI components takes place. The appearance of inductive loop after 200 cycles also indicates partial electrode degradation, most likely because the lithiation (hence, expansion) process is faster compared to the SEI formation/deposition. However, the small shell thickness and strong mechanical attachment to highly conductive VACNF core makes the outer surface of Li_xSi highly active so that the SEI was reversibly oxidized in the discharge process, thus maintaining a high columbic efficiency. Even though it requires extensive further study (particularly with in situ techniques such as Raman spectroscopy and synchrotron X-ray scattering or absorption) to reveal the detailed mechanism, the consistent results from our ex-situ

TEM/SEM and EIS at discrete SOCs illustrate a possible explanation to the seemingly anomalous phenomenon of capacity increase at very high rates. Bringing this to the attention of the EES community is expected to stimulate research toward developing high-power LIB materials.

4.4 Conclusions

The hybrid electrode of pine-leave nanocolumnar structured Si-shell on VACNFs has been demonstrated as a remarkable high-power anode for lithium-ion batteries. The Si shells present the full lithium storage capacity of amorphous Si, ~3,000 to 3,500 mAh $(g_{Si})^{-1}$ at normal rates (up to ~3C). The electrode showed very little degradation in over 500 cycles even after going through five heavily stressed power tests, retaining ~1,200 mAh $(g_{Si})^{-1}$ at 1C rate at the end. In addition, increasing the C-rate from C/8 to 8C during the power tests only caused very small change (< 7%) in the capacity. More importantly, the measured capacity even slightly increased from 3C to 8C rates. Such anomalous high-rate capability is a new phenomenon that has not been reported in literature and needs further attention. Further studies on such new phenomenon are required to understand the responsible mechanism, which is imperative to developing high-power performance lithium-ion batteries.

Chapter 5 - High Rate Lithium ion Battery Electrodes based on Titanium Oxide Coated Vertically Aligned Carbon Nanofibers

5.1 Introduction

Lithium ion batteries are currently the most prolific means of portable electrical energy storage, with their lightweight design providing the highest in volumetric and gravimetric energy density available commercially. However, their rate of charging-discharging is still hindered by the performance of the electrode materials, typically the lithiated metal oxide ($LiCoO_2$, $LiFePO_4$ or blended composition). In Chapters 3 and 4, Si was shown to be viable material for anode of Li-ion battery (LIB), and whose performance was enhanced through use of the use of the VACNF array.[116, 134] A similar expectation was made for the cathode, which has been the rate-limiting electrode in most LIBs. Most cathodes are based on a transition-metal oxide complex, which demonstrate low electrical conductivities ($\sim 10^{-4}$ to $\sim 10^{-14}$ S/m), causing a large voltage gradient to produce across the electrode and the need for a significant over-potential to drive reaction.[135] This can also develop when a large current is applied or demanded from the battery, reducing the efficiency of the delivered power output. This variation potential can affect the Li concentration within the electrodes and stability through the reduction and dissolution of the transition metal or cause the collapse of the metal-oxide crystal structure, leaving the electrode damages and to have significantly less capacity.[136] The low conductivity also impedes long range Li^+ diffusion, requiring greater over potentials to charge, leaving the electrode exposed to detrimental side reactions. If left unchecked, heat generation from the high resistivity can cause the materials to degrade or decompose leading to a total failure. Most commercial electrodes are compensated by use of various additives and binders to fabricate cathodes with greater interconnectivity, helping to increase both specific capacity and rate performance.[135] To improve current density further, new structures are needed for the active materials, providing shorter Li diffusion path lengths and faster electron transport pathways to the current collector. The material must also have good ion diffusion throughout, while maintaining integrity to cycle without pulverization, severe dissolution, and disconnection.

Anatase TiO_2 is unique with a Li Redox potential of 1.8 V vs. Li/Li^+ by which the process is expressed by the equation:[52, 57]

$$TiO_2 + xLi^+ + xe^- \rightleftharpoons Li_xTiO_2 \quad (\text{with } X \leq 0.5) \tag{5.1}$$

This allows the TiO_2 to operate as an anode versus $LiCoO_2$ and produce a voltage of ~2.1V, or operate as a cathode versus Carbon and produce a voltage of ~1.6 V. This selectable voltage concept will be demonstrated more in Chapter 6, however, the voltage profile of a battery is very much dependent on the voltage profiles of the individual electrodes operating with respect to one another. For this chapter, we utilized a reactive sputtering technique, depositing nanocrystalline TiO_2 onto the VACNF arrays, forming a concentric coating along the fiber's length. The TiO_2-coated VACNF arrays were characterized versus Li foil to fully understand their performance and pseudocapacitive contributions at various high-rates.

5.2 Experimental Details

5.2.1 VACNF Growth and Titanium Oxide Deposition

Following the generalized procedure in Chapter 2, VACNF arrays were grown on Cu foils for 30 minutes to a reach length of ~5.0 μm long and reactively sputtered to deposit TiO_2 to a nominal thickness of 0.5 μm. Experimental conditions are as noted in Chapter 2.

5.2.2 Electrochemical Cell Assembly and Charge-Discharge Tests

A reusable electrochemical cell (El-Cell, Hamburg Germany) with three-electrode design (Figure 3.2) was used for the half-cell tests. The Cu disks covered with TiO_2-coated VACNFs were used as the working electrode against an 18-mm dia. lithium disk (1.5 mm in thickness) as the counter electrode. A lithium wire was used as the reference electrode. A fiberglass spacer (0.65 mm in thickness) and a Kel-F ring (18 mm outer dia., 3.0 mm thick) was placed between the working and counter electrodes with 1.0 M lithium hexafluorophosphate ($LiPF_6$) in a mixture of 1:1:1 volume ratio of ethylene carbonate (EC), ethyl methyl carbonate (EMC) and dimethyl carbonate (DMC) plus 2% vinylene carbonate (Novelty, Ohio) as electrolyte. Galvanostatic charge-discharge cycles were performed using an MTI 8 channel battery analyzer (MTI Corporation, Richmond, CA). Cyclic voltammetry (CV) was performed using a CHI760D potentiostat controlled by CHI Electrochemical Software (CH Instruments, Austin, TX). The potential window for the TiO_2-coated VACNF electrodes was set from 2.5 to 1.0 V vs. (Li/Li^+) to minimize oxidation of copper and limit SEI formation. AC impedance spectroscopy was performed using a CHI 760D potentiostat controlled by CHI Electrochemical Software (CH Instruments, Austin, TX) with a 10 mV_{pp} AC potential over a frequency range from 100 kHz to 0.01 Hz.

5.2.3 Microscopy and Spectroscopy Characterization

Both the as-prepared electrodes and those disassembled from the cells after Li-ion half-cell tests were stored and transferred in air before inspection with SEM (FEI Nano430). Some Si-coated VACNFs were scraped off from the Cu substrate onto carbon film coated Cu grids for transmission electron microscopy (TEM) (FEI Tecnai F20 XT) measurements.

5.3 Results and Discussion

5.3.1 Detailed Characterization of TiO_2-coated VACNF Electrode

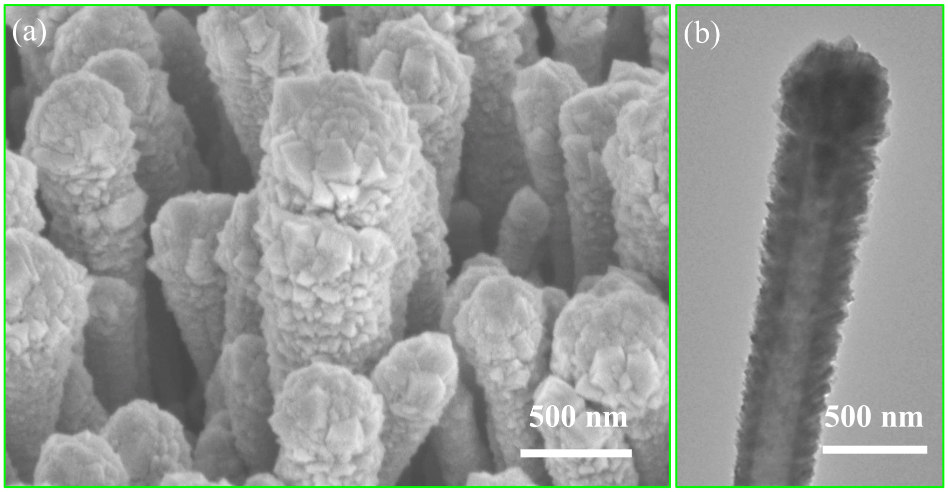

Figure 5.1 – (a) SEM and (b) TEM images of TiO_2-coated VACNF NW after reactive sputtering and before cycling. Both scale bars are 500 nm

On the surface, the individual CNFs after reactive sputtering of TiO_2 to a nominal thickness of 500 nm showed a similar cotton swab appearance that appears with the Si electrode (Figure 4.1). There is the large mass of TiO_2 material at the top of the fibers that has bulky crystals of several tens to hundreds of nanometers in diameter randomly arranged on the CNF. The inherent crystallite feature extends down the shaft of the CNFs, coating the fiber quite concentrically (Figure 5.1). More fascinating, Figure 5.1b shows the polycrystalline shell comprised of many smaller (5-20 nm) crystals that wrap around the fibers surface, mirroring the stacked conical structure. Some of the crystals jut out from the shell, producing a surface that is very rough in texture and shows large grain boundaries permeating deep to the core, allowing for easier access by the electrolyte. As with the Si-coated CNFs, the TiO_2 shell tapers gradually down the length of the CNF, thinning to less than 20 nm in shell thickness. Variation in shell thickness and conformity are due to fluctuations during deposition, which include shadow effects, temperature, and rate of deposition (as described in section 4.3.1).

5.3.2 High Current Rate Testing of TiO_2-coated VACNF Electrode

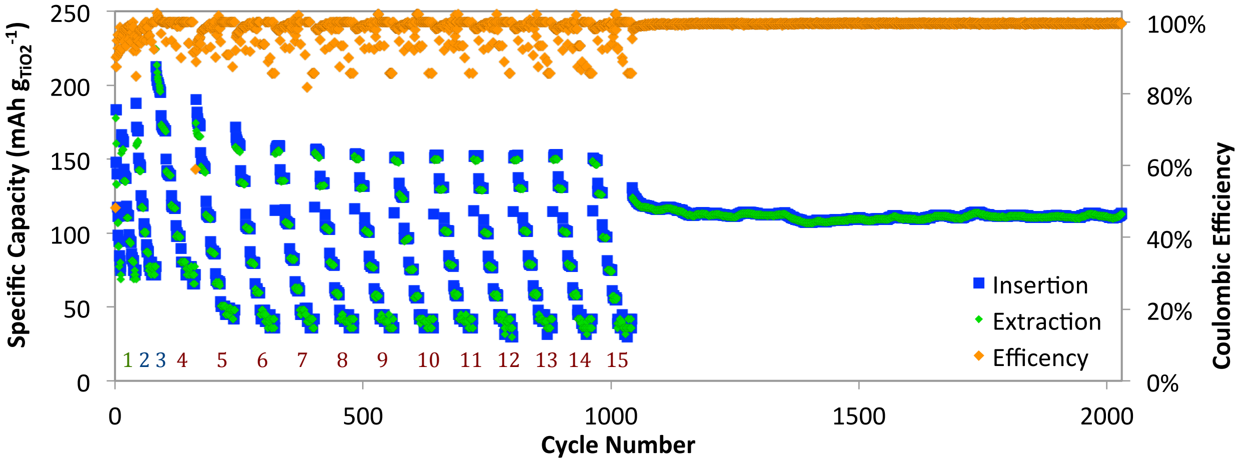

Figure 5.2 – Cycling performance of TiO_2-coated VACNF electrode showing insertion and extraction capacities with respect to the mass of TiO_2 (left vertical axis), and Coulombic efficiency (right vertical axis).

With an understanding that TiO_2-based electrodes show high-rate performance, the TiO_2-coated VACNF electrode was started at a 1C rate and cycled at progressively larger currents. This was referred to as the power test (PTs, labeled sequentially under each grouping in Figure 5.2). Initially, the TiO_2 electrode was cycled for two cycles each at 90, 180, 450, 900, 1800, and 4500 μA, which corresponds to 1C , 3C, 10C, 23C, 55C, and 150C, respectively. A high insertion capacity of 368 mAh $(g_{TiO2})^{-1}$ was observed in the first cycle and achieved only 178 mAh $(g_{TiO2})^{-1}$ on the extraction cycle; resulting in a first cycle loss of 51%. This loss was primarily due to reactions of the Li with residual oxygen on the TiO_2 surface left from the sputtering process. The second and third cycle saw insertion capacities of 183 and 147 mAh $(g_{TiO2})^{-1}$, while achieving 178 and 160 mAh $(g_{TiO2})^{-1}$ upon extraction. Over the first 3 cycles, the electrode resulted in net loss of 228 mAh $(g_{TiO2})^{-1}$, equivalent to 130% the theoretical capacity of TiO_2. It has been reported that a "break-in" period of three to five cycles is needed to fill irreversible insertion titanate sites and to oxidize and consume any trace water.[137] This point will be crucial later in Chapter 6. After this period, Coulombic efficiency appeared to level off quickly with each change in current rate. The second and third PTs were cycled for five cycles each at same current steps (90, 180, 450, 900, 1800, and 4500 μA), with capacity values remaining stable over the entire step and increasing slightly from PT2 to PT3 for identical currents. This was indicative of the TiO_2 becoming fully activated and with reaction sites becoming more stable.

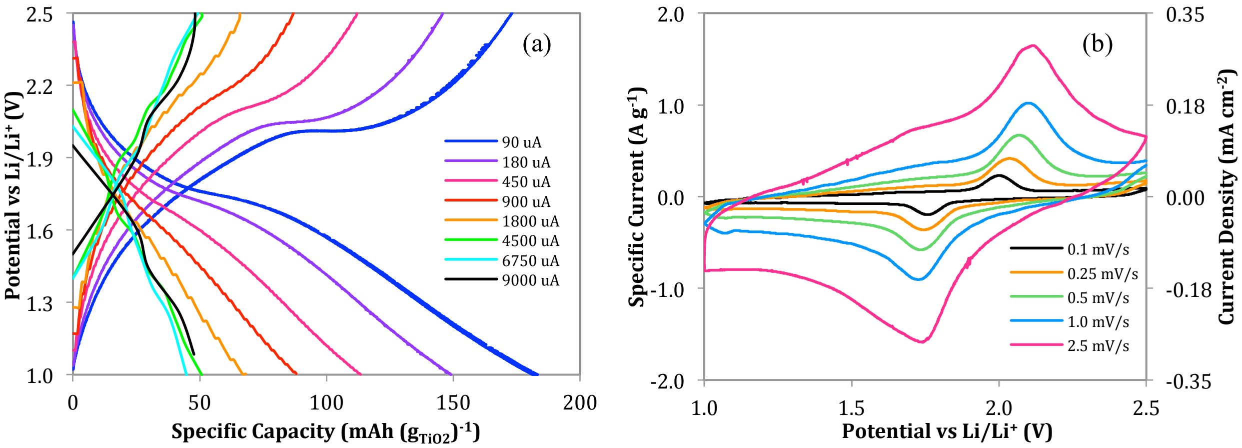

Figure 5.3 – Electrochemical characterization of Li insertion and extraction of TiO_2-coated VACNFs at the nominal thickness of 0.50 μm. (a) Galvanostatic charge-discharge profiles at selected current rates, and (b) cyclic voltammograms operating between 2.5 V and 1.0 V versus Li/Li^+ showing scan rates from 0.1 mV s^{-1} to 2.5 mV s^{-1}.

For PT4 –PT15, two additional currents were added to each series, 6750 and 9000 μA, while also increasing the cycles per step to ten. The half-cell cycling was restarted with PT4 showing exceptionally high capacity of 224 mAh $(g_{TiO2})^{-1}$ for 90μA, that leveled out gradually to 196 mAh $(g_{TiO2})^{-1}$. At 900 μA, the TiO_2-coating achieved a capacity of 117 mAh $(g_{TiO2})^{-1}$, and at 9.0 mA (300C), showed an outstanding 77 mAh $(g_{TiO2})^{-1}$. Figure 5.3a shows the voltage profiles of all the currents during PT4. The 90 μA profile shows TiO_2 dual storage processes of Li^+ insertion[138] and Li^+ redox pseudocapacitance[56]. Since the TiO_2 shell is polycrystalline in nature, it consists of a large number of particles that have an even greater surface area and reactivity. Dunn et al. has reported that larger particles contribute to a greater faradaic response[57] since the crystalline phase requires a Li^+ diffusion process to achieve full saturation. This only occurs at the intrinsic redox potential (1.55 V), thus the development of a large sloping curve combined with the phase changing insertion/extraction plateaus is shown in the voltage profile.

Increasing the current to 900 μA shows a most significant decrease in Li^+ insertion processes, while maintaining a good portion of the energy in the form of surface pseudocapacitance. Increasing to 9.0 mA, the profile becomes near linear, suggestive of capacitor like operation only, with relatively lower capacities at high rates. By PT6, cycling had fully stabilized for all currents, demonstrating capacities of ~156 mAh $(g_{TiO2})^{-1}$ for 90μA, ~79 mAh $(g_{TiO2})^{-1}$ for 900μA, and ~42 mAh $(g_{TiO2})^{-1}$ for 9.0 mA, with less than a 5% decrease in discharge capacity after 1900 cycles (PT15). Coulombic efficiency also achieved near 100% throughout the power tests except for first cycles after each current rate change. As the voltage profiles suggest in Figure 5.3a, the shift in contribution of the dual Li^+ processes to decrease in lithium insertion/extraction capacity and become significantly surface pseudocapacitance. For long cycling performance, a symmetric 300 μA (6C) current rate was applied for 2000 cycle (Figure 5.2) showing a capacity of 122 mAh $(g_{TiO2})^{-1}$ at its start and 113 mAh $(g_{TiO2})^{-1}$ upon completion, while maintaining greater than 99% Coulombic efficacy. This performance is credited to the TiO_2 layered structure that shows near zero-percent volume expansion upon lithiation, remaining stable over many thousands of cycles, and having a significant large surface area available for fast, pseudocapacitive reactions.

Cyclic voltammetry was performed on the TiO_2-coated VACNF electrode from 2.5 V to 1.0 V at scans rates varying from 0.1 mV s^{-1} to 2.5 mV s^{-1}. Figure 5.3b shows the I-V curves, all of which show charging current contributions between the voltage limits, represented by the rectangular box shape of the curve. The faradic peaks appear well separated, with Li^+ insertion occurring at 1.77 V and extraction occurring at 1.99 V for 0.1 mV s^{-1} scan rate. Increasing the rate to 1.0 mV s^{-1} shows a larger separation in the peaks with 1.73 V and 2.09 V, respectively. Dunn et al. noted that Li^+ insertion/extraction into nano-sized TiO_2 materials was still sluggish for they are very and very dependent diffusion rate of Li^+ (Degussa P25 (30 nm): 1.1 $x10^{-15}$ cm^2 s^{-1}), giving rise to slightly the larger peak separations at increased scan rate.[57]

5.3.3 Electrochemical Impendence Spectroscopy of TiO_2-coated VACNF Electrode

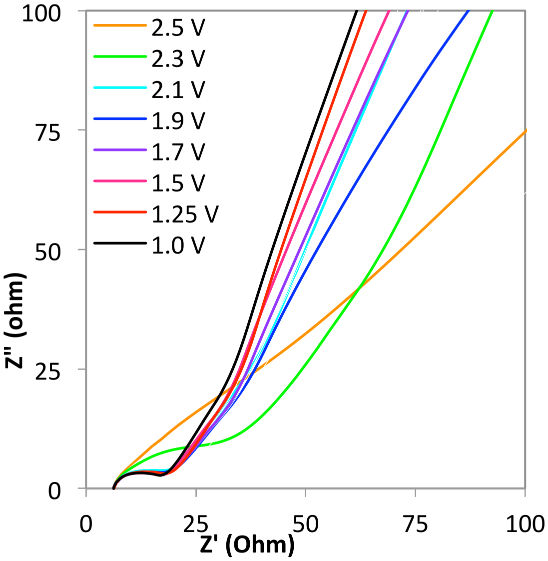

Figure 5.4 – Nyquist plot of TiO_2-coated VACNFs after 1000 cycles and at different static voltages from 1.0 V to 2.5 V.

Figure 5.4 shows the Nyquist plots measured after 1000 cycles at potentials from 2.5 V to 1.0 V. The electrochemical impedance is minimal at 6.2 Ω, which represents the series resistance of the external circuit, TiO_2/CNF/substrate interfaces, and the ionic conduction in electrolytes. In the medium frequency region (10 kHz to ~10 Hz) it is dominated by the parallel RC element (semicircle feature) that includes charge transfer resistance and impedance of Li^+ diffusion. A large Warburg diffusion element is present (represented by the 45° slope) for Voltages below 2.0V, which accounts for the slow Li+ diffusion toward the interior of the TiO_2, while a straight capacitive tail at the low frequency represents the capacitance at the surface of the electrode. The deviation of higher voltage plots is expected as no further charge transfer can be achieved, and is pure capacitance that is stored by surface reactions.

5.4 Conclusion

Here, we have demonstrated that TiO_2 can be effectively coated onto the VACNF structure utilizing reactive sputtering to form a concentric coating that is not only robust, but can provide high rate charge-discharge over many hundreds of cycles. The VACNF arrays demonstrated to be a good platform for the deposition of TiO_2 onto the surface, providing an effective electrical interface with the entire TiO_2 shell allowed the material to become fully lithiated with a maximum capacity of 224 mAh $(g_{TiO2})^{-1}$ at a 1C rate. Capacity retention remained high at larger current rates, demonstrating that the TiO_2 was capable of fast surface reaction fast electron transfer. This work continues to show that assembling hybrid structures using the VACNF array as a template is a viable approach for energy storage technologies.

Chapter 6 - A Novel High-Power Battery-Pseudocapacitor Hybrid Based on Fast Lithium Reactions in Titanium Dioxide Cathode and Silicon Anode Coated on Vertically Aligned Carbon Nanofibers

Submitted for publication. S. A. Klankowski, G. P. Pandey, G. A. Malek, J. Wu, R. A. Rojeski, J. Li, (2015).

6.1 Introduction

Electrochemical energy storage (EES) systems have been widely used for powering today's portable electronics and may play a bigger role in supporting future electric vehicles and energy technologies utilizing intermittent renewable sources.[56, 139] An ideal EES system would provide as high as possible energy capacity while delivering the maximum power. These two technical merits are each represented by the characteristics of today's two most successful EES systems, i.e. Lithium ion batteries (LIBs)[140] and electrochemical supercapacitors.[13] But, due to the distinct mechanisms, they are not capable of being integrated into one system without significantly compromising one or the other. LIBs are known to have very high specific energy due to the large amount of Li involved in intercalation or alloying reactions in the whole bulk electrode materials, but their deliverable power is rather low, limited by the slow reaction rate due to the slow Li^+ diffusion in solid materials.[140] In contrast, electrochemical supercapacitors, particularly pseudocapacitors, can charge-discharge at much higher rates based on fast electrochemical reactions occurring at the electrode surface or in a thin layer near the surface. Since only a small portion of the electrode material is involved in the reactions, the specific energy is much lower.[13, 56] The recent development in LIBs has focused on innovative nanostructured electrode materials in which the Li^+ diffusion length in solids can be reduced to tens of nanometers, thus leading to largely improved power rates.[141, 142] In such systems, the pseudocapacitive contribution from fast surface reactions becomes significant, leading to properties similar to a battery-supercapacitor hybrid.[141, 142] However, the obtainable Li storage capacity and the specific energy were found to significantly decrease as the nanoparticle size was reduced.[141, 143] Here we demonstrate that it is possible to develop a hybrid system to retain nearly the full capacity of the active electrode materials by utilizing the our nanostructured coaxial shells on vertically aligned carbon nanofiber (VACNF) electrodes to create a battery-supercapacitor hybrid comprised of a Si-based anode and a TiO_2-based cathode. The hybrid features of such electrodes have been systematically characterized in half-cells as well as in a full cell combining these two electrodes. We have found that the full-cell properties can be tuned toward a battery or pseudocapacitor by changing the capacity ratio between the two electrodes and charge-discharge rates. The high-power capability of the TiO_2-VACNF electrode is fully utilized as the cathode to match the Si-VACNF anode in a novel full cell with unique battery-pseudocapacitor hybrid features.

6.2 Experimental Details

6.2.1 Fabrication of Silicon and Titanium Oxide Electrodes

Following the generalized procedure in Chapter 2, VACNF arrays were grown on Cu foils for 30 minutes to a reach length of ~5.0 μm long. High-vacuum magnetron sputtering was employed to deposit pure Si or reacted anatase TiO_2 onto the VACNF arrays to form the concentric coatings to form the shell-core nanowires. All electrodes were stored under argon until use.

6.2.2 Electrochemical Cell Assembly

A reusable electrochemical cell (El-Cell, Hamburg, Germany) with three-electrode design was used for the half-cell tests. The Si or TiO_2 coated VACNFs were used as the working electrode (18-mm diameter) against a lithium disk as the counter electrode. A plug of lithium was used as the reference electrode. A polyethylene spacer (0.65 mm in thickness) was placed between the working and counter electrodes. A specially designed Kel-F ring was used to separate the working electrode from the polyethylene fiberglass separator so that the vertical nanowires were not compressed, which reduced the active electrode surface area to 17.5 mm in diameter. The cell was assembled in an argon-filled glove-box (MBraun LabStar50). The electrolyte consisted of 1.0 M lithium hexafluorophosphate ($LiPF_6$) in a mixture of 1:1:1 volume ratio of ethylene carbonate (EC), ethyl methyl carbonate (EMC) and dimethyl carbonate (DMC) with 2% vinylene carbonate additive (Novolyte, Ohio). Before testing, the electrolyte was injected by a syringe in between the electrodes.

The full cell consists of a lithiated Si-VACNF anode and a pristine TiO_2-VACNF cathode. Before assembly, the pristine Si-VACNF electrode was first conditioned by 4 cycles each at 90 μA and 180 μA between 1.50 V and 0.05 V versus a lithium counter electrode in an El-Cell. The cell was stopped at 0.05 V in an additional lithiation step at 90 μA and held constant for 300 seconds at 0.049 V before being disassembled and then reassembled with a 16-mm diameter TiO_2-VACNF cathode into a 3032 coin cell. A separator soaked with the electrolyte was placed between the two electrodes to provide the desired amount of electrolyte that can fill the whole coin cell after compressing. The as-assembled cell was in the charged state with an OCV of ~1.7 V.

6.2.3 Electrochemical Charge-Discharge Tests

Galvanostatic charge-discharge cycling was performed using an 8 channels battery analyzer BST8-MA (MTI Corporation, Richmond, CA). Selected currents were used on both half-cells and full-cells, ranging from 45 μA to 4.5 mA. For half-cells, the mass-specific capacity was calculated by dividing the mass of the active materials on the electrodes estimated from the measured nominal thickness (Si: 456 nm; TiO_2: 500 nm), known density (Si: 2.33 g cm^{-3}; TiO_2: 3.50 g cm^{-3}), and the geometric electrode area. For full cells, the combined mass of Si and TiO_2 on both electrodes was used in some calculations to assess the overall energy storage properties. AC impedance spectroscopy was performed using a CHI 760D potentiostat controlled by CHI Electrochemical Software (CH Instruments, *Austin, TX*) with a 5 mV_{pp} AC potential over a frequency range from 100 kHz to 0.01 Hz.

6.2.4 Microscopy and Spectroscopy Characterizations

The morphology of the coated VACNF arrays were characterized with a SEM (FEI Nano430) at 5 kV accelerating voltage and a TEM (FEI Tecnai F20 XT) at 200 kV accelerating voltage. The crystal structure of the coatings was examined with a Raman microscope (Model DXR, Thermo Scientific, Wisconsin, USA) with a 10X 0.25NA objective and a 532 nm laser at 5 mW power.

6.3 Results and Discussion

6.3.1 Full Cell Design and Structure of Electrode Materials.

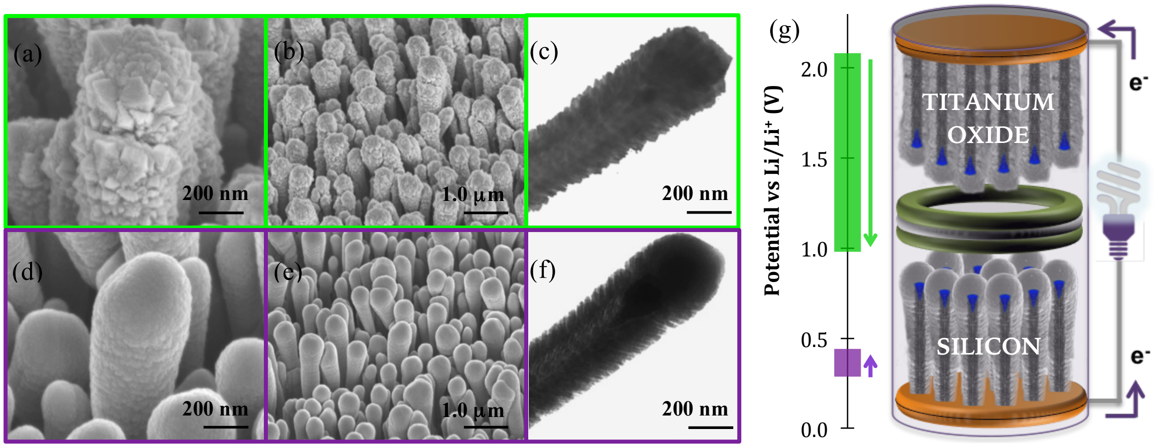

Figure 6.1 – SEM and TEM images of the as-prepared electrode materials (a-c) for TiO_2-coated VACNFs and (d-f) for Si-coated VACNFs. (g) Illustration of the full cell consisting of a prelithiated Si-coated VACNFs as anode and a TiO_2-coated VACNFs as cathode, both on cupper foil. The expected operating potentials of each electrode during cycling are shown to the left, with arrows pointing the direction of potential change during discharge.

The main focus of this study is on exploring the properties of a full cell built on the vertical core-shell architectures, with the cell design illustrated in Figure 6.1g. About 500 nm nominal thickness of Si and TiO_2 were sputter-coated on VACNFs grown on Cu foils as the anode and cathode, respectively. The use of similar nominal thickness was to ensure the formation of similar core-shell structures, but it can be increased or decreased within a factor 3 to tune the Li storage capacity without altering the electrode properties.[144] The mass of TiO_2 is about 1.5 fold of Si on the same substrate area due to its higher density. However, since the theoretical specific capacity of Li storage in Si is more than 20 times of that in TiO_2, the full-cell capacity is expected to be limited by the TiO_2 cathode. The unbalanced cell design with higher capacity at the Si anode is expected to significantly narrow down the potential change at the anode (from the normal operating range between 0.05 to 1.5 V) while the full potential range of the TiO_2 cathode (~1 to 2.2 V) is utilized. In principles, the high-power capability of nanostructured TiO_2 electrodes would be fully utilized in the full cells.[57, 145]

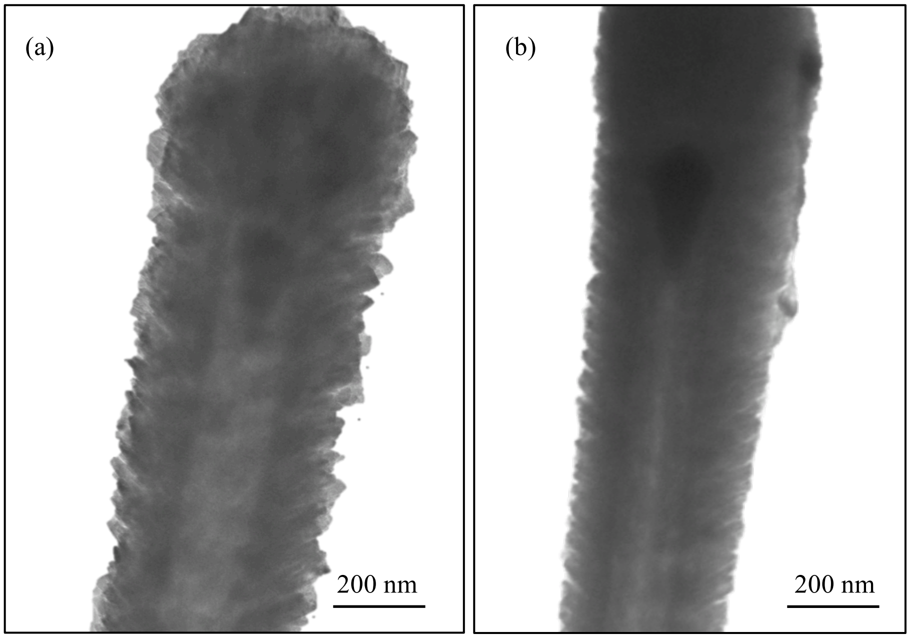

Figure 6.2 – TEM of (a) TiO_2-coated CNF and (b) Si-coated CNF.

Figures 6.1a-6c and 6.1d-6f show the structure of the TiO_2 and Si coatings on the VACNFs by SEM and TEM. Further enlarged high-resolution TEM images are shown in Figure 6.2. SEM images indicate that both materials form coaxial shells with larger radial thickness at the VACNF tips and gradually thinned moving down to the base. The largest average outer diameter is ~450 nm, appearing near the tips of the VACNFs which have a uniform diameter of ~145 nm along the ~5 μm length.[144] All core-shell fibers are vertically aligned and free-stand on the Cu foil, with open spaces between each other to allow electrolyte access and to accommodate the large volume expansion during lithiation. The TEM images in Figures 6.1f and 6.2b revealed the same feature as our previous studies (Chapter 3 and 4).[134, 144] Most importantly, the Si shell is not a solid film. Instead, it forms an oblique nanocolumnar structure with a pine-needle-like texture in which Si nanoneedles (of ~20 nm in diameter and ~170 nm in length) are anchored upward at the sidewall of the VACNFs. Clear open space and voids are visible between the Si nanoneedles. Interestingly, the TiO_2 shell forms a similar nanocolumnar structure, as shown in Figures 6.1c and 6.2a. Such unique structures represent the characteristic feature of the materials deposited by ion beam sputtering onto the VACNFs at low substrate temperatures (< 200° C), no matter using reactive gas or not. The open space allows Li^+ to access to Si or TiO_2 surface via much faster diffusion through the liquid electrolyte. The path length of slow chemical diffusion of Li^+ within the solid materials is reduced to ~ 10 nm (the radius of the nanocolumns). Such unique multi-scale integrated porous core-shell structure has been demonstrated to be the key for high-power and high-stability performance.[134, 144]

6.3.2 Silicon Coated VACNF Half-Cell

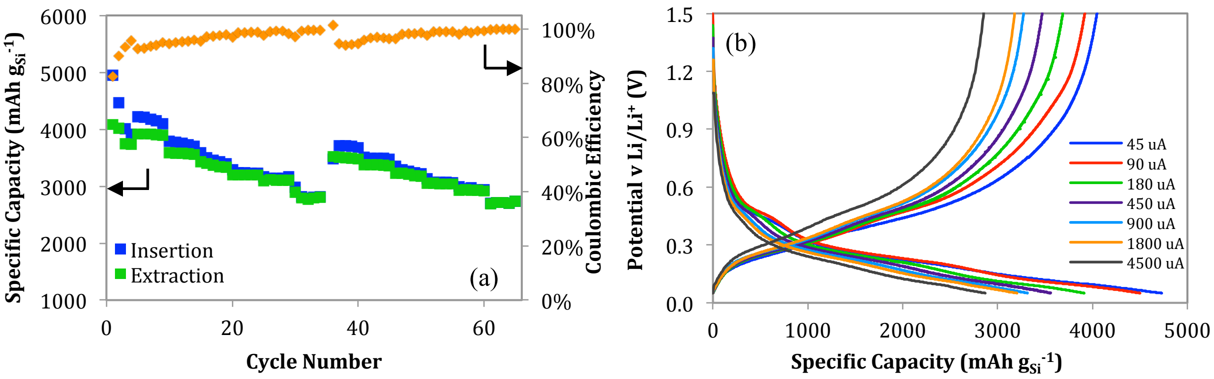

Figure 6.3 – (a) The rate performance of a Si-VACNFs half-cell during long cycling tests between 1.5 V and 0.05 V, showing the insertion and extraction capacities (left vertical axis) and coulombic efficiency (right vertical axis). (b) The galvanostatic charge-discharge profiles at various current rates from 90 μA to 4.5 mA (37.5 μA cm^{-2} to 1.9 mA cm^{-2}). All profiles were taken from the fifth cycle at each rate.

The half-cell electrochemical properties of Si-coated VACNFs as the LIB anode have been thoroughly characterized vs. a Li foil in our previous studies (Chapters 3 and 4).[134, 144] New measurements were carried out for a direct comparison with the cathode and full cell measurements to be discussed later. Figure 6.3a shows the electrode's cycling performance at various current rates. For ease of comparison with literature, current densities (normalized to the geometric area of Cu foils and the total Si mass of 0.254 mg) and commonly used C-rates specific to Si (i.e. C_{Si}) were all provided. The C_{Si} rates were calculated based on the maximum specific capacity for Li insertion into Si at room temperature (~3,800 mAh g_{Si}^{-1})[32] and the total Si mass on the electrode. The cell was initially applied with two Li insertion-extraction cycles at 45 μA (18.8 μA cm^{-2}, 0.18 A g^{-1}, C_{Si}/21.4) and 90 μA (37.6 μA cm^{-2}, 0.35 A g^{-1}, C_{Si}/10.7), respectively. Cycling at such low rates facilitated conditioning the Si shells and establishing the Solid-Electrolyte Interphase (SEI) layer, which was found to be crucial for achieving long-term cycling stability.[132-134] Similar to literature[32, 132-134, 144], a significantly higher quasi- Li insertion capacity of 4,956 mAh g_{Si}^{-1} than the extraction capacity of 4,087 mAh g_{Si}^{-1} was observed in the first cycle, which was attributed to the initial SEI formation and other side reactions.[144] After the fourth cycle, the Si-VACNF electrode became stabilized showing an extraction capacity of 3,742 mAh g_{Si}^{-1} which is close to the theoretical specific capacity of amorphous Si.[112]

To demonstrate the high-rate performance, the electrode was then subjected to two series of power tests (PTs), with the current increased in 6 steps from 90 μA (37.6 μA cm^{-2}, 0.35 A g_{Si}^{-1}, C_{Si}/10.7) to 4.5 mA (1.88 mA cm^{-2}, 17.7 A g_{Si}^{-1}, 4.7C_{Si} (or C_{Si}/0.21)) while five Li insertion-extraction cycles were applied at each step. From our previous studies (Chapters 3 and 4),[134, 144] these current rates are well within the safe range for Si-VACNF anode and will not cause any significant degradation. In the first power test series (Si-PT1), an average extraction capacity of 3,907 mAh g_{Si}^{-1} at 90 μA and 2,810 mAh g_{Si}^{-1} at 4.5 mA was achieved. The extract capacity only decreased by 28% as the current rate was increased by 50 fold. The second PT series (Si-PT2) gave only slightly lower extraction capacities of 3,502 mAh g_{Si}^{-1} at 90 μA and 2,712 mAh g_{Si}^{-1} at 4.5 mA, respectively. In each PT series, the coulombic efficiency gradually increased from ~93% to >99.5%, indicating that the electrode become more reversible after cycling.

The representative galvanostatic charge-discharge profiles of Si-PT2 series are shown in Figure 6.3b. The major Li insertion occurred between ~0.5 to 0.05 V and extraction between 0.15 and 0.6 V. Both the insertion and extraction curves showed tilt plateaus with larger slopes comparing to those of crystalline Si nanowires,[24, 32] indicating that the Si-VACNF electrode is dominated by a battery behavior (represented by the flat plateau) but mixed with some pseudocapacitive contributions (represented by the tilt linear lines). This can be attributed to the increase of fast surface reactions when the size of the Si nanoparticles is reduced, similar to the nanosize effects observed in high-rate Li intercalation in $LiCoO_2$ electrodes.[141, 143] As shown in Figure 6.1f and our previous studies (Chapters 3 and 4),[134, 144] the Si coating on VACNFs forms a pine-needle-like oblique nanocolumnar structure anchored on the VACNF sidewall, with substantial voids between the ~20 nm diameter Si nanoneedles. This porous structure is beneficial for high-rate reactions since Li^+ ions can access to larger Si surface via fast diffusion through the liquid electrolyte (with the Li^+ ion diffusion coefficient $D_{Li+} = (5\text{-}7)\text{x}10^{-11}\ cm^2\ s^{-1}$ in nanostructured Si[146] and $\sim 1\text{x}10^{-5}\ cm^2\ s^{-1}$ in volatile organic electrolyte) In contrast to literature, the nanosize of the Si grain in this study did not cause decrease in the Li storage capacity. The Si coating on VACNFs matches the full theoretical capacity, which is a highly desired property enabled by the good electrical connection through the highly conductive VACNF core. The unique architecture of the Si-VACNF electrode makes it capable to provide both high rate and high capacity, as demonstrated in Figure 6.3 and our previous studies[134, 144].

6.3.3 Titanium Oxide Coated VACNF Half-Cell

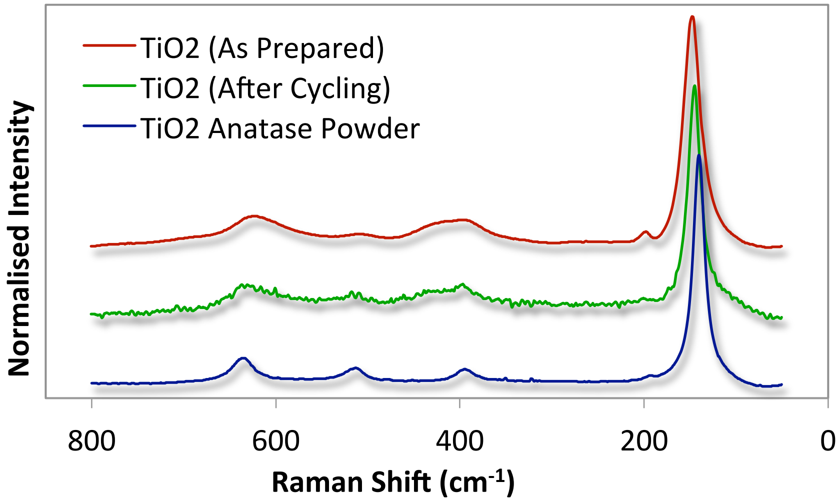

Figure 6.4 – Raman spectra of the TiO_2-coated VACNFs in as prepared form and after 1,650 charge-discharge cycles in half-cell test, compared to a pure anatase TiO_2 powder.

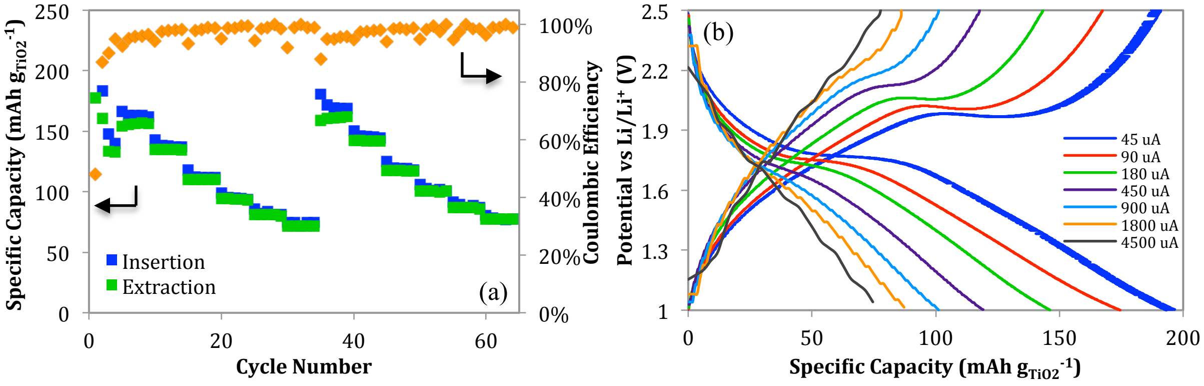

Figure 6.5 – (a) The rate performance of a TiO_2-VACNF half-cell during long cycling tests between 2.5 V and 1.0 V, showing the insertion and extraction capacities (left vertical axis) and coulombic efficiency (right vertical axis). (b) The galvanostatic charge-discharge profiles at various current rates from 45 µA to 4.5 mA (22.5 µA cm^{-2} to 2.25 mA cm^{-2}). All profiles were taken from the fifth cycle at each rate.

Since TiO_2 was deposited onto the VACNFs using a reactive ion sputtering process. Raman measurements confirmed that it formed anatase TiO_2 with characteristic peaks at Raman shift of 146, 382, 501, and 623 cm^{-1} (see Figure 6.4). There was no significant change in Raman spectrum even after the electrode was subjected to 1,650 charge-discharge cycles. Figure 6.5a shows the cycling performance of a TiO_2-VACNF electrode vs. a Li disk at various current rates. Similar to the Si-VACNF anode case, this cathode half-cell was initially applied with two Li^+

insertion-extraction cycles at 45 μA and 90 μA, respectively, to activate and stabilize the TiO_2 shell. The first cycle showed a very low coulombic efficiency of 48%, with an exceptionally high insertion capacity of 368 mAh g_{TiO2}^{-1} and a normal extraction capacity of 177 mAh g_{TiO2}^{-1}, indicating the presence of a significant amount of irreversible reactions. After 4 cycles, the electrode became stabilized, giving an insertion capacity of 163 mAh $(g_{TiO2})^{-1}$ and an extraction capacity of 156 mAh g_{TiO2}^{-1} at 90 μA current. According to literature[52, 57], the theoretical capacity of bulk anatase is 168 mAh $(g_{TiO2})^{-1}$ to reach the final lithiation form of Li_xTiO_2 (with $x = 0.5$). Smaller anatase TiO_2 nanoparticles below 30 nm in diameter present higher apparent Li storage capacity due to a larger pseudocapacitive contribution.[52, 57] Our measured extraction capacity at the lowest applied current (45 μA) exceeds the theoretical specific capacity, indicating that the entire TiO_2 shell was active in the core-shell structure. For ease of comparison, the measurement conditions in the following discussions are listed in multiple units, including electric currents, current densities (normalized to the 2.011 cm^2 geometric electrode area and the total TiO_2 mass of 0.352 mg), and TiO_2-specific C-rates (calculated using the theoretical specific capacity 168 mAh g_{TiO2}^{-1}).

The TiO_2-VACNF array was subjected to identical PTs as performed on the Si-coated VACNFs, with the current started at 90 μA (44.8 μA cm^{-2}, 0.26 A g_{TiO2}^{-1}, $1.5C_{TiO2}$) and increased in 5 steps to a final current of 4.5 mA (2.24 mA cm^{-2}, 12.8 A g_{TiO2}^{-1}, $76C_{TiO2}$). Since the specific capacity of TiO_2 is about 20 times lower than Si, the C_{TiO2} rate appeared remarkably higher than Si even though the current magnitudes were the same. At the highest current (4.5 mA), it took less than 1 min. to complete the charge or discharge process. In the first power test (TiO_2-PT1), a 90 μA current produced an average extraction capacity of 156 mAh g_{TiO2}^{-1} with a coulombic efficiency greater than 98%. At 4.5 mA current, the extraction capacity was 71 mAh

g_{TiO2}^{-1}, retaining ~46% of the low-current capacity. The coulombic efficiency was near 100% even at such high rates. The capacity was increased in the second power test (TiO_2-PT2), achieving 160 mAh g_{TiO2}^{-1} at 90 μA and 78 mAh g_{TiO2}^{-1} at 4.5 mA, indicating that the electrode was improved during cycling. The high stability at high current rates is consistent with the literature on thin-film electrodes (< 1 μm in thickness) made of TiO_2 nanoparticles.[57, 145]

6.3.4 Titanium Oxide Li^+ Storage Mechanism

TiO_2 is well known for dual Li^+ storage processes by means of bulk Li^+ insertion to form Li_xTiO_2 (with $x \leq 0.5$)[138] and pseudocapacitance via fast surface reactions.[56] The ratio of these contributions is largely determined by the particle size.[57] TEM images in Figures 6.1c and 6.2a clearly show that the TiO_2 coating also forms a polycrystalline nanocolumnar structure with ~20-30 nm diameter and ~170 nm long TiO_2 nanocolumns protruding out from the sidewall of the VACNFs. Similar to the earlier discussions on Si-coated VACNFs, the highly porous nanocolumnar structure allows Li^+ ions to access to larger TiO_2 surface via fast diffusion through liquid electrolyte and thus significantly reduces the diffusion lengths of Li^+ across solid TiO_2 materials. Thus higher reaction rates can be achieved due to greater pseudocapacitive contribution from surface reactions.[57] The mechanism of Li storage is reflected in the galvanostatic charge-discharge curves in Figure 6.5b. During lithium insertion starting at 2.5 V, a small plateau is seen at 1.75 V but is flanked by a sloping profile (down to the low limit at 1.0 V) corresponding to the pseudocapacitance that dominates the major portion of the charge storage. The process reverses upon extraction, with the potential profiles showing the dissipation of pseudocapacitive charge first until the extraction potential of TiO_2 is reached at ~2.0 V. After all lithium diffuses out from the bulk crystals to complete the phase transition from Li_xTiO_2 to TiO_2, the surface reaction dominates again and produces the pseudocapacitive curve up to 2.5 V.

It is noted that, as the magnitude of the current is raised, the capacity of Li^+ insertion decreases more rapidly than the pseudocapacitance and the curves become nearly linear lines at 4.5 mA current. At this high rate, the electrode is fully charged or discharged to its full capacity (78 mAh g_{TiO2}^{-1}) in only 22 seconds. The Li^+ diffusion length in TiO_2 can be calculated by

$$L = (Dt)^{1/2} \tag{6.1}$$

Using D_{Li+} = (3-5) x 10^{-15} cm^2 s^{-1} for the bulk anatase TiO_2 films,[138] the maximum thickness of TiO_2 that Li^+ ions can reach from the external surface is only 3.3 nm. Apparently, the rate of Li^+ insertion was limited by the very slow diffusion of Li^+ in solid TiO_2. The inner portion of the TiO_2 nanoparticles was not lithiated at the high rates. It is noted that the chemical diffusion coefficient of Li^+ in nanoporous TiO_2 film was reported to be mysteriously lower than the bulk value by 10 to 100 times,[57, 145] which needs to be better understood in the future. Thus we avoid using those values for the discussion here. Nevertheless, the nanocolumnar core-shell structure of TiO_2-coated VACNFs maximized the portion of TiO_2 that Li^+ can be inserted into and provided additional surface reactions. The latter factor was responsible for the high specific capacity of Li extraction in TiO_2-VACNF electrode, 177 mAh g_{TiO2}^{-1} (or 637 C g_{TiO2}^{-1}) at 45 μA, exceeding that of an ultrathin film of 7-nm-dia. TiO_2 nanoparticles.[57] This value corresponds to a specific capacitance of ~ 425 F g_{TiO2}^{-1} assuming that the cell operates as an asymmetric supercapacitor between 1.0 to 2.5 V, matching the performance of the best supercapacitors. It can be concluded that this electrode material can perform both as a battery with high capacity at low rates and a pseudocapacitor with high power at high rates, based on different aspects of Li chemistry. However, the specific Li^+ storage capacity is much lower that the Si-VACNF electrode (177 mAh g_{TiO2}^{-1} vs. ~3,500 mAh g_{Si}^{-1} at 45 μA).

6.3.5 Silicon–Titanium Oxide Full Cell Battery

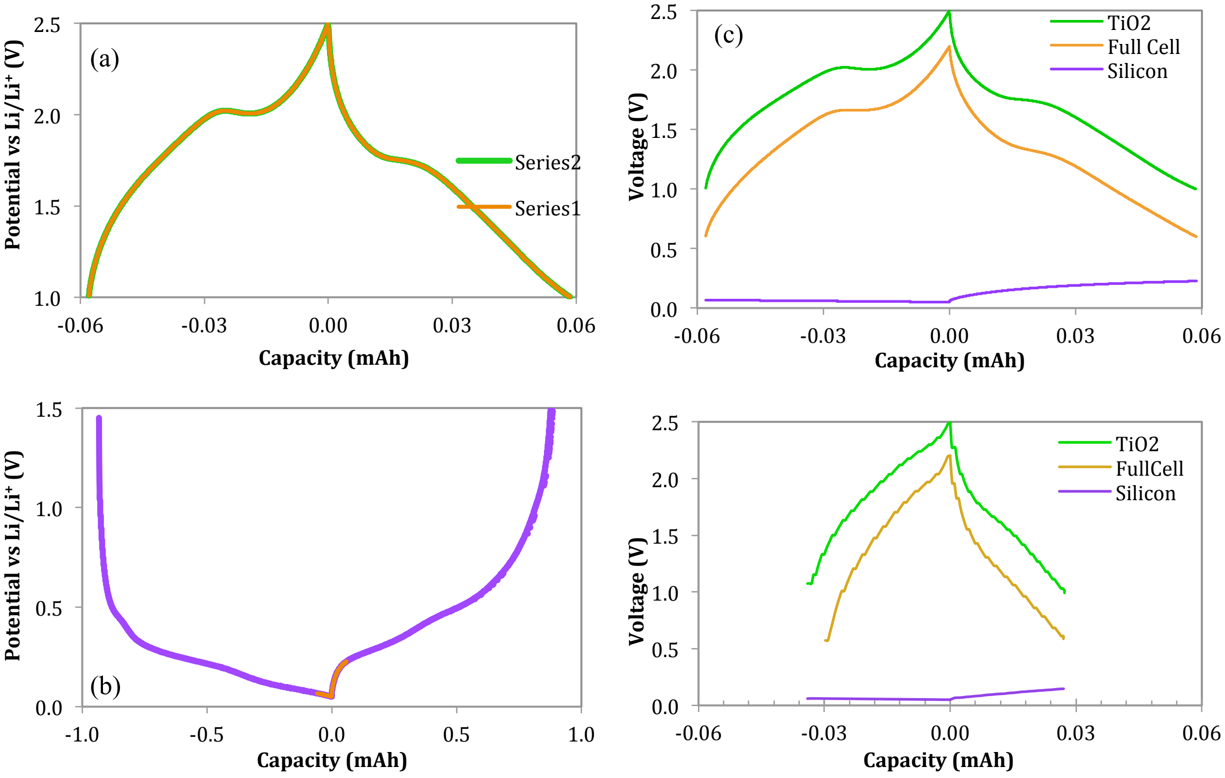

Figure 6.6 – Individual half-cell voltage profiles of (a) a TiO_2-VACNF electrode (green line) and (b) a Si-VACNF electrode (purple line). The portion of the electrodes used in the full cell is highlighted by gold line. All measurements performed at 90 µA. Half-cell voltage profiles of TiO_2-VACNFs and Si-VACNFs compared to profile of Si-TiO_2 full-cell hybrid at (c) 90 µA and (d) 1.8 mA.

As shown in the above half-cell studies, the VACNFs serve well as a nanostructured current collecting core to effectively connect to all active shell materials, permitting utilization of their maximum lithium storage capabilities while maintaining the integrity of the 3D composite structure without using additives or binders. The core-shell architectures with both Si and TiO_2 coatings on the VACNFs behave as battery-pseudocapacitor hybrids. The Si-coated VACNFs consist of more contributions from battery-like lithium insertion/extraction while TiO_2-coated VACNFs are dominated by pseudocapacitive surface reactions. It would be interesting to see the performance of a full cell combining a Si-VACNF anode and a TiO_2-VACNF cathode.

Table 6.1 - Specifications of Full Cell Electrode Materials

Electrode	**Anode**	**Cathode**	**A/C ratio**
Active Electrode Materials	**Si**	**TiO_2**	
Nominal Thickness (nm)	456	500	~1:1
Geometric Area (cm^2)	2.4	2.0	1.2:1
Density ($g\ cm^{-3}$)	2.33	3.50	0.67:1
Mass m (mg)	0.254	0.352	0.72:1
Theoretical Capacity Density ($mAh\ g^{-1}$)	3,800 [a]	168 [b]	22.6:1
Available Capacity (mAh)	0.965	0.059	16.3:1
Diffusion Coefficient D_{Li+} ($cm^2\ s^{-1}$)	$(5\text{-}7)\text{x}10^{-11}$ [c]	$(3\text{-}5)\text{x}10^{-15}$ [d]	15k:1
Max. Diffusion Length in 1 min (nm) [e]	648	5.5	

Note: [a] From reference.[32] [b] From reference.[52, 57] [c] From reference.[146] [d] From reference.[138]
[e] Calculated by Eq. (1) with t = 60 s.

It is noteworthy that the full-cell performance depends not only on the properties of each electrode materials, but also on the capacity ratio between them.[147] Table 6.1 lists various parameters of the Si-VACNF and TiO_2-VACNF electrodes deposited with ~500 nm nominal thickness of active materials. Due to the large difference in the specific capacity, the available Li^+ storage capacity of the Si electrode is about 16 fold of that of the TiO_2 electrode (0.965 mAh vs. 0.059 mAh), though the mass of the active materials is about the same. As a result, the capacity of the full-cell is limited by the TiO_2 cathode. As illustrated in Figure 6.6c, the charge and discharge processes only caused a minimal potential change (< 0.20 V) in the Si-VACNF anode while the potential of the TiO_2-VACNF cathode varied in the full range of ~1.5 V. The utilized portion of the Si half-cell profiles relative to the full capacity of both electrodes is further elaborated in Figure 6.6. The full cell charge-discharge profile at 90 μA current in Figure 6.6c not only matches the full half-cell capacity of TiO_2 (0.058 mAh), but also reflects the exact shape of the TiO_2 half-cell profile. The cell voltage varies between 0.60 V and 2.15 V, about 0.1 to 0.3 V lower than the difference between the two half-cell profiles. At a higher current of 1.8 mA as shown in Figure 6.6d, the potential change at the Si anode in the half-cell is even smaller (< 0.1 V) and the full-cell capacity drops to ~0.027 mAh in correlation with the TiO_2 half-cell capacity.

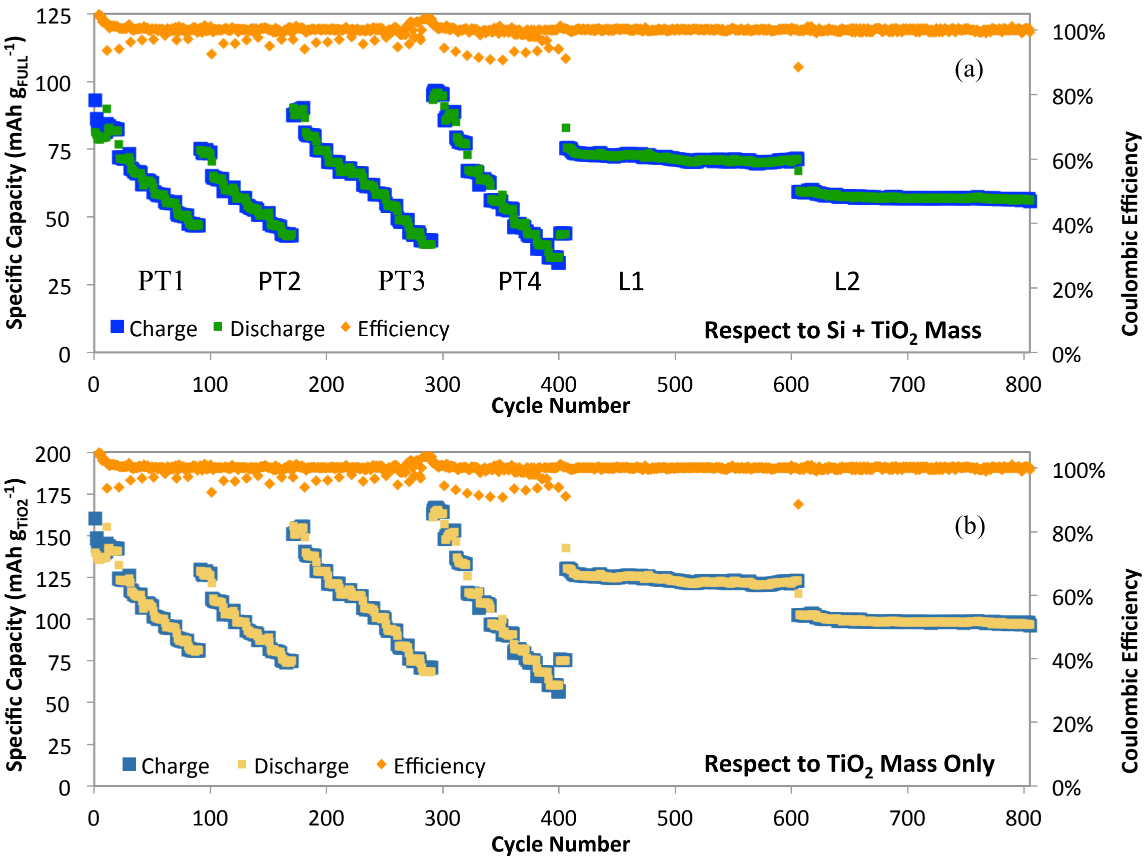

Figure 6.7 – (a) Cycling performance of Si-TiO_2 full cell over 800 charge-discharge cycles at various current rates, showing charge (🟩) and discharge (🟦) capacities with respect to the total mass of active materials of cell (Si + TiO_2) and Coulombic efficiency (🔶). (b) Cycling performance of Si-TiO_2 full cell, showing charge (🟦) and discharge (🟨) capacities with respect to TiO_2 mass only and Coulombic efficiency (♦).

For the full cell, the specific capacity is calculated by dividing the total mass of Si and TiO_2, i.e. 606 μg. Thus the value is lower than that of the TiO_2 half-cell. Increasing the TiO_2 mass loading would give higher specific capacity for the full cell, which can be achieved by using longer VACNFs and thicker TiO_2 layers. However, this may be at the cost of an important advantage in cell assembly. It needs to be noted that sufficient Li needs to be loaded in the electrode materials before cell assembly. In most commercial LIBs, lithiated cathodes with higher Li capacity than the anode serve as the Li source and the cells are assembled in the discharged state.[148] In this study, a fully lithiated Si anode was assembled with a pristine TiO_2 cathode to form a full cell in the charged state. The overwhelming Li capacity pre-stored in the

Si anode ensured that plenty of Li^+ ions were available to flood into the TiO_2 cathode and to compensate other side reactions during the first discharging process. Since only a small portion of the Li in the lithiated Si was involved in later charge-discharge processes, the Si anode in such full cells was much more stable than that in the half-cell tests.

Similar cycling procedures to the earlier half-cell tests were applied on the VACNF supported Si-TiO_2 full cells. The specific capacity normalized to the total mass of Si and TiO_2 (represented by the unit mAh g_{full}^{-1}) and TiO_2 alone (represented by the unit mAh g_{TiO2}^{-1}) for over 800 cycles are presented in Figure 6.7. The cell was first galvanostatically discharged from an open circuit voltage (OCV) of ~1.7 V to 0.6 V at 75 μA, giving an extremely high capacity of 0.093 mAh (154 mAh g_{full}^{-1}) which exceeded the theoretical TiO_2 half-cell capacity (0.059 mAh). The cell was then charged-discharged for ten cycles at 75 μA between 0.6 V and 2.0 V to become stabilized at specific capacities of 79.6 and 81.5 mAh g_{full}^{-1} for charge and discharge respectively, with the coulombic efficiency nearly 100%. The Si-TiO_2 cell was subjected to four PT series, with the current stepwise increased from 75 μA (37.3 μA cm^{-2}, 1.3C_{TiO2}) to 4.5 mA (2.24 mA cm^{-2}, 76C_{TiO2}) with 10 charge-discharge cycles at each rate. It is noted that the current density was calculated using the geometric surface area of TiO_2-VACNF disk and C_{TiO2} stands for the C-rate calculated by TiO_2 mass alone, since TiO_2-VACNF was the limiting electrode.

Finally two tests of ~200 cycles each were applied at 240 and 600 μA, respectively. As shown in Figure 6.7, the results are highly reproducible with negligible changes over 800 cycles. The coulombic efficiency maintained at ~100% except in the first cycles when the current was changed. The upper and lower voltage limits were varied in PT1 and PT2 tests to find that the optimum voltage window (2.2 to 0.6 V) for obtaining the maximum capacity, which were employed in the remaining cycles.

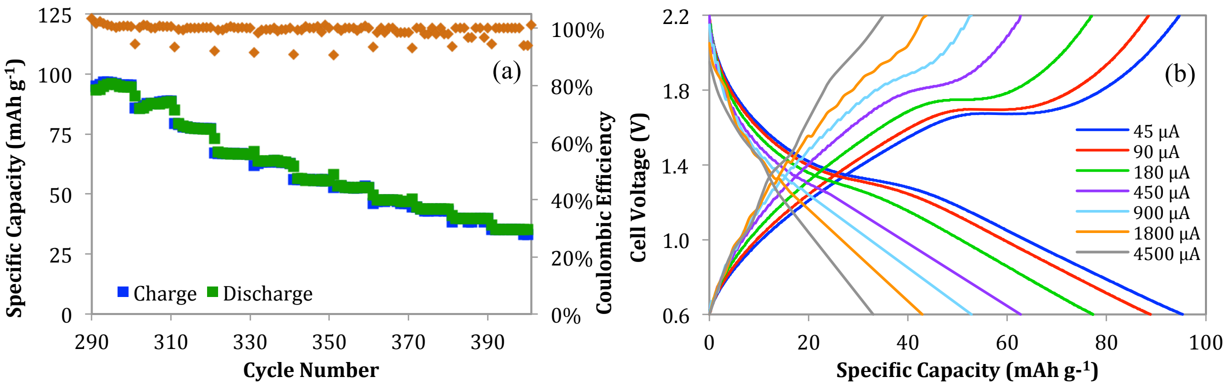

Figure 6.8 – (a) Cycling performance of Si-TiO$_2$ full cell, operating from 2.2 V to 0.6 V, showing charge (🟦) and discharge (🟩) capacities (left vertical axis) and Coulombic efficiency (🔶) (right vertical axis). (b) Charge-discharge curves of Si-TiO$_2$ full cell at various currents from 45 μA (1C) to 4,500 μA (225C).

Figure 6.8a shows the characteristics of PT4 of the full cell between 2.2 to 0.6 V, with the current ranging from 45 μA to 4.5 mA. At the lowest current of 45 μA, the cell achieved its highest capacity of 0.0575 mAh (94.9 mAh g_{full}^{-1}) which was 97.4% of the cell's theoretical capacity 0.059 mAh (97.4 mAh g_{full}^{-1}) limited by the TiO$_2$ cathode. At the highest current of 4.5 mA, a respectable capacity of 0.020 mAh (33.0 mAh g_{full}^{-1}) was measured, retaining ~34% of the full capacity. Since it took only 16 seconds to complete the full charge or discharge at 4.5 mA, the cell essentially operated as a supercapacitor. The charge-discharge curves of the Si-TiO$_2$ full-cell at different current rates are shown in Figure 6.8b. The full-cell profiles closely resemble the profiles of the TiO$_2$ half-cell at all current rates, but the characteristic charging plateau at 45 μA shifted downward from 2.0 V to 1.7 V, and the discharge plateau shifted from 1.75 V to ~1.4 V. At higher currents, the full-cell voltage profiles become nearly linear, clearly dominated by the fast pseudocapacitive contribution.

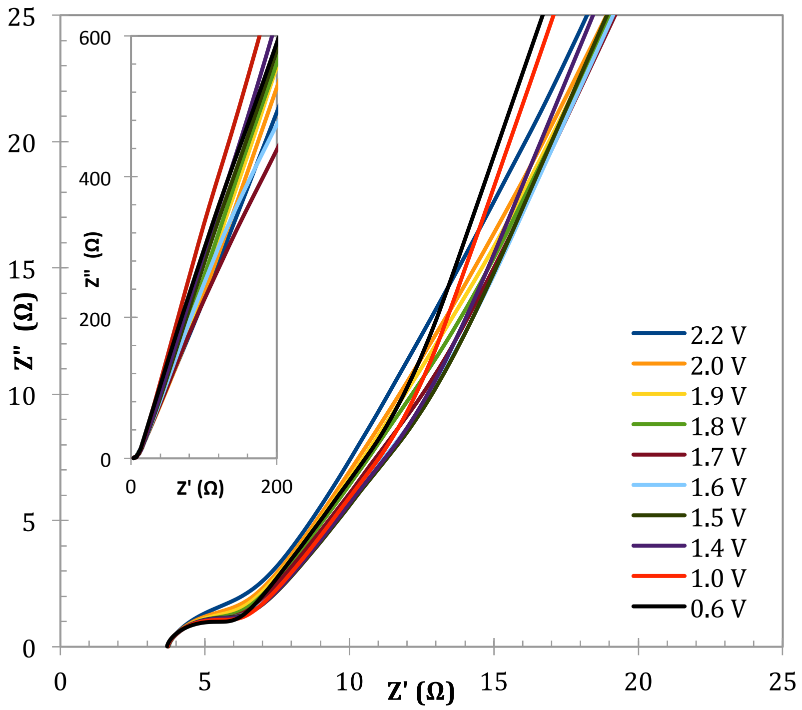

Figure 6.9 – Nyquist plot of the electrochemical impedance spectra (EIS) of the Si-TiO_2 full-cell after going through 400 charge-charge cycles. Each spectrum was measured at a static voltage varied from 0.6 V to 2.2 V using a CHI 760D potentiostat (CH Instruments, *Austin, TX)* with a 5 mV_{pp} AC voltage over a frequency range from 100 kHz to 0.01 Hz. The inset is an expanded view of the spectra.

Electrochemical impedance spectroscopy (EIS) with the Si-TiO_2 full cell after 400 charge-discharge cycles further confirmed that the properties of the full cell were dominated by the TiO_2-VACNF cathode. The Nyquist plots of EIS measured at the cell voltages from 0.6 V (fully discharged state) to 2.2 V (fully charged state) are dominated by a quasi-straight line slightly tilt off from the vertical axis (see inset of Figure 6.9), representing the pseudocapacitor feature. A very small semicircle was only visible after zooming into the high frequency region close to the origin (see Figure 6.9), indicating the small contribution of bulk faradaic reaction associated with Li insertion/extraction. At higher cell voltages, the Nyquist curve shifts toward a vertical line, closer to the feature of an ideal pseudocapacitor.

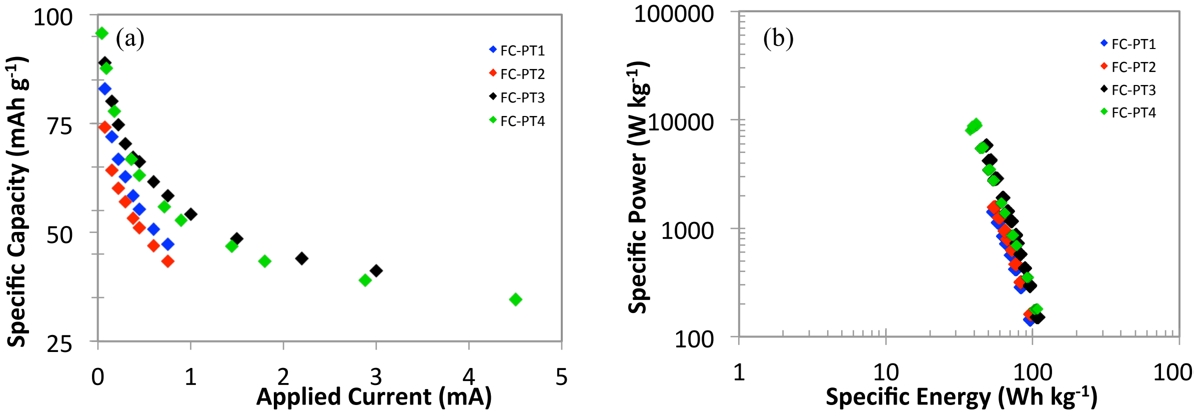

Figure 6.10 - (a) The specific capacity of the Si-TiO$_2$ full-cell versus applied current. (b) Ragone plot of the Si-TiO$_2$ full-cell operated at various currents, producing a corresponding specific energy and specific power capabilities.

As shown in Figure 6.8, the galvanostatic charge-discharge curves of the Si-TiO$_2$ full cell supported on VACNFs represent the hybrid feature of a battery (with a simple flat plateau) and an asymmetric pseudocapacitor (with a linear line). The method for calculating the specific energy and specific power is thus different from that in literature[10, 13] for either batteries or supercapacitors, but can be derived from the fundamental principles. Here the delivered specific energy (E, in the common unit Wh kg^{-1}) is calculated from the V-t data in the discharge curve by:

$$E = \left(\int_{Q=0}^{Q_{max}} V\times dQ\right)/m = \left(\int_{t=0}^{t_{max}} V\times I\times dt\right)/m \qquad (6.2)$$

where V is the cell voltage, Q the stored charge, t the charging time and m the total mass of Si and TiO$_2$. The average specific power (P_{avg}, in the common unit W kg^{-1}) is simply the total delivered specific energy divided by the maximum discharge time (t_{max}):

$$P_{avg} = {}^{E}/_{t_{max}} = \left(\frac{\int_{t=0}^{t_{max}} V*I*dt}{m}\right)/\; t_{max} \qquad (6.3)$$

Figure 6.10a shows that the specific discharge capacity of the Si-TiO$_2$ full cell decreased as the current was raised from 45 μA to 4.5 mA in all four PT series. This is a common phenomenon for both batteries and supercapacitors. Interestingly, the cell capacity increased after long cycling and it was able to retain 36% of the capacity as the current was increased by

100 times. Figure 6.10b further illustrates the full cell performance in Ragone plot, i.e. the specific power vs. specific energy. While the delivered specific energy (40-103 Wh kg^{-1}) matches that of a decent battery, the highest average power (8,830 W kg^{-1}) is nearly two orders of magnitude higher than the best batteries.[10] It is noted that, in literature, the maximum delivered power (P_{max}) for a single supercapacitor electrode is calculated by:

$$P_{max} = \frac{V}{4mR_s} \tag{6.4}$$

where R_s is the equivalent series resistance (ESR) defined by the internal electronic and ionic resistance.[13, 149] This method apparently gives much higher value in power density. For fair comparison, we adapt this method by using the total mass of Si and TiO_2 as m and the R_s value determined by the small voltage jump $\Delta V = 2IR_s$ when the polarity of the current was flipped during the charge-discharge transition. Figure 6.11 shows the Ragone plot derived by this method, which represents the high limit of the power performance. The values are in the range of 26,000 to 56,000 W kg^{-1}, matching the high limit of the state-of-the-art supercapacitors.[149] Importantly, the ratio of the load resistance (R_L) to R_s in all these measurements was high, from ~12:1 to ~700:1, and the internal energy consumption by heat dissipation is negligible in this range.[13] More than 92% of the stored energy was delivered to the external load even at the highest current (4.5 mA).

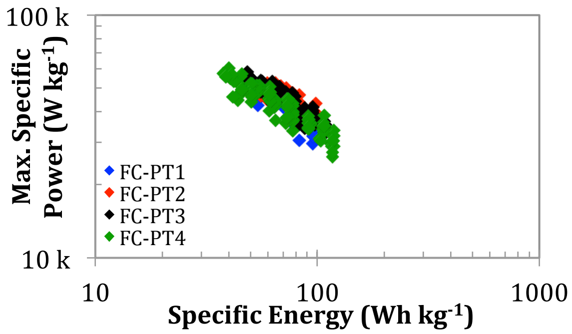

Figure 6.11 - The maximum power density calculated by Equation (6.4) versus the specific energy calculated by Equation (6.2)

6.4 Conclusions

In conclusion, we have demonstrated a unique lithium ion battery based on a Si anode and a TiO_2 cathode, both in form of nanocolumnar shells coated on vertically aligned carbon nanofiber arrays which serve both as the 3D structural support and as an effective current collector. The active materials in each electrode have matched their full theoretical Li^+ storage capacities with significantly improved cycle stability and high-power capability comparing to their bulk counterparts, attributed to the unique core-shell nanostructure. The charge-discharge profiles of both half-cells and the full cell resemble the hybrid feature of a battery (with a flat plateau) and a supercapacitor (with a tilt linear line), indicating the significant pseudocapacitive contribution by fast faradaic reactions at the outer surface or a thin layer near the surface of Si and TiO_2 nanocolumns. The electrodes behave closer to a battery at low current rates but become more like a pseudocapacitor at high current rates. The properties of the full cell can be also tuned from a battery to a pseudocapacitor by changing the capacity ratio between the two electrodes. The Si-TiO_2 full cell showed a high specific energy (103 Wh kg^{-1} at the low current density of ~74 mA g_{full}^{-1}), comparable to a decent battery, and a remarkable specific power (56,000 Wh kg^{-1} at the high current density of ~7.4 A g_{full}^{-1}) reaching the limit of the state-of-the-art supercapacitors. Using a cathode material matching the properties of the Si anode will lead to further optimization of the full-cell performance.

Chapter 7 - Higher-Power Supercapacitor Electrodes Based on Mesoporous Manganese Oxide Coating on Vertically Aligned Carbon Nanofibers

Reprinted with permission from The Royal Society of Chemistry from S. A. Klankowski, G.P. Pandey, G. Malek, C. R. Thomas, S. L. Bernasek, J. Wu, J. Li, Nanoscale, 2015, Advance Article, DOI: 10.1039/C5NR01198A

7.1 Introduction

Hydrous ruthenium oxide (RuO_2) is one of the foremost supercapacitor electrode material due to its high theoretical specific capacitance (SC) (>1,300 F g^{-1}), high electrical conductivity (~1 x 10^2 S cm^{-1}), and long-term cycle stability.[150] However, due to the high production cost and known environmental toxicity, practical applications of RuO_2 have been limited and other materials are being actively pursued as alternatives. Among them, manganese oxides (MnOx) have received the most attention in part due to their abundance, low cost and benign nature. The theoretical SC value of MnO_2 is 1,370 F g^{-1} for a redox process involving one electron per Mn atom,[76] which is comparable to hydrous RuO_2 in terms of reaction mechanism. MnO_2 is also very similar to RuO_2 with its pseudo-capacitance behavior derived via proton or alkali metal cation (C^+) insertion into the lattice structure during reduction processes[76, 151]:

$$MnO_2 + e^- + H^+ \leftrightarrow MnOOH, \tag{7.1}$$

$$MnO_2 + e^- + C^+ \leftrightarrow MnOOC, \tag{7.2}$$

with the cation C^+ being K^+, Na^+, or Li^+. Additionally, it has been proposed that surface adsorption of electrolyte cations C^+ may also contribute[151] through:

$$MnO_2 + e^- + C^+ \leftrightarrow (MnO_2^-C^+)_{surface} \tag{7.3}$$

with the reaction rate determined by the balance of electron and ion transport rates in the electrode materials. Despite the likeness in reaction mechanisms, MnO_2 (and many other metal oxides) has a much lower electrical conductivity than RuO_2 (with σ_{MnO_2} = ~10^{-5}-10^{-6} S cm^{-1} versus σ_{RuO_2} = ~1 x 10^2 S cm^{-1}, differentiated by 7-8 orders of magnitude),[152, 153] while the diffusion coefficients of protons and alkali cations in MnO_2 (D_{H^+} = 6 x 10^{-10} cm^2 s^{-1} and D_{Na^+} = ~ 5 x 10^{-10} cm^2 s^{-1})[76, 154] are greater than those in RuO_2 (D_{H^+} = 5 x 10^{-14} cm^2 s^{-1}).[152, 155-158] Overall, the effective reaction rate in the bulk MnO_2 material was found to be much less than its RuO_2 counterpart because only a limited fraction of bulk MnO_2 was electrically connected and active in electrochemical reactions.[76] The low electrical conductivity also restrained the applicable power rate of the bulk MnO_2 electrodes.

To date, the highest reported SC value of 1,380 F g^{-1} for MnO_2 was measured at a very slow scan rate of 5 mV s^{-1},[76] which is not meaningful for practical applications and opts to be augmented by other redox reactions. Making MnO_2 into thinner films and incorporating binders and conductive additives have been adopted to improve the overall rate performance, but this always comes at the expense of the total specific energy. In particular, due to the sluggish proton and cation diffusion rates, the electrochemical reaction of MnO_2 may be limited to the surface layer of only several nanometers at fast charge-discharge rates (on a timescale of seconds), which significantly reduces the obtainable specific capacitance.[67, 76, 154] Hence, for MnO_2-based electrodes to outperform RuO_2-based supercapacitors, the electrode design must provide a very high active surface area along with effective electrical connectivity through the entire MnO_2 material while maintaining electrode's robustness to endure tens-of-thousands of charge-discharge cycles. Hence, MnO_2 were also synthesis in the various nanostructures to improve its electrochemical performance as supercapacitor electrode material.[159-162]

One more promising approach to fulfilling the above requirements is to create a three-dimensional (3D) core-shell hybrid architecture consisting of thin MnO_2 shells on stable conductive nanostructured cores.[152] Carbon nanotubes (CNTs), due to the nanoscale fiber-like structure, high electrical conductivity, and good chemical stability, have been recognized as an attractive core material to improve current collection, as demonstrated in the intensive studies of CNTs as EDLC materials.[67, 163] Various CNT/MnO_2 composites[164-166] or thin MnO_2 coating on dense, randomly stacked CNT films[167-169] have demonstrated rather high SC value varying from ~100 to ~600 F g^{-1} at scan rates up to hundreds of millivolts per second in cyclic voltammetry (CV) or at current density up to tens of amperes per gram in galvanostatic charge-discharge measurements. Generally, only ultrathin MnO_2 coatings of a few nanometers on CNT surfaces can afford both the high SC and high charge-discharge rates, which is presumably limited by the high contact resistance between CNTs. The MnO_2 coating sandwiched between CNT films would make the overall film resistance even higher.

Alternatively, vertically aligned CNTs were explored as a binder-free 3D current collector where all CNTs were directly anchored on a common conductive surface.[127, 170] MnO_2 has been electrochemically deposited as flower-like nanoparticles along the CNTs [171] or filled between CNTs.[170] However, the SC value and charge-discharge rate are not much better than the randomly stacked CNTs. In contrast, we have previously demonstrated another type of 3D hybrid architecture based on electrodeposition of a uniform 7.5-nm compact MnO_2 film on vertically aligned carbon nanofibers (VACNFs).[92] With additional MnO_2 mass loading by electrodeposition, the specific capacitance value showed signs of decreasing, which can be attributed to the reduced electrical connection and slowing down of mass transport as the layer thickness increases.

VACNFs are a special type of multi-walled CNTs grown by plasma enhanced chemical vapor deposition (PECVD), which consist of a stack of conical graphitic cups instead of concentric seamless tubes.[79-81, 85] The abundant active broken graphitic edges at the sidewall of VACNFs were found to be the key in enabling uniform MnO_2 deposition and formation of an effective electrochemical interface.[92] As a result, a high SC value of ~350 F g^{-1} was obtained at high scan rates up to 2,000 mV s^{-1}; however, the SC value tended to decrease as a thicker MnO_2 was deposited, limiting the overall energy density.[92] Here we extend this unique core-shell electrode architecture too much thicker MnO_2 coatings of over 200 nm in radial thickness. Particularly, a mesoporous manganese oxide shell with nanoscale rose-petal-like structure was formed by electrochemical oxidation of the sputtered Mn shell on the VACNF scaffold, as illustrated in Figures 7.1a and 7.1b. The mesoporous MnO_2 structure provides a significantly enhanced solid/liquid interface inside a larger electrode volume, allowing protons and other cations to access the whole MnO_2 material through fast diffusion in solution instead of moving across the solid MnO_2 materials. The ion diffusion length across the MnO_2 petals is less than ~ 10 nm. Consequently, a remarkable high-rate performance was obtained.

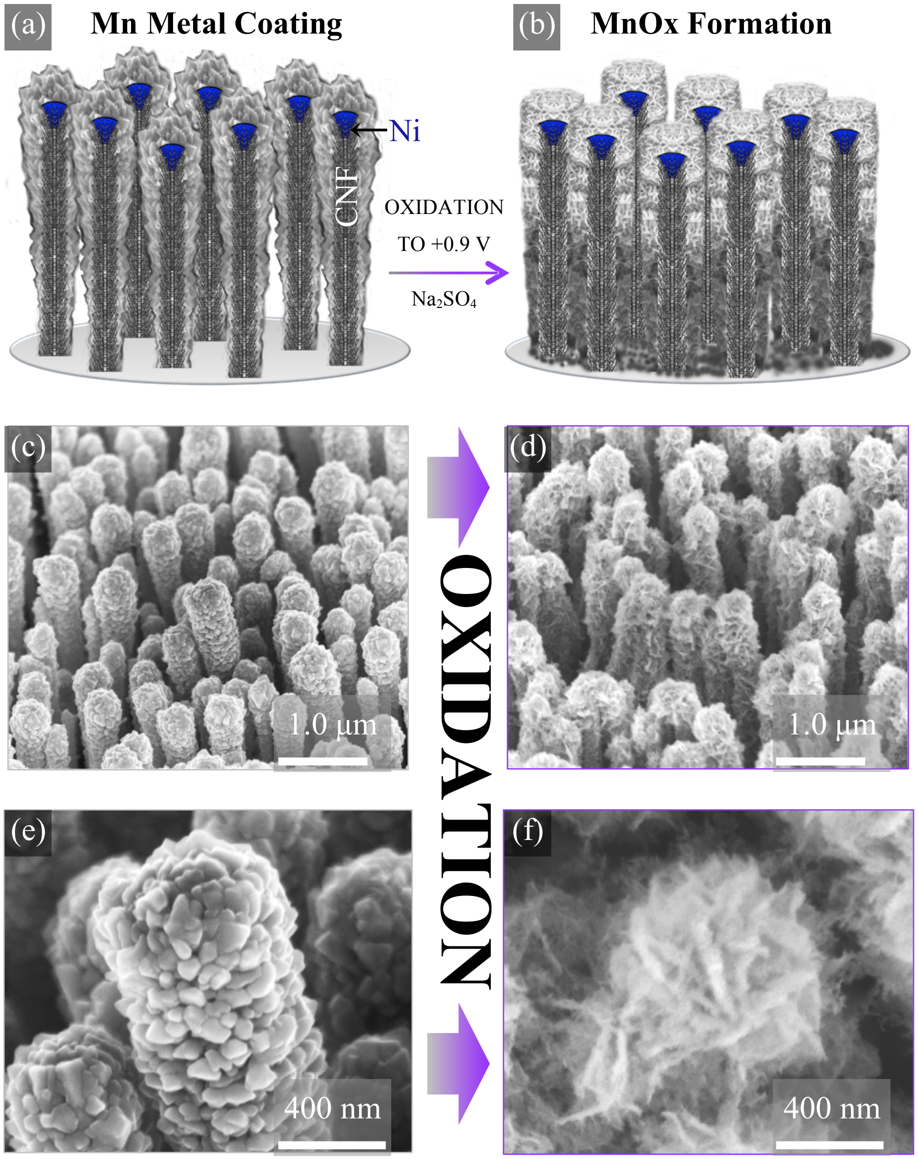

Figure 7.1 – Schematic of Mn-coated VACNFs (a) before and (b) after electrochemical oxidation in 1 M Na_2SO_4. Representative SEM images of 300 nm nominal Mn thickness at different magnifications with (c) & (e) before oxidation and (d) & (f) after oxidation.

.

7.2 Experimental Details

7.2.1 Electrochemical Oxidation and Charge-Discharge Tests

The electrochemical oxidation and cycling tests of the Mn-coated VACNF arrays were performed using a Teflon cell sealed against the Mn-coated VACNF array with an O-ring, leaving a total area of 1.39 cm^2 exposed. The electrolyte for this experiment was 1.0 M Na_2SO_4

solution prepared with 18.2 MΩ deionized water. All measurements were conducted by a three-electrode configuration in 6.0 mL of electrolyte with the Mn or MnO_2-coated VACNF array as the working electrode, an Ag/AgCl (4 M KCl) reference electrode, and a Pt foil counter electrode. The initial Mn coating was oxidized by chronopotentiometry method from the open circuit potential (~ −1.3 V) to the maximum potential of +0.9 V vs. Ag/AgCl (4 M KCl).[72] The electrolyte was quickly replaced with new solution after oxidation and CV measurements were then performed from 0.0 V to 0.8 V with a scan rate varying from 1.0 mV s^{-1} to 2000 mV s^{-1}. Chronopotentiometric charge-discharge tests were performed at various currents from 0.28 A g^{-1} to 140 A g^{-1} (44.2 μA to 22.5 mA total, respectively). Electrochemical impedance spectroscopy (EIS) measurements were performed from 100 kHz to 10 mHz, at an amplitude of 5.0 mV and a bias of 0.4 V. All electrochemical measurements were conducted with a CHI 760D Electrochemical Workstation (CH Instruments, Austin, TX).

7.2.2 Electron Microscopy and X-ray Photoelectron Spectroscopy Characterization

The structures of the electrodes before and after electrochemical testing were examined by SEM (FEI Nano 430), and transmission electron microscopy (TEM) (FEI Tecnai F20 XT). All electrodes were removed from Teflon cell in the discharged state (0.0 V), rinsed with copious amounts of deionized water to remove any remaining Na_2SO_4 salt from the electrode, and dried in a vacuum oven at ambient temperature. Surface analysis was done by XPS using the VG ESCALAB MkII system with a Phi 04-548 dual anode X-ray source. A Mg Kα line (1253.6 eV) generated at 15 kV and 300 W was used in this study. Survey scans used a pass energy of 100 eV, a step of 0.5 eV, and a dwell time of 200 ms. High-resolution core-level scans employed a pass energy of 20 eV, a step of 0.05 eV, and a dwell time of 500 ms.

7.3 Results and Discussion

7.3.1 Structural Characterization of MnO_2-VACNF Electrode

As demonstrated in our earlier studies,[92, 116, 134] the VACNF array provides a unique 3D platform to support a variety of active materials that can be deposited onto to the CNFs by either physical or chemical methods. With their unique cup-stacking graphitic structure and a diameter of 100-200 nm, the individual CNFs provide a mechanically robust scaffold, able to retain the integrity during Mn deposition and subsequent wet electrochemical processes. The CNFs are well separated and vertically aligned, forming a non-entangled brush-like structure that provides a stable Ohmic contact with the substrate.[79, 81, 85] The CNFs are known for excellent electrical conductivity along the axis ($\sim 2.5 \times 10^3$ S cm^{-1}, about 25 fold of the conductivity of RuO_2), serving to facilitate fast electron transport to and from the active materials.[84] Unlike the smooth sidewalls of a CNT, the edges of the graphitic cups create surface irregularities along the fiber surface that facilitated nucleation of the Mn flux during sputtering and provided active sites for fast electron transfer at the Mn/CNF interface. The larger, open space between the VACNFs enabled greater amounts of Mn metal to be deposited onto each CNF, forming a thick coaxial shell that was both electrically and chemically connected to the CNF.

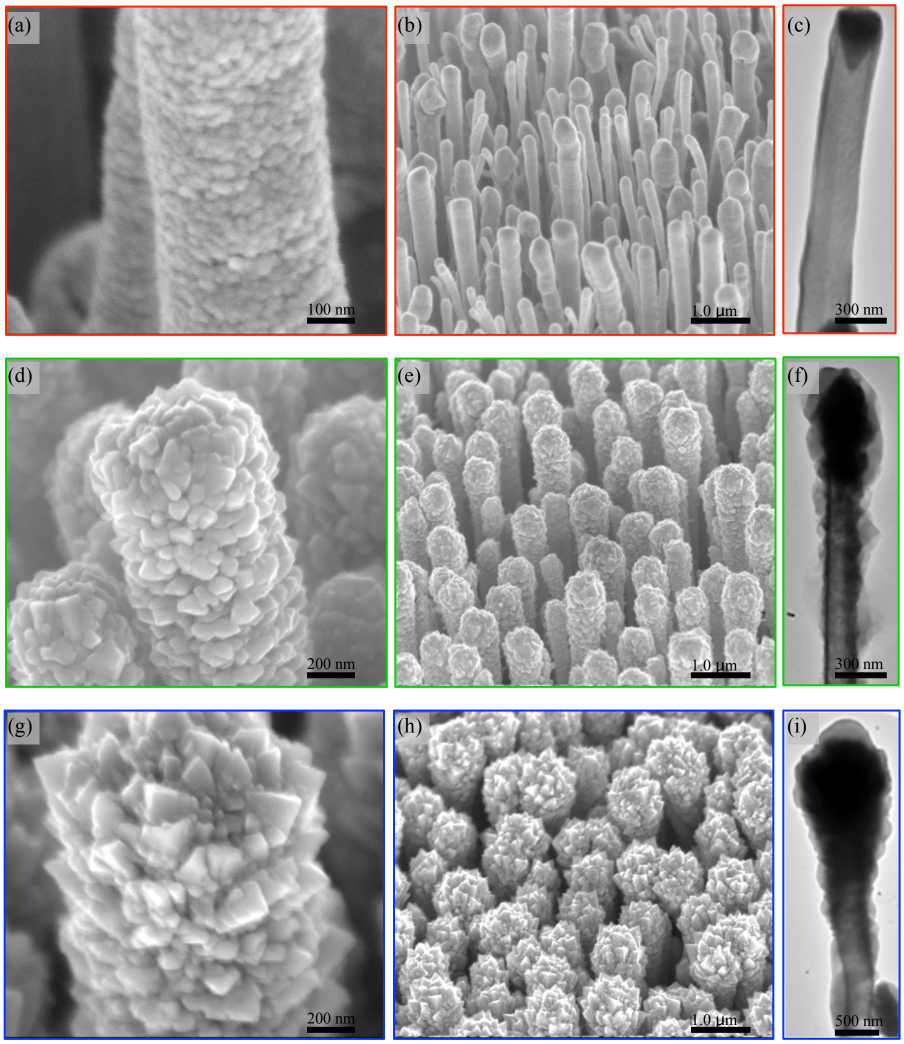

Figure 7.2 – SEM and TEM of the Mn-coated VACNFs just after Mn sputtering to various nominal thicknesses of (a-c) 100nm, (d-f) 300 nm , and (g-i) 600 nm. Scale bars are 100 nm, 1.0 µm, 300nm; 200 nm, 1.0 µm, 300nm; 200 nm, 1.0 µm, 500nm, respectively.

In this study, Mn metal at the nominal thickness of 100 nm, 200 nm, 300 nm, or 600 nm was sputtered onto the VACNF in order to obtain the maximum specific energy at high specific power. Figures 7.1c–f show representative SEM images of the as-sputtered Mn-coating (at 300 nm nominal thickness) on a VACNF array before (Figures 7.1c and 7.1e) and after electrochemical oxidation (Figures 7.1d and 7.1f). The Mn sputtering process deposited a coaxial shell consisting of Mn nanoparticles. At 100 nm nominal Mn deposition thickness, the Mn shell was found to be rather uniform along the CNFs, with a radial thickness of ~40 nm. At 300 and 600 nm nominal Mn deposition, the shell thickness increased to ~130 and ~200 nm, respectively (Figure 7.2). The Mn nanoparticles appeared to wrap along the whole length of CNFs but with larger shell thickness at locations nearer the CNF tip where Mn flux was the greatest during deposition (Figures 7.2b, 7.2e, and 7.2h). The Mn nanoparticles appeared to be crystalline in-nature, with sizable facets and lattice edges broken up by small crevasses that penetrated deep to the core. All these features provided a large surface area and high porosity, which allowed the electrolyte to effectively access the whole Mn shell in the next step.

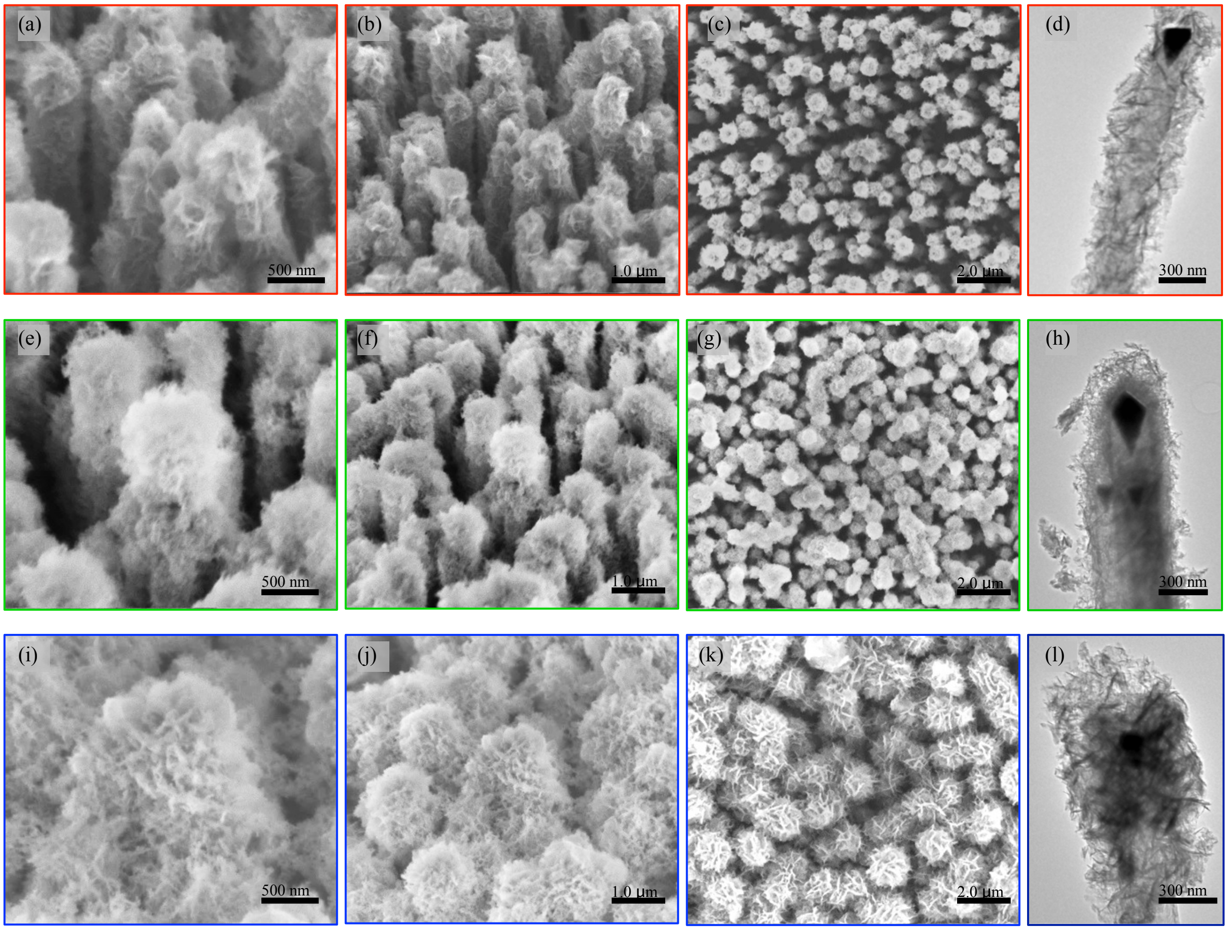

Figure 7.3 – SEM and TEM of the MnOx-coated VACNFs after oxidation and cycling characterizations of MnOx material. Images shown in respect to their nominal thickness of (a-d) 100 nm, (e-h) 300nm, or (i-l) 600 nm. Scale bars are 500 nm, 1 µm, 2 µm, 300 nm; respectively for each nominal thickness.

The Mn-coated VACNF electrodes were then oxidized in galvanostatic mode by applying a current density of 127 μA cm^{-2} (177 μA total) starting at an open circuit potential (OCP) of about -1.3 V. The electropotential was monitored with chronopotentiometry until reaching the upper limit at +0.9 V. The oxidized Mn shell appeared billowy for the entire lot, with very intricate dendrites that resembled rose petals indiscriminately arranged on the VACNF sidewall (Figures 7.1d, 7.1f, and Figure 7.3). Such Mn oxide shells are highly porous, with very thin walls (~20 nm) extending out radially from the CNF core, forming a large expanded shell with cavernous pores across the whole Mn oxide layer. The 100 nm nominal coating showed a coarser structure, with large thick petals (Figures 7.3a-d), while the 600 nm coatings are more ornate with thinner and more convoluted petals (Figure 7.3i-l). The high porosity of the MnO_2 shell is expect to significantly improve the power density since ions can access to the whole MnO_2 film faster through diffusion in electrolyte solution and only need to transport < 10 nm across the solid MnO_2 material from either side of the petal plane.

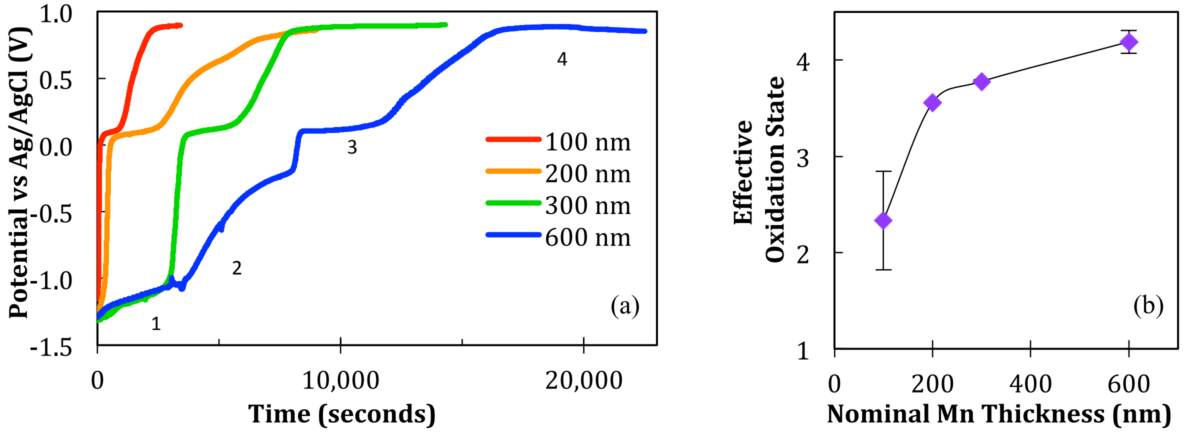

Figure 7.4 – (a) Chronopotentiometric oxidation profiles of Mn-coated VACNF electrodes with nominal thickness of 100, 200, 300, and 600 nm, respectively. The oxidation current is fixed at 127 μA cm^{-2} with an upper limit of +0.9 V. (b) The average effective oxidation state calculated from the profile of chronopotentiometric oxidation of Mn to MnO_2.

Since the 1.0 M Na_2SO_4 electrolyte used for oxidation has a measured pH of 9.4 (unbuffered), the Pourbaix diagram for Mnsuggests oxidation occurs along the following pathway:[172]

$$Mn(s) \xrightarrow{1} Mn(OH)_2 \xrightarrow{2} Mn_3O_4 \xrightarrow{3} Mn_2O_3 \xrightarrow{4} MnO_2 \tag{7.4}$$

The average valence states of Mn in the above five species are 0, 2, 2.67, 3, and 4, respectively. Accordingly, four reaction steps were clearly observed in the chronopotentiometric oxidation profiles as shown in Figure 7.4a. The plateaus at characteristic potentials represent the transition of Mn from one predominant valence state to the next, with the potentials defined by the boundaries between ion species on the Pourbaix diagram at the electrolyte's pH.[67, 172, 173]

For example, the 600 nm sample starts with an OCP of -1.3 V. The potential rises to -1.0 V as Mn(s) is gradually oxidized to $Mn(OH)_2$, and then rises gradually up to 0.0 V representing the formation of Mn_3O_4, and to +0.1 V accompanying the transition from Mn_3O_4 to Mn_2O_3. The strongest oxidation features are the transition from Mn_2O_3 to the final form of MnO_2 at +0.9 V. The time at each step represents the charge involved in the reaction. Interestingly, the thinner Mn coatings with 100 nm and 200 nm nominal thicknesses show smaller oxidation time in the first and second steps compared to that required to complete oxidation into MnO_2. Since the Mn coating on the VACNF is much thinner (~40 nm and ~80 nm, respectively) than the nominal thickness and has a greater surface area to mass ratio than thicker coatings, it is suspected that a significant portion of the Mn atoms have been partially oxidized to MnO or Mn_3O_4 due to exposure to air and the electrolyte before the electrochemical oxidation process. To confirm this, an effective oxidation state (EOS, n_{Mn}) was calculated from each chronopotentiometric profile using the following equation:

$$n_{Mn} = \frac{i\,t}{(m/M)\,F} \tag{7.5}$$

where i is the applied current, t is the time required to complete the oxidation, M is the molar mass of Mn, m is the mass of involved Mn material, and F = 96,500 C mol^{-1} is the Faraday constant. The average EOS of the samples at four different nominal thicknesses is shown in Figure 7.4b. The curve shows an increasing trend toward a higher oxidation state from 2.3 to 3.6 to 3.8 to 4.2 as the nominal Mn thickness increases from 100 nm to 200 nm, 300 nm, and 600 nm, respectively, consistent with the expectation that thinner Mn coating has higher volume percentage being oxidized in the open air. The EOS of the 600 nm nominal Mn thickness is larger than 4 due to some side reactions (such as water electrolysis) between +0.8 to +0.9 V (as shown in CV in Figure 7.6a in later discussion). Thus we have set the upper potential limit at +0.8 V in later supercapacitor tests. These results indicate that even the Mn in the thick coating (at 600 nm nominal thickness) on the VACNF can be completely oxidized into MnO_2, the desired form for optimum supercapacitor performance. The 600 nm nominal thickness is much greater than those that can be applied as thin films on flat surfaces.[72, 73]

Further comparison between SEM images of Figures 7.2 and 7.3 show that the expansion of the Mn shell after electrochemical oxidation is smaller than expected. As shown in a control test utilizing a 100 nm thick Mn film sputtered onto a flat Cr-coated Si wafer, the Mn film thickness expanded by >100% after electrochemical oxidation to form the porous rose-petal-like structure, consistent with the previous report for larger film thicknesses.[73] Besides the large volume expansion, up to 0.10 mg of Mn may dissolute into the 6.0 mL of electrolyte, based on the calculation with $K_{sp} = 1.9 \times 10^{-13}$ for $Mn(OH)_2$ and pH of 9.4:

$$[Mn^{2+}] = 1.9x10^{-13} / [OH^{-}]^2 = 1.9x10^{-13} / (2.51x10^{-5})^2 = 0.30 \text{ mM} \rightarrow 0.0989 \text{ mg} \qquad (7.6)$$

in the form of Mn^{2+}, during the early electrochemical oxidation process, it then formed the species at other valence states with much lower solubility, evident by the electrolyte turning a brownish color. The Mn mass loss during oxidation process is significant for 100 nm nominal Mn thickness (to a maximum of ~63%), but is much less important as the film thickness is increased, dropping to a maximum value of ~10% for 600 nm nominal Mn thickness. It needs to be noted that the exact mass loss of Mn during oxidation varied for each sample, limited by many uncontrolled factors such as sample storage time in the air after Mn deposition, humidity, and oxidation current density. To make the calculations consistent, we neglect the mass loss and used the total starting Mn mass (and subsequent MnO_2 mass) for all samples in later energy storage calculations. As a result, the performance in terms of specific energy and specific power may be under-estimated, particularly for samples with smaller nominal thickness.

7.3.2 XPS Surface Analysis of MnO_2-VACNF Electrode

The MnO_2-coated VACNF electrodes at different nominal Mn thicknesses were characterized by XPS to determine the actual valence state of the Mn after long charge-discharge cycles. The electrodes were polarized to 0.0 V before the potential control was turned off so that the MnO_2 was in the reduced form. The cell was then quickly dissembled and the electrodes were rinsed with deionized water (See Section 7.3).

Table 7.1 – Summary of the Mn 3s XPS Features

Sample	Mn 3s Spectra Values		
(Nominal)	E_B(main)/eV	E_B(sat)/eV	ΔE_B/eV
100 nm MnO_x	83.57	88.80	5.23
300 nm MnO_x	83.54	88.86	5.32
600 nm MnO_x	84.00	88.64	4.64

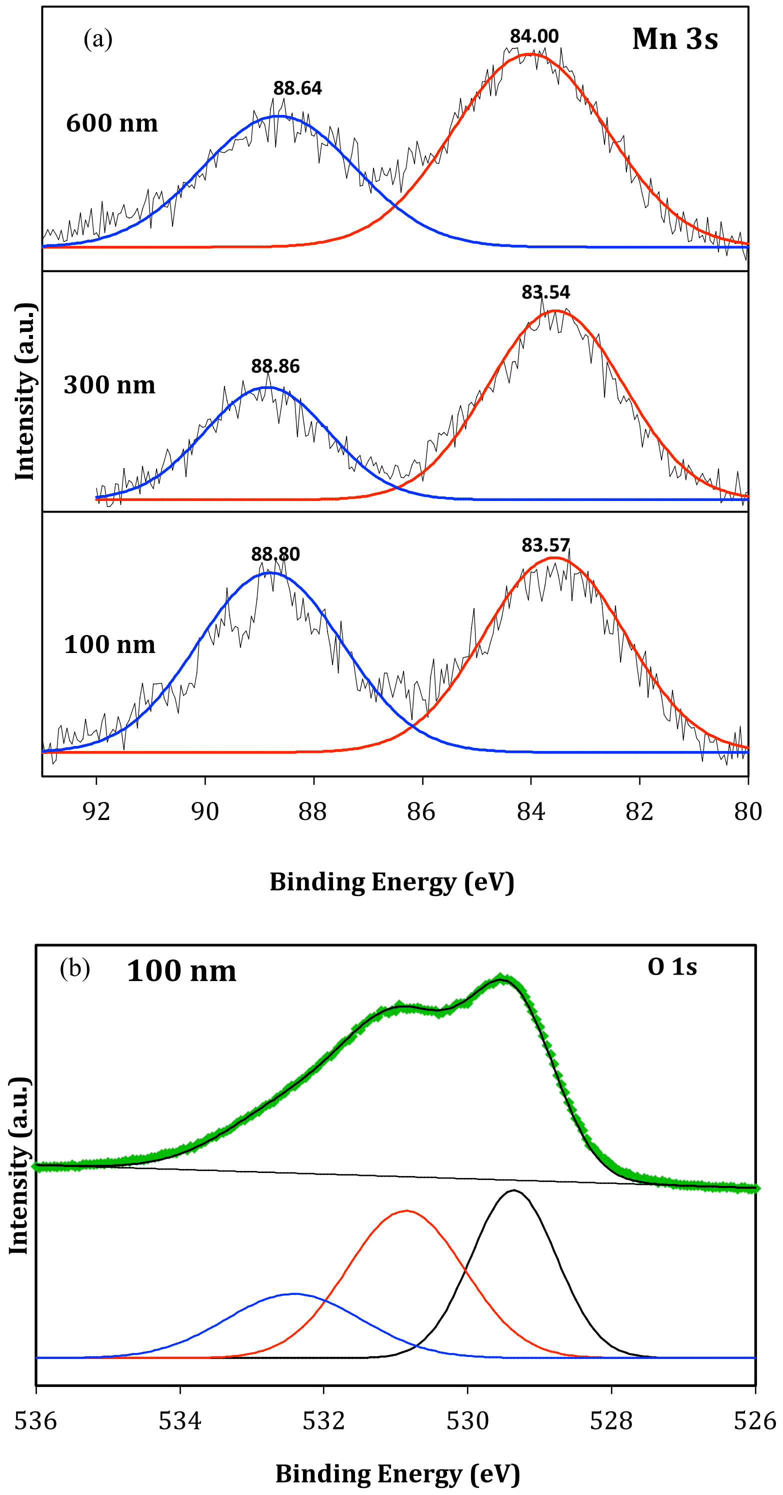

Figure 7.5 – (a) Mn 3s core level XPS spectra for 100, 300 and 600 nm MnO_2-coated VACNF electrodes. The peak position values are indicated. The raw data is represented by black line, and the fitted data are represented by blue and red lines. (b) A typical O 1s spectra (green diamonds) along with fittings for H-O-H (blue), Mn-OH (red), and Mn-O-Mn (black) bindings for 100 nm MnO_2-coated VACNF electrode.

The survey spectra for all the electrode samples show Mn 2p (~642 eV), Mn 3s (~83-89 eV) and O 1s (529-533 eV) peaks attributed to manganese oxides. The Mn 3s core level spectra splits into a doublet due to the parallel spin coupling of the 3s electron with the 3d electron during the photoelectron ejection.[76] The separation in the binding energy between these two peaks is related to the mean Mn oxidation state, as described previously.[174, 175] As shown in Figure 7.5a and Table 7.1, the splitting of the Mn 3s peak is almost the same for 100 nm and 300 nm samples (at 5.23 and 5.32 eV, respectively), indicating that the Mn valence state is about 3 according to literature.[76] In contrast, the splitting of the Mn 3s peak of the 600 nm sample is 4.64 eV, indicating that the valence state of Mn in this electrode is close to 4.[76] Since XPS only provides the information of a very thin layer (<5 nm) at the outer surface, it is likely that the valence state of Mn in deeper layer of this electrode is different. The O 1s spectra provide further information of Mn-O bonds and hydration contents. Figure 7.5b shows a representative O 1s spectrum of the 100 nm sample, which can be de-convoluted into three types of bonds: Mn-O-Mn (529.4 eV), Mn-O-H (530.9 eV) and H-O-H (532.3 eV). The peak areas of Mn-O-Mn and Mn-OH are very similar (at 40% and 38%, respectively), suggesting that nearly all Mn atoms at the surface formed MnOOH bonds during the reduction reaction described by Eq. 1. The third peak accounts for 22% of oxygen due to the adsorption of water. The Mn 3s and O 1s spectra of the 100 nm MnO_2/VACNF sample agree well with each other. But for thicker MnO_2-coated samples, the large adsorption of water and $NaSO_4$ salt in the mesoporous MnO_2 layer caused large uncertainties in the quantitative analysis of O 1s spectra.

7.3.3 Electrochemical Performance of MnO_2-VACNF Electrodes

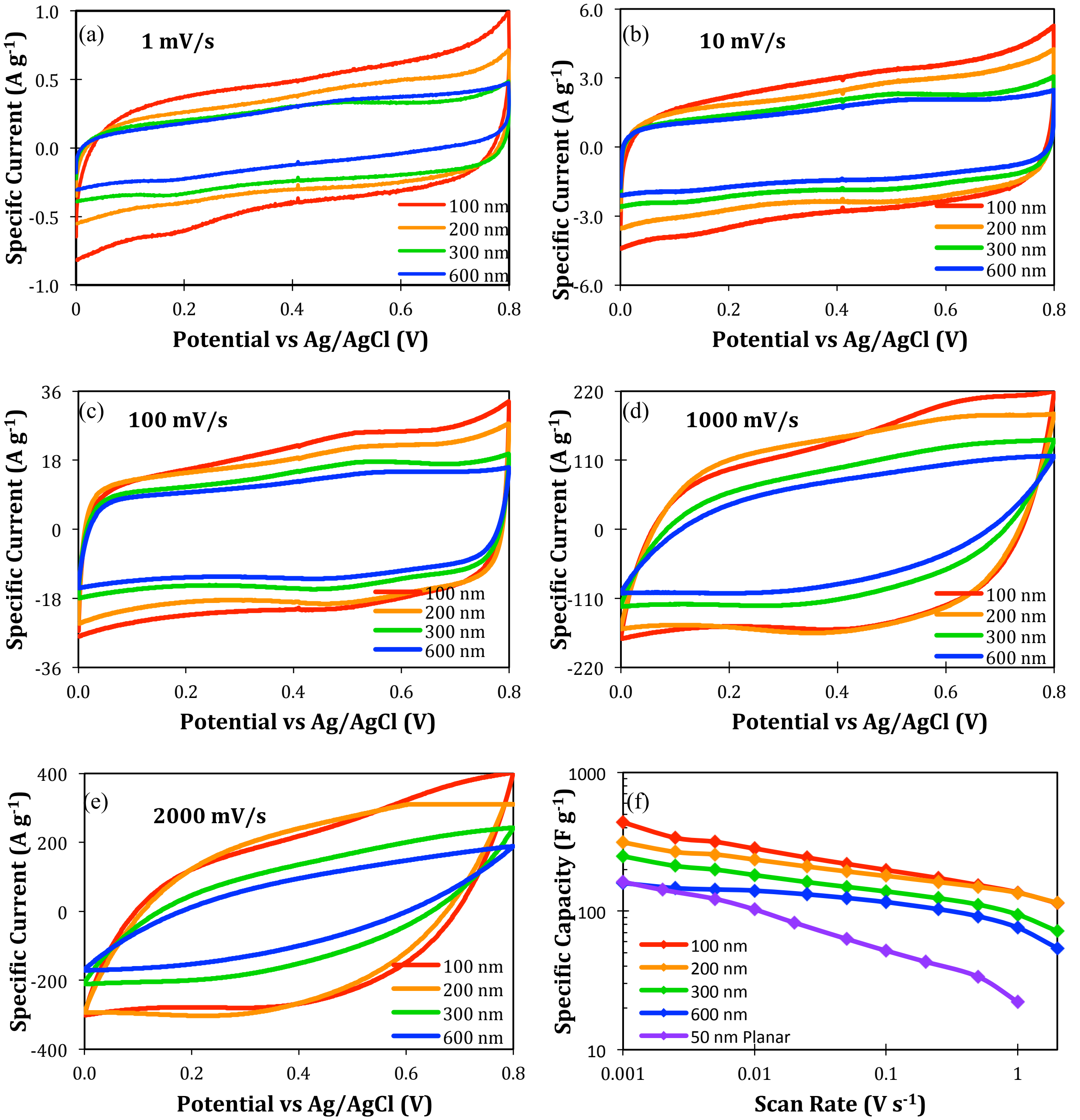

Figure 7.6 – I-V curves by cyclic voltammetry for Mn-coated VACNF electrodes with nominal thickness of 100, 200, 300, and 600 nm, (a-e) performed at the labeled scan rate of 1.0 mV/s to 2000 mV/s. (f) The specific capacity versus the scan rate for various nominal thicknesses. The curve labeled as "50 nm Planar" is measured with a control sample of 50 nm thick planar Mn film deposited on a flat Cr-coated Si wafer.

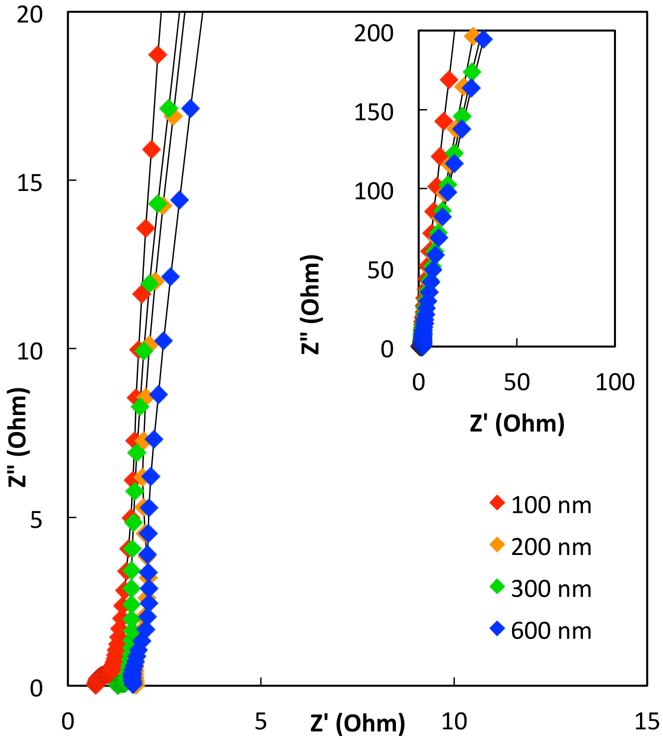

Figure 7.7 – Nyquist plot of electrochemical impedance spectra of the MnO_2-coated VACNFs. The inset shows the full spectra.

After the oxidation step, the electrolyte was replaced with fresh solution and cyclic voltammetry was performed from 0.0 V to 0.8 V at the scan rate varying from 1 mV s^{-1} to 2000 mV s^{-1}. Figures 7.6a-7.6e show the I-V curves of the four samples at five scan rates of 1, 10, 100, 1000, and 2000 mV s^{-1}, respectively. All four samples exhibit good capacitor behavior in a wide range up to 2000 mV s^{-1}, with a symmetrical rectangular loop and a small time constant (represented by the small rounding corners as the polarity is reversed). The MnO_2 redox peak is not observed distinctly, implying that electrodes show faradic pseudocapacitive nature and fast, reversible successive surface redox reactions define the behavior of the voltammogram.[151] This is also supported by EIS, showing steep rise in the imaginary axis and very low charge-transfer resistance and negligible serial resistance (< 2 Ohm) (Figure 7.7); a significant improvement over previous work completed by our group, in part due to the use of a Ti substrate in lieu of the thin Cr film coated Si wafer.[92] In general, the SC value monotonically decreases as the nominal

Mn thickness is increased (Figure 7.6c). At 1 mV s^{-1} scan rate, the 600 nm sample provided 162 F g^{-1}, while the 100 nm sample sailed to a notable 437 F g^{-1}. Increasing the scan rate up to 1000 mV s^{-1} only caused the SC value to descend to 76 F g^{-1} and 135 F g^{-1}, respectively. Pushing the scan rate further to 2000 mV s^{-1} caused the SC to fall more quickly, but still able to deliver 54 F g^{-1} and 109 F g^{-1}, respectively. Although the capacitance of the MnO_2-coated VACNFs seems to follow a logarithmic trend with increasing scan rate (Figure 7.6f), it is noteworthy that such large SC values at a scan rate of 2000 mV s^{-1} (corresponding to 2.5 Hz) is rarely reported for supercapacitors in the literature. In comparison, the control experiment with a planar 50 nm thick Mn film on Cr-coated Si wafer only matches the SC value of the worst sample (600 nm nominal thickness) of all Mn-coated VACNFs at 1.0 mV s^{-1}, but decreased more significantly to 22.1 F g^{-1} at 1000 mV s^{-1} (Figure 7.6f). This result illustrated that the nanoscale architecture provided by the VACNFs is indeed critical to the better performance.

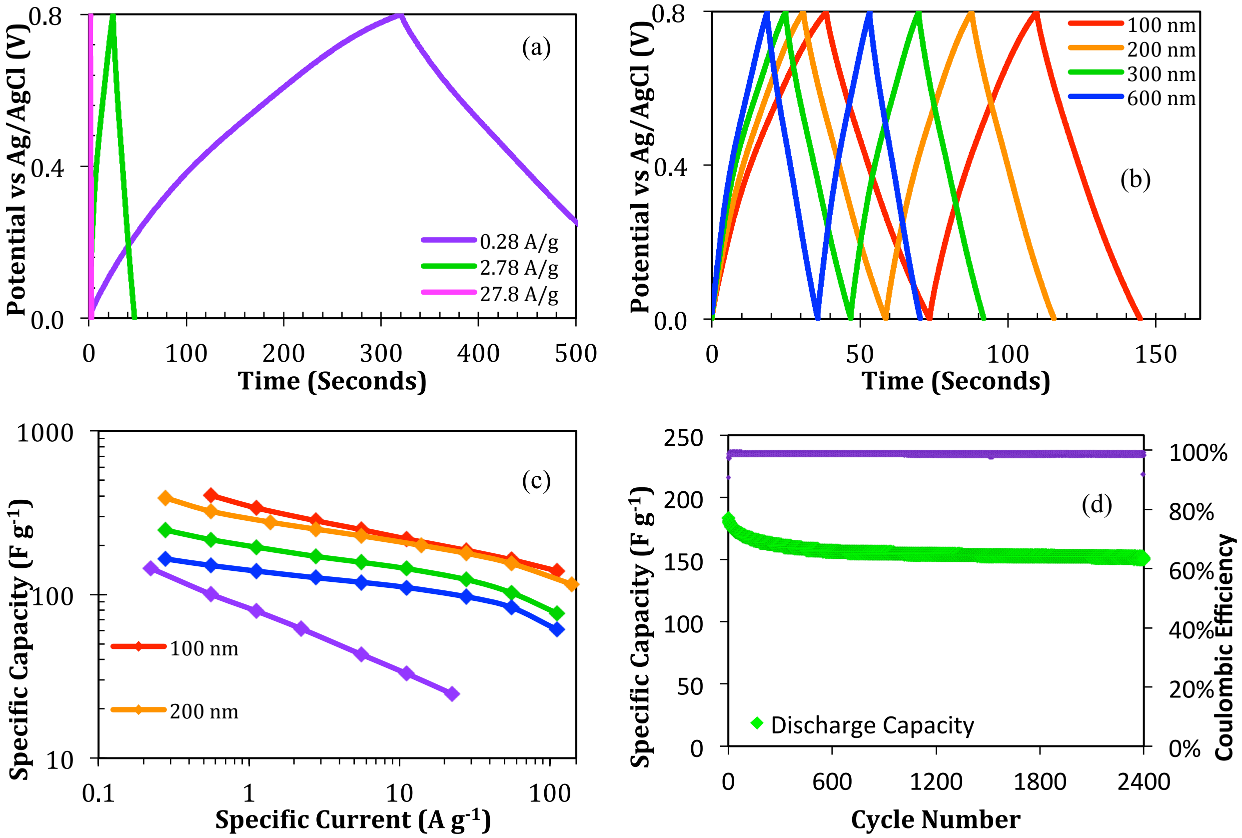

Figure 7.8 – Chronopotentiometric cycling profiles of Mn-coated VACNF electrode with (a) 300 nm nominal thickness at 0.28 A g^{-1}, 2.78 A g^{-1}, and 27.8 A g^{-1} and (b) comparison of varied nominal thickness of 100, 200, 300, and 600 nm at 2.78 A g^{-1}. (c) Specific capacitance versus specific current rate for various nominal thicknesses. (d) Cycling performance of 300 nm nominal thickness at 10 A g^{-1} for 2,400 cycles, showing discharge capacity (green line) and Coulombic efficiency (purple line) versus the cycle number.

The charge-discharge capability at high current densities is one of the most important factors in the development of new electrodes for supercapacitors. Following cyclic voltammetry, a series of chronopotentiometric measurements were performed at a current density of 0.28 A g^{-1} to 140 A g^{-1}. Figure 7.8a shows the rate capability of the electrode with 300 nm nominal thickness, at 0.28, 2.78, and 28.7 A g^{-1}, respectively. The nearly linear and symmetric feature of the voltage profiles suggests good capacitor behavior of the MnO_2-coated VACNF arrays. The corresponding SC values can be calculated as 246, 171, and 97 A g^{-1} by SC = (i_c x t)/ΔV where i_c is the charge (or discharge current density), t the charge (or discharge time), and ΔV the potential window. The SC value only dropped by about a factor of 2.5 as the current density was raised by 100 times, indicating the high reaction rate which matches the high current density.

Figure 7.8b shows the charge-discharge curves at 2.78 A g^{-1} for the four samples with 100, 200, 300, and 600 nm nominal Mn thickness. Similar to the CV measurements, the SC value gradually decreases as the thickness of MnO_2 is increased, achieving a capacitance of 250 F g^{-1} for the 100 nm nominal electrode, decreasing to 127 F g^{-1} for the 600 nm nominal electrode. This reveals that while mass loading increases, the thicker MnO_2 shell was not fully utilized. However, even the sample with 600 nm nominal Mn thickness was able to achieve a SC of 61 F g^{-1} at an extremely large current of ~110 A g^{-1} (Figure 7.8c). This property well exceeds the performance of the much thinner 50 nm planar Mn film on Cr-coated Si wafer, i.e. 144.3 F g^{-1} at 0.22 A g^{-1} and 25 F g^{-1} at 22 A g^{-1}. The MnO_2-coated VACNFs at lower nominal Mn thicknesses consistently show higher SC values that drop slower at high current densities. In addition, a fresh electrode with 300 nm nominal Mn thickness was tested at 10 A g^{-1} for over 2400 cycles (Figure 7.8d). Besides the small initial decay, the SC value of this electrode becomes extremely stable after 800 cycles, maintaining a SC of 152 F g^{-1} after 2000 cycles. The columbic efficiency over the course is over 98.5%.

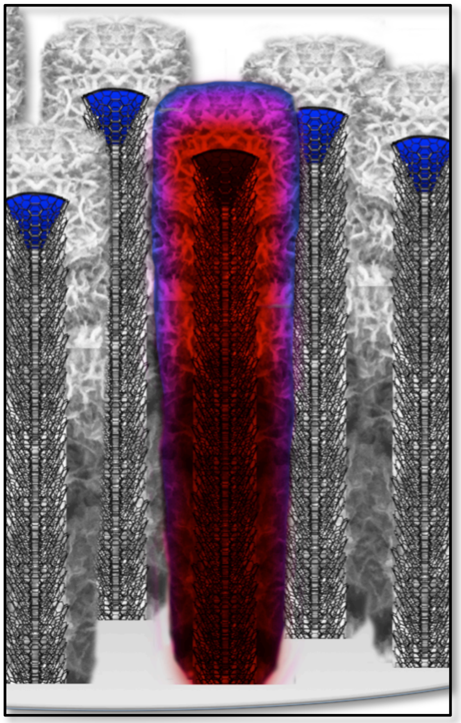

Figure 7.9 – Schematic illustration of the variation in electrochemical activity in MnO_2-coated VACNFs. The inner portion is highly active (red) while the outer portion is less active (blue) due to the low electrical conductivity of MnO_2.

From above results, it is clear that, by spreading Mn along the VACNFs as a thin shell, 12 fold of Mn (i.e. 600 nm vs. 50 nm nominal thickness) can be used while achieving better performance than that on a flat surface. This significantly increases the Mn mass loading and the total energy storage capacity. As we discussed in the introduction, the maximum thickness of MnO_2 films, either planar film on flat surface or coaxial shell wrapping around VACNFs, is determined by both electron and ion transport properties. The high porosity of the rose-petal-like MnO_2 nanostructure formed by electrochemical oxidation in this study allows cations to easily access the entire MnO_2 material through much faster diffusion in solution than across the solid MnO_2 film. As a result, the usable radial thickness of MnO_2 shell can be expanded to over 200 nm (see Figure 7.3l) from the 7.5 nm compact shell in our previous study which was ion transport limited.[92] However, the low electrical conductivity of MnO_2 may now be a limiting factor, particularly in thicker shells. As illustrated in Figure 7.9, the outer portion of a thick MnO_2 shell may lose effective electrical connection with the CNF core and thus is not fully engaged in charge-discharge processes even though there are much more ions available in the outer portion for insertion reactions. This factor is responsible for the lower SC value as the nominal Mn thickness is increased. For the same reason, the XPS data in Figure 7.5a showed that the MnO_2 at the outer surface of the samples started with 100 and 300 nm nominal Mn thickness was reduced to valence state +3 at the last discharge cycle, while that of the 600-nm sample remained at +4. The inner portion of the MnO_2 shell (represented by the red color in Figure 7.9) has much better electrical connection to the CNF core and serves as the most active redox materials during charge and discharge. Overall, this hybrid core-shell structure is expected to enhance both energy capacity and power rate of the MnO_2 supercapacitor.

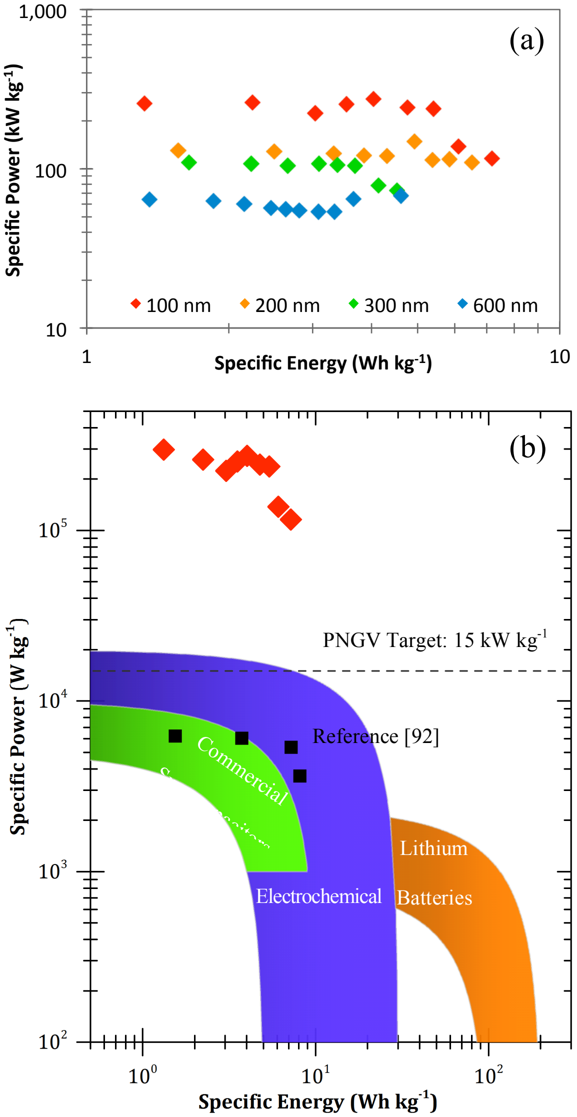

Figure 7.10 – Ragone plots of Mn-coated VACNF electrodes (a) at the nominal Mn thicknesses of 100, 200, 300, and 600 nm; and (b) at 100 nm nominal Mn thickness (◆) with comparisons to values achieved in previous work[92](■), and the range seen for commercial & state-of-art supercapacitors as well as lithium batteries[176]. The black dashed line represents a target in specific power proposed by Partnership for a New Generation of Vehicles (PNGV).[177]

To illustrate the potential of these 3D architectured hybrid electrodes for electrical energy storage, the specific energy (Wh kg^{-1}) and specific power (W kg^{-1}) of a full cell have been derived from the above half-cell results and plotted in the Ragone plot (Figure 7.10). For a single supercapacitor electrode, the maximum stored energy is related to the total charge (Q) built up on the electrode in a linear fashion up to the maximum voltage (V), with:

$$C_0 = \frac{Q}{Vm} \tag{7.7}$$

$$\mathrm{E_0} = (1/2)\mathrm{C_0V^2} \tag{7.8}$$

However, for a full cell consisting of two identical electrodes, the specific energy is represented by the following:

$$E_{0,full\ cell} = (1/8)\mathrm{C_0V^2} \tag{7.9}$$

The specific power P_0 of a supercapacitor represents the maximum power output, which can be calculated by

$$P_0 = \frac{\mathrm{V^2}}{4\ \mathrm{m\ ESR}} \tag{7.10}$$

where *m* is the total mass of MnO_2 on both electrodes ESR is the equivalent series resistance that is determined by the voltage drop after the current polarity is flipped during charge-discharge processes.

Interestingly, as the current density was varied by 100 fold, from ~0.28 A g^{-1} to ~28 A g^{-1} in galvanostatic charge-discharge, the specific power *P* remained nearly constant, indicating that the change in ESR is negligible in this wide current ranges (Figure 7a). This is quite different from common supercapacitors. As shown in Figure 7b, while the specific energy in this study is between 1 to 10 Wh kg^{-1}, comparable to commercial supercapacitors[176] and compact MnO_2 shells on VACNFs in our own previous study[92], the specific power is more than one order of magnitude higher than the other studies (Figure 7b), reaching 240 kW kg^{-1} for the 100 nm nominal thickness and over 70 kW kg^{-1} for the 600 nm nominal thickness. This greatly surpasses the target in specific power of 15 kW kg^{-1} (but including the whole system), proposed by the Partnership for a New Generation of Vehicles (PNGV).[177, 178] The high-power capability can be attributed to the improvement in ion diffusion through the electrolyte penetrating into mesoporous MnO_2 shell in the hybrid structure. The specific energy, however, is limited by the low electrical conductivity that prevents effective electrical connection to the outer shells. Improving Mn coating to spread it more uniformly along the VACNFs and incorporating an additional conductive polymer (or carbon) coating at electrolyte/MnO_2 interface may enhance the specific energy in future studies.

7.4 Conclusion

We have demonstrated the formation of rose-petal-like mesoporous MnO_2 layers by electrochemical oxidization of Mn shells of 100 to 600 nm nominal thickness sputter-coated on vertically aligned carbon nanofibers (VACNFs). Such 3D MnO_2/VACNF hybrid architecture provides enhanced ion diffusion across the mesoporous MnO_2 shell and yields excellent current collecting capability using the conductive VACNF core, both required for high-performance supercapacitors. The enhanced ion diffusion lift the previous limit of optimum MnO_2 shell thickness at ~7.5 nm while the high electron and ion transport collectively enabled the fast redox reaction in thick MnO_2 shells up to 200 nm during charge-discharge processes in 1 M Na_2SO_4 electrolyte. More than one order of magnitude higher specific power (~240 kW kg^{-1}) was obtained with such a hybrid electrode material as compared to the state-of-the-art supercapacitors based on other MnO_2 structures at the similar specific energy range (~1 to 10 Wh kg^{-1}). This design strategy clearly demonstrates the remarkable capability of using VACNFs core structure as a template for high-powered energy storage devices.

Chapter 8 - Concluding Remarks

Nanostructured materials will continue to play a pivotal role in improving the capacity and performance of electrical energy storage systems, as both existing and emerging applications demand it. The ability of the vertically aligned carbon nanofibers to enhance kinetics and electrochemical activity is shown through the improved current rates and overall capacity, which are desirable for broader applications with constrictive requirements. This dissertation described several uses of the VACNF array and shows how each benefited from a nearly perfect platform for depositing onto, activating, and fully utilizing the electrode material.

The first project introduced the use of Si-coated VACNF arrays as anode for lithium ion batteries (LIBs). The goal was to capitalize on the massive specific capacity of Si while reducing issues of degradation and detachment seen earlier in bulk electrodes. The VACNF, with the stack of broken graphitic edges on each CNF bind the Si to the surface, while the open vertical structure allowed the shells to expand and contract freely, releasing internal stress and strain during lithiation. The geometry also removed the stress at the Si/CNF interface, which otherwise lead to disconnection and immediate capacity loss. The robustness of the coated VACNFs was shown by the ability for the Si to reach the full capacity in every cycle over many hundreds of cycles. Remarkable high-rate retention was shown in the second study and was owed to the unique pine-leave nanocolumnar structure of the Si-shell on VACNFs produced by a combination of magnetron sputtering and the wealth of broken graphitic edges on each CNF that acted as nucleation sites for the deposited material. Surprisingly, the measured capacity showed a slight increase at the higher rates, a phenomenon that had never been reported in literature, but is desired for higher-power performance lithium-ion batteries.

Expanding on the success of the Si coating, TiO_2 was also investigated as a shell material due to its high-rate Li storage kinetics by means of Li^+ insertion coupled with pseudocapacitive reactions. Again, the robustness of the TiO_2 shell material was displayed by minimal capacity fading over thousands of cycles, while the coated VACNFs were cycled at rates from 1.5C up to 150C+. Thus it was shown that the VACNF helped to improve the performance by providing better conductivity to more of the loaded TiO_2 material.

This led to the ultimate goal of placing two coated VACNF electrodes in opposed positions to create a unique LIB that enhanced not only high-rate performance, but also demonstrated battery-supercapacitor characteristics at high C-rates. The true hybrid nature of this full cell was realized in accommodating both high capacities at lower and high current rates without loss of integrity. By bringing together these two nanostructured electrodes, the full-cell demonstrated a true high power Li-ion battery that is comparable to conventional supercapacitors.

As an ultimate test of high rate performance, the VACNF was used to support Mn shells, which were electrochemically oxidized to form rose-petal-like mesoporous MnO_2 layers for use as a supercapacitor. The structures showed enhanced ion diffusion across the porous MnO_2 shell and yielded excellent current collecting capability using the conductive VACNF as core, both required for high-performance cycling. More than an order of magnitude higher specific power was obtained as compared to the state-of-the-art supercapacitors at the similar specific energy range.

These architectures are unique to our work, where the remarkable capability clearly demonstrates the strategy of using VACNFs core structure as a template for high-powered, high-energy storage devices. For the best perspective as to were the performance of the Si-TiO_2

hybrid battery-supercapacitor and the MnO_2-coated VACNFs supercapacitor stand, we return to the Ragone plot.[12, 16] Figure 8.1 shows both of the systems documented in this dissertation demonstrating state-of-the-art capabilities by delivering maximum specific energy at specific power rates unmatched by other devices. This goes to show how valuable the VACNF array can be to next generation electrodes, delivering the needed energy at high rate with trusted reliability that is unparalleled in the literature today. Plus, there are more materials that can benefit from this great core-shell architecture as well.

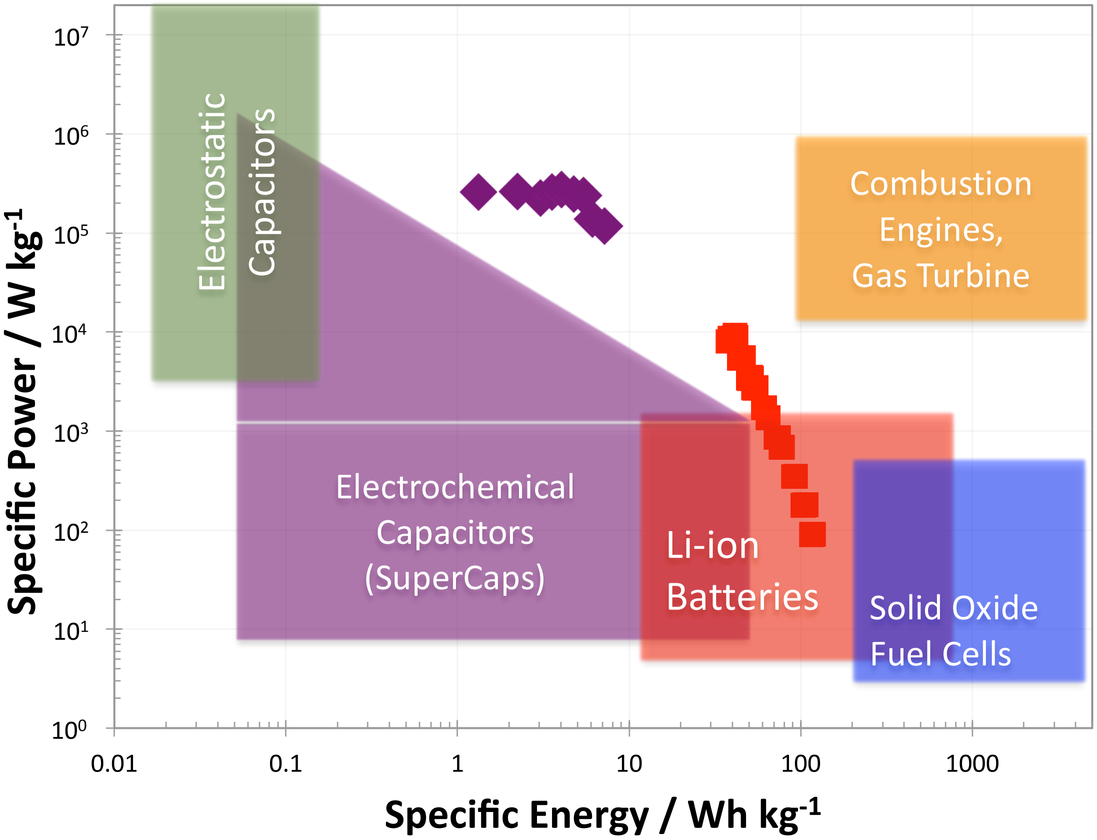

Figure 8.1 - Ragone plot of various electrochemical energy storage systems, with addition of (◆) MnO_2 pseudocapacitor and (■) Si-TiO_2 hybrid battery technologies. Adapted by permission from M. Winter and R. J. Brodd, *Chemical Reviews*, 2004, 104, 4245-4270. Copyright 2004, American Chemical Society.

8.1 Future Direction

The field of electrical energy storage systems is very much alive and full of excitement, as it races to revolutionize many key industries in an effort to be more sustainable. The findings shown here are just the tip of a larger body of work needed to make the coated VACNF electrodes more useful in the commercial setting. The limited mass loading of the coated VACNF arrays has been questioned several times, and is highlighted in Chapter 3. Although the Si-coated VACNF showed less than 1 mg cm^{-2} of deposited materials onto the electrode surface, (less than today's commercially casted film electrodes) the trading of high-rate performance for greater areal capacity is an avenue for other study. In the mean time, several companies have vying to get a Si-based anode to market, with them now looking toward our industry collaborator, Catalyst Power Technologies, as a good performer. Showing that the VACNF array is practical for nearly any material, Qing and coworkers have tried other anode materials, [26, 86-89, 179-182] showing continued success of the VACNF nanostructure to improving capacity and rate performance.

Cathode materials have the most to gain with use of the VACNFs as intrinsic crystal structure changes still limit the rate performance and cycling lifetime.[183] Through better control of the particle size deposited on the VACNF, performances for most transition metal oxides; such as $LiNiO_2$, $LiMn_2O_4$, $LiFePO_4$, and several others, should see a good improvement. More aggressive research is needed to search for new materials, as high throughput theoretical calculations are already helping to narrow down new candidates of cathode materials, and provide insights into how nanostructures can be utilized to attain theoretical capacities at high rates.[49, 184, 185]

Cathode materials that have an even wider operating voltage window will need a more suitable current collector, which can tolerate the high oxidation potential of the cathode. Commercially, aluminum is used for cathode support, but is incompatible to our current PECVD processing protocol due to it low melting point. Graphite paper has shown promise, but further characterization and corrosion analysis will be needed.

Overall, optimization of each material coating with regards to thickness, crystal size, deposition condition, was not the primary focus of this dissertation work, but would be required to improve specific energy and power toward even greater level. But clearly, the assembly of hybrid structures using the well-defined VACNF array template is a viable approach for energy storage technologies and would allow for higher power rate and higher specific capacity storage for the most demanding applications.

References

1. N. E. I. C. (NEIC), Greenhouse Gases, Climate Change, and Energy, http://www.eia.gov/oiaf/1605/ggccebro/chapter1.html, Accessed March 12, 2015, 2015.

2. D. P. Tans, Trends in Atmospheric Carbon Dioxide, http://www.esrl.noaa.gov/gmd/ccgg/trends/, Accessed January 28, 2015, 2015.

3. A. Luntz, *J. Phys. Chem. Lett.*, 2015, 6, 300-301.

4. S. Kann, M. Shiao, C. Honeyman, N. Litvak, J. Jones and L. Cooper, *US solar market insight report: 2015 year-in-review-Executive summary*, 2015.

5. D. R. Dunn, J. Barrick, A. Sweeney, N. Davis, S. Thapa, R. S. Hankey, S. Kaplan, P. Smith and P. Lindstrom, ed. U. E. I. Administration, 2015.

6. B. Dunn, H. Kamath and J. M. Tarascon, *Science*, 2011, 334, 928-935.

7. R. Hensley, J. Newman and M. Rogers, *McKinsey Quarterly*, 2012, 3, 5-50.

8. S. J. Gerssen-Gondelach and A. P. C. Faaij, *J. Power Sources*, 2012, 212, 111-129.

9. A. J. Bard and L. R. Faulkner, *Electrochemical methods: fundamentals and applications*, Wiley New York, 1980.

10. M. Winter and R. J. Brodd, *Chem. Rev.*, 2004, 104, 4245-4270.

11. W. Lu and L. Dai, *Carbon nanotube supercapacitors*, INTECH Open Access Publisher, 2010.

12. D. V. Ragone, *Review of battery systems for electrically powered vehicles*, SAE Technical Paper, 1968.

13. B. E. Conway, *Electrochemical supercapacitors: scientific fundamentals and technological applications*, Kluwer Academic/Plenum: New York, 1999.

14. B. Dibner, *Alessandro Volta and the electric battery*, Franklin Watts, 1964.

15. M. Yoshio, R. J. Brodd and A. Kozawa, *Lithium-Ion Batteries*, Springer, 2009.

16. T. Christen and M. W. Carlen, *J. Power Sources*, 2000, 91, 210-216.

17. M. S. Whittingham, *Science*, 1976, 192, 1126-1127.

18. B. Kumar and J. Kumar, *J. Electrochem. Soc.*, 2010, 157, A611.

19. D. Aurbach, E. Zinigrad, Y. Cohen and H. Teller, *Solid State Ionics*, 2002, 148, 405-416.

20. T. R. Jow, K. Xu, O. Borodin and M. Ue, *Electrolytes for lithium and lithium-ion batteries*, Springer, 2014.

21. A. S. Arico, P. Bruce, B. Scrosati, J. M. Tarascon and W. van Schalkwijk, *Nat. Mater.*, 2005, 4, 366-377.

22. W. J. Zhang, *J. Power Sources*, 2011, 196, 13-24.

23. A. Magasinski, P. Dixon, B. Hertzberg, A. Kvit, J. Ayala and G. Yushin, *Nat. Mater.*, 2010, 9, 353-358.

24. C. K. Chan, H. Peng, G. Liu, K. McIlwrath, X. F. Zhang, R. A. Huggins and Y. Cui, *Nat. Nanotechnol.*, 2008, 3, 31-35.

25. M. H. Park, M. G. Kim, J. Joo, K. Kim, J. Kim, S. Ahn, Y. Cui and J. Cho, *Nano Lett.*, 2009, 9, 3844-3847.

26. L. M. Sun, X. H. Wang, R. A. Susantyoko and Q. Zhang, *Carbon*, 2015, 82, 282-287.

27. C. K. Chan, X. F. Zhang and Y. Cui, *Nano Lett.*, 2008, 8, 307-309.

28. L. P. Tan, Z. Y. Lu, H. T. Tan, J. X. Zhu, X. H. Rui, Q. Y. Yan and H. H. Hng, *J. Power Sources*, 2012, 206, 253-258.

29. T. Kennedy, E. Mullane, H. Geaney, M. Osiak, C. O'Dwyer and K. M. Ryan, *Nano Lett.*, 2014, 14, 716-723.

30. B. A. Boukamp, G. C. Lesh and R. A. Huggins, *J. Electrochem. Soc.*, 1981, 128, 725-729.

31. H. Kim, C.-Y. Chou, J. G. Ekerdt and G. S. Hwang, *J. Phys. Chem. C*, 2011, 115, 2514-2521.

32. M. R. Zamfir, H. T. Nguyen, E. Moyen, Y. H. Lee and D. Pribat, *J. Mater. Chem. A*, 2013, 1, 9566-9586.

33. S. Ohara, J. Suzuki, K. Sekine and T. Takamura, *J. Power Sources*, 2004, 136, 303-306.

34. J. P. Maranchi, A. F. Hepp, A. G. Evans, N. T. Nuhfer and P. N. Kumta, *J. Electrochem. Soc.*, 2006, 153, A1246-A1253.

35. J. P. Maranchi, A. F. Hepp and P. N. Kumta, *Electrochem. Solid St*, 2003, 6, A198-A201.

36. T. S. Arthur, D. J. Bates, N. Cirigliano, D. C. Johnson, P. Malati, J. M. Mosby, E. Perre, M. T. Rawls, A. L. Prieto and B. Dunn, *MRS Bull.*, 2011, 36, 523-531.

37. J. W. Long, B. Dunn, D. R. Rolison and H. S. White, *Chem. Rev.*, 2004, 104, 4463-4492.

38. J. M. Tarascon and M. Armand, *Nature*, 2001, 414, 359-367.

39. J. Molenda and J. Marzec, *Funct. Mater. Lett.*, 2008, 01, 91-95.

40. J. H. Ryu, J. W. Kim, Y. E. Sung and S. M. Oh, *Electrochem Solid St*, 2004, 7, A306-A309.

41. U. Kasavajjula, C. S. Wang and A. J. Appleby, *J. Power Sources*, 2007, 163, 1003-1039.

42. H. Chen, J. Xu, P. C. Chen, X. Fang, J. Qiu, Y. Fu and C. Zhou, *ACS Nano*, 2011, 5, 8383-8390.

43. L. F. Cui, Y. Yang, C. M. Hsu and Y. Cui, *Nano Lett.*, 2009, 9, 3370-3374.

44. P. C. Chen, J. Xu, H. T. Chen and C. W. Zhou, *Nano Research*, 2011, 4, 290-296.

45. W. Wang, R. Epur and P. N. Kumta, *Electrochem. Commun.*, 2011, 13, 429-432.

46. J. Qu, H. Q. Li, J. J. Henry, S. K. Martha, N. J. Dudney, H. B. Xu, M. F. Chi, M. J. Lance, S. M. Mahurin, T. M. Besmann and S. Dai, *J. Power Sources*, 2012, 198, 312-317.

47. D. Choi, W. Wang and Z. Yang, *Material Challenges and Perspectives*, CRC Press, 2011.

48. G. Hautier, A. Jain, S. P. Ong, B. Kang, C. Moore, R. Doe and G. Ceder, *Chem. Mater.*, 2011, 23, 3495-3508.

49. S. Curtarolo, G. L. Hart, M. B. Nardelli, N. Mingo, S. Sanvito and O. Levy, *Nat. Mater.*, 2013, 12, 191-201.

50. M. S. Whittingham, *Chem. Rev.*, 2004, 104, 4271-4301.

51. B. Wang, W. Al Abdulla, D. Wang and X. S. Zhao, *Energ. Environ. Sci.*, 2015, 8, 869-875.

52. G. N. Zhu, Y. G. Wang and Y. Y. Xia, *Energ. Environ. Sci.*, 2012, 5, 6652-6667.

53. X. H. Wang, X. W. Li, X. L. Sun, F. Li, Q. M. Liu, Q. Wang and D. Y. He, *J. Mater. Chem.*, 2011, 21, 3571-3573.

54. F. Y. Cheng, H. B. Wang, Z. Q. Zhu, Y. Wang, T. R. Zhang, Z. L. Tao and J. Chen, *Energ. Environ. Sci.*, 2011, 4, 3668-3675.

55. J. W. Fergus, *J. Power Sources*, 2010, 195, 939-954.

56. V. Augustyn, P. Simon and B. Dunn, *Energ. Environ. Sci.*, 2014, 7, 1597-1614.

57. J. Wang, J. Polleux, J. Lim and B. Dunn, *J. Phys. Chem. C*, 2007, 111, 14925-14931.

58. M. M. Thackeray, *Handbook of Battery Materials*, 1998, DOI: 10.1002/9783527611676.ch13, 293-321.

59. Z. G. Yang, D. Choi, S. Kerisit, K. M. Rosso, D. H. Wang, J. Zhang, G. Graff and J. Liu, *J. Power Sources*, 2009, 192, 588-598.

60. H. Helmholtz, *Annalen der Physik und Chemie*, 1853, 165, 211-233.

61. B. E. Conway, J. O. Bockris and I. A. Ammar, *Transactions of the Faraday Society*, 1951, 47, 756-766.

62. M. Gouy, *Journal de Physique Théorique et Appliquée*, 1910, 9, 457-468.

63. D. L. Chapman, *Philosophical Magazine Series 6*, 1913, 25, 475-481.

64. O. Stern, *Zeit. Elektrochem*, 1924, 30, 508-516.

65. W. Lu, R. Hartman, L. T. Qu and L. M. Dai, *J. Phys. Chem. Lett.*, 2011, 2, 655-660.

66. L. L. Zhang, R. Zhou and X. S. Zhao, *J. Mater. Chem.*, 2010, 20, 5983-5992.

67. M. Lu, F. Beguin and E. Frackowiak, *Supercapacitors: Materials, Systems and Applications*, John Wiley & Sons, 2013.

68. G. Wang, L. Zhang and J. Zhang, *Chem. Soc. Rev.*, 2012, 41, 797-828.

69. C. C. Yu, L. X. Zhang, J. L. Shi, J. J. Zhao, J. H. Gao and D. S. Yan, *Adv. Funct. Mater.*, 2008, 18, 1544-1554.

70. V. Subramanian, H. Zhu, R. Vajtai, P. M. Ajayan and B. Wei, *J. Mater. Chem. B*, 2005, 109, 20207-20214.

71. S. C. Pang, M. A. Anderson and T. W. Chapman, *J. Electrochem. Soc.*, 2000, 147, 444-450.

72. J. N. Broughton and M. J. Brett, *Electrochim. Acta*, 2004, 49, 4439-4446.

73. B. Djurfors, J. N. Broughton, M. J. Brett and D. G. Ivey, *J. Power Sources*, 2006, 156, 741-747.

74. C. C. Hu and C. C. Wang, *J. Electrochem. Soc.*, 2003, 150, A1079-A1084.

75. L. Z. Wang, Y. Omomo, N. Sakai, K. Fukuda, I. Nakai, Y. Ebina, K. Takada, M. Watanabe and T. Sasaki, *Chem. Mater.*, 2003, 15, 2873-2878.

76. M. Toupin, T. Brousse and D. Belanger, *Chem. Mater.*, 2004, 16, 3184-3190.

77. Y. T. Wu and C. C. Hu, *J. Electrochem. Soc.*, 2004, 151, A2060-A2066.

78. V. Subramanian, H. W. Zhu and B. Q. Wei, *Pure Appl. Chem.*, 2008, 80, 2327-2343.

79. Z. F. Ren, Z. P. Huang, J. W. Xu, J. H. Wang, P. Bush, M. P. Siegal and P. N. Provencio, *Science*, 1998, 282, 1105-1107.

80. B. A. Cruden, A. M. Cassell, Q. Ye and M. Meyyappan, *J. Appl. Phys.*, 2003, 94, 4070-4078.

81. A. V. Melechko, V. I. Merkulov, T. E. McKnight, M. A. Guillorn, K. L. Klein, D. H. Lowndes and M. L. Simpson, *J. Appl. Phys.*, 2005, 97.

82. J. Li and G. P. Pandey, *Annu. Rev. Phys. Chem.*, 2015, 66, null.

83. E. C. Landis, K. L. Klein, A. Liao, E. Pop, D. K. Hensley, A. V. Melechko and R. J. Hamers, *Chem. Mater.*, 2010, 22, 2357-2366.

84. Q. Ngo, T. Yamada, M. Suzuki, Y. Ominami, A. M. Cassell, J. Li, M. Meyyappan and C. Y. Yang, *IEEE T. Nanotechnol.*, 2007, 6, 688-695.

85. M. Meyyappan, L. Delzeit, A. Cassell and D. Hash, *Plasma Sources Sci T*, 2003, 12, 205-216.

86. R. A. Susantyoko, X. Wang, L. Sun, K. L. Pey, E. Fitzgerald and Q. Zhang, *Carbon*, 2014, 77, 551-559.

87. R. A. Susantyoko, X. H. Wang, Q. Z. Xiao, E. Fitzgerald and Q. Zhang, *Carbon*, 2014, 68, 619-627.

88. X. Wang, R. A. Susantyoko, Y. Fan, L. Sun, Q. Xiao and Q. Zhang, *Small*, 2014, 10, 2826-2829, 2742.

89. Q. Z. Xiao, Y. Fan, X. H. Wang, R. A. Susantyoko and Q. Zhang, *Energ. Environ. Sci.*, 2014, 7, 655-661.

90. G. A. Malek, E. Brown, S. A. Klankowski, J. Liu, A. J. Elliot, R. Lu, J. Li and J. Wu, *ACS Appl. Mater. Inter.*, 2014, 6, 6865-6871.

91. Y. Zheng, Kansas State University, 2014.

92. J. W. Liu, J. Essner and J. Li, *Chem. Mater.*, 2010, 22, 5022-5030.

93. L. Z. Swisher, L. U. Syed, A. M. Prior, F. R. Madiyar, K. R. Carlson, T. A. Nguyen, D. H. Hua and J. Li, *J. Phys. Chem. C*, 2013, 117, 4268-4277.

94. L. Z. Swisher, A. M. Prior, S. Shishido, T. A. Nguyen, D. H. Hua and J. Li, *Biosens. Bioelectron.*, 2014, 56, 129-136.

95. M. Foram Ranjeet, S. Lateef Uddin, A. Prabhu and L. Jun, in *Advances in Applied Nanotechnology for Agriculture*, American Chemical Society, 2013, vol. 1143, ch. 6, pp. 109-124.

96. F. R. Madiyar, L. U. Syed, C. T. Culbertson and J. Li, *Electrophoresis*, 2013, 34, 1123-1130.

97. F. R. Madiyar, S. Bhana, L. Z. Swisher, C. T. Culbertson, X. Huang and J. Li, *Nanoscale*, 2015, 7, 3726-3736.

98. G. Baysinger, ed., *CRC Handbook of Chemistry and Physics*, National Institute of Standards and Technology, 2015.

99. M. Ohring, *Materials science of thin films*, Academic press, 2001.

100. W. Wang and P. N. Kumta, *ACS Nano*, 2010, 4, 2233-2241.

101. N. Quoc, A. M. Cassell, A. J. Austin, L. Jun, S. Krishnan, M. Meyyappan and C. Y. Yang, *IEEE Electron Device Lett.*, 2006, 27, 221-224.

102. L. U. Syed, J. W. Liu, A. M. Prior, D. H. Hua and J. Li, *Electroanal*, 2011, 23, 1709-1717.

103. E. C. Landis and R. J. Hamers, *J. Mater. Chem. C*, 2008, 112, 16910-16918.

104. D. Aurbach, M. D. Levi, E. Levi and A. Schechter, *J. Phys. Chem. B*, 1997, 101, 2195-2206.

105. D. Aurbach, Y. Talyosef, B. Markovsky, E. Markevich, E. Zinigrad, L. Asraf, J. S. Gnanaraj and H. J. Kim, *Electrochim. Acta*, 2004, 50, 247-254.

106. G. K. Simon and T. Goswami, *Metallurgical and Materials Transactions a-Physical Metallurgy and Materials Science*, 2011, 42A, 231-238.

107. Y. W. Perla B. Balbuena, *Lithium-ion Batteries: Solid-Electrolyte Interphase*, Imperial College Press, River Edge, NJ, 2004.

108. D. R. Lide, ed., *CRC Handbook of Chemistry and Physics*, CRC Press, New York, 2004.

109. M. Winter, K.-C. Moeller and J. O. Besenhard, in *Lithium Batteries: Science and Technology*, eds. G.-A. Nazri and G. Pistoia, Kluwer Academic Publishers, Boston, 2004, ch. 5, pp. 144-194.

110. T. D. Nguyen-Vu, H. Chen, A. M. Cassell, R. Andrews, M. Meyyappan and J. Li, *Small*, 2006, 2, 89-94.

111. W. Wan, Q. Zhang, Y. Cui and E. Wang, *J Phys Condens Matter*, 2010, 22, 415501.

112. J. R. Szczech and S. Jin, *Energ. Environ. Sci.*, 2011, 4, 56-72.

113. V. Etacheri, R. Marom, R. Elazari, G. Salitra and D. Aurbach, *Energ. Environ. Sci.*, 2011, 4, 3243-3262.

114. D. Aurbach, eds. W. Schalkwijk and B. Scrosati, Springer US, 2002, DOI: 10.1007/0-306-47508-1_2, pp. 7-77.

115. I. I. Abdulhalim, R. Beserman and R. Weil, *Phys Rev B Condens Matter*, 1989, 39, 1081-1091.

116. S. A. Klankowski, R. A. Rojeski, B. A. Cruden, J. Liu, J. Wu and J. Li, *J. Mater. Chem. A*, 2013, 1, 1055-1064.

117. J. A. Thornton, *J. Vac. Sci. Technol. A*, 1986, 4, 3059.

118. R. Messier, A. P. Giri and R. A. Roy, *J. Vac. Sci. Technol. A*, 1984, 2, 500-503.

119. I. Petrov, P. B. Barna, L. Hultman and J. E. Greene, *J. Vac. Sci. Technol. A*, 2003, 21, S117-S128.

120. Y. Fan, Q. Zhang, Q. Z. Xiao, X. H. Wang and K. Huang, *Carbon*, 2013, 59, 264-269.

121. B. B. Li, D. P. Yu and S. L. Zhang, *Phys. Rev. B*, 1999, 59, 1645-1648.

122. H. Kim and J. Cho, *Nano Lett.*, 2008, 8, 3688-3691.

123. L. Martin, H. Martinez, M. Ulldemolins, B. Pecquenard and F. Le Cras, *Solid State Ionics*, 2012, 215, 36-44.

124. L. B. Chen, K. Wang, X. H. Xie and J. Y. Xie, *J. Power Sources*, 2007, 174, 538-543.

125. J. R. Macdonald, in *Superionic Conductors*, eds. G. Mahan and W. Roth, Springer US, 1976, DOI: 10.1007/978-1-4615-8789-7_6, ch. 6, pp. 81-97.

126. R. Ruffo, S. S. Hong, C. K. Chan, R. A. Huggins and Y. Cui, *J. Mater. Chem. C*, 2009, 113, 11390-11398.

127. T. Zhang, H. P. Zhang, L. C. Yang, B. Wang, Y. P. Wu and T. Takamur, *Electrochim. Acta*, 2008, 53, 5660-5664.

128. B. Markovsky, M. D. Levi and D. Aurbach, *Electrochim. Acta*, 1998, 43, 2287-2304.

129. N. Ding, J. Xu, Y. X. Yao, G. Wegner, X. Fang, C. H. Chen and I. Lieberwirth, *Solid State Ionics*, 2009, 180, 222-225.

130. S. I. Lee, U. H. Jung, Y. S. Kim, M. H. Kim, D. J. Ahn and H. S. Chun, *Korean J. Chem. Eng.*, 2002, 19, 638-644.

131. Y. M. Lee, J. Y. Lee, H. T. Shim, J. K. Lee and J. K. Park, *J. Electrochem. Soc.*, 2007, 154, A515-A519.

132. J. H. Cho and S. T. Picraux, *Nano Lett.*, 2014, 14, 3088-3095.

133. E. Radvanyi, K. Van Havenbergh, W. Porcher, S. Jouanneau, J. S. Bridel, S. Put and S. Franger, *Electrochim. Acta*, 2014, 137, 751-757.

134. S. A. Klankowski, G. P. Pandey, B. A. Cruden, J. W. Liu, J. Wu, R. A. Rojeski and J. Li, *J. Power Sources*, 2015, 276, 73-79.

135. K. Ozawa, *Lithium Ion Rechargeable Batteries: Materials, Technology, and New Applications*, John Wiley & Sons, 2012.

136. B. Markovsky, A. Rodkin, G. Salitra, Y. Talyosef, D. Aurbach and H. J. Kim, *J. Electrochem. Soc.*, 2004, 151, A1068-A1076.

137. J. Wang, Y. K. Zhou, Y. Y. Hu, R. O'Hayre and Z. P. Shao, *J. Phys. Chem. C*, 2011, 115, 2529-2536.

138. L. Kavan, *J. Solid State Electrochem.*, 2014, 18, 2297-2306.

139. R. Van Noorden, *Nature*, 2014, 507, 26-28.

140. M. Armand and J. M. Tarascon, *Nature*, 2008, 451, 652-657.

141. P. Simon, Y. Gogotsi and B. Dunn, *Science*, 2014, 343, 1210-1211.

142. P. G. Bruce, B. Scrosati and J. M. Tarascon, *Angew. Chem. Int. Ed. Engl.*, 2008, 47, 2930-2946.

143. M. Okubo, E. Hosono, J. Kim, M. Enomoto, N. Kojima, T. Kudo, H. Zhou and I. Honma, *J. Am. Chem. Soc.*, 2007, 129, 7444-7452.

144. S. A. Klankowski, R. A. Rojeski, B. A. Cruden, J. W. Liu, J. Wu and J. Li, *J. Mater. Chem. A*, 2013, 1, 1055-1064.

145. H. Lindstrom, S. Sodergren, A. Solbrand, H. Rensmo, J. Hjelm, A. Hagfeldt and S. E. Lindquist, *J. Phys. Chem. B*, 1997, 101, 7710-7716.

146. H. Zhang and P. V. Braun, *Nano Lett.*, 2012, 12, 2778-2783.

147. Z. Weng, F. Li, D. W. Wang, L. Wen and H. M. Cheng, *Angew. Chem. Int. Ed. Engl.*, 2013, 52, 3722-3725.

148. T. Aida, K. Yamada and M. Morita, *Electrochem Solid St*, 2006, 9, A534-A536.

149. S. L. Zhang and N. Pan, *Advanced Energy Materials*, 2015, 5.

150. C. C. Hu, K. H. Chang, M. C. Lin and Y. T. Wu, *Nano Lett.*, 2006, 6, 2690-2695.

151. P. Simon and Y. Gogotsi, *Nat. Mater.*, 2008, 7, 845-854.

152. D. R. Rolison, J. W. Long, J. C. Lytle, A. E. Fischer, C. P. Rhodes, T. M. McEvoy, M. E. Bourg and A. M. Lubers, *Chem. Soc. Rev.*, 2009, 38, 226-252.

153. Z. B. Lei, J. T. Zhang and X. S. Zhao, *J. Mater. Chem.*, 2012, 22, 153-160.

154. J. Desilvestro and O. Haas, *J. Electrochem. Soc.*, 1990, 137, C5-C22.

155. D. M. Adams, L. Brus, C. E. D. Chidsey, S. Creager, C. Creutz, C. R. Kagan, P. V. Kamat, M. Lieberman, S. Lindsay, R. A. Marcus, R. M. Metzger, M. E. Michel-Beyerle, J. R. Miller, M. D. Newton, D. R. Rolison, O. Sankey, K. S. Schanze, J. Yardley and X. Y. Zhu, *J. Phys. Chem. B*, 2003, 107, 6668-6697.

156. R. Huggins, *Advanced batteries: materials science aspects*, Springer, 2008.

157. Y. Yang, J. Choi and Y. Cui, in *Functional Metal Oxide Nanostructures*, eds. J. Wu, J. Cao, W.-Q. Han, A. Janotti and H.-C. Kim, Springer New York, 2012, vol. 149, ch. 12, pp. 269-302.

158. J. E. Weston and B. C. H. Steele, *J. Appl. Electrochem.*, 1980, 10, 49-53.

159. W. Chen, R. B. Rakhi, Q. X. Wang, M. N. Hedhili and H. N. Alshareef, *Adv. Funct. Mater.*, 2014, 24, 3130-3143.

160. F. Li, Y. Xing, M. Huang, K. L. Li, T. T. Yu, Y. X. Zhang and D. Losic, *J. Mater. Chem. A*, 2015, DOI: 10.1039/c5ta00634a, 10.1039/C1035TA00634A

161. K. Zhang, X. Han, Z. Hu, X. Zhang, Z. Tao and J. Chen, *Chem. Soc. Rev.*, 2015, 44, 699-728.

162. M. Zhi, C. Xiang, J. Li, M. Li and N. Wu, *Nanoscale*, 2013, 5, 72-88.

163. P. Simon and Y. Gogotsi, *Acc. Chem. Res.*, 2013, 46, 1094-1103.

164. Z. Fan, J. H. Chen, M. Y. Wang, K. Z. Cui, H. H. Zhou and W. Kuang, *Diamond Relat. Mater.*, 2006, 15, 1478-1483.

165. S. B. Ma, K. Y. Ahn, E. S. Lee, K. H. Oh and K. B. Kim, *Carbon*, 2007, 45, 375-382.

166. J. Yan, Z. J. Fan, T. Wei, J. Cheng, B. Shao, K. Wang, L. P. Song and M. L. Zhang, *J. Power Sources*, 2009, 194, 1202-1207.

167. K. W. Nam, C. W. Lee, X. Q. Yang, B. W. Cho, W. S. Yoon and K. B. Kim, *J. Power Sources*, 2009, 188, 323-331.

168. S. L. Chou, J. Z. Wang, S. Y. Chew, H. K. Liu and S. X. Dou, *Electrochem. Commun.*, 2008, 10, 1724-1727.

169. S. W. Lee, J. Kim, S. Chen, P. T. Hammond and Y. Shao-Horn, *ACS Nano*, 2010, 4, 3889-3896.

170. R. Amade, E. Jover, B. Caglar, T. Mutlu and E. Bertran, *J. Power Sources*, 2011, 196, 5779-5783.

171. H. Zhang, G. Cao, Z. Wang, Y. Yang, Z. Shi and Z. Gu, *Nano Lett.*, 2008, 8, 2664-2668.

172. M. Pourbaix, *Atlas of electrochemical equilibria in aqueous solutions*, Pergamon Press, Oxford, 1974.

173. G. Rayner-Canham and T. Overton, *Descriptive inorganic chemistry*, Macmillan, 2003.

174. M. Chigane and M. Ishikawa, *J. Electrochem. Soc.*, 2000, 147, 2246-2251.

175. M. Chigane, M. Ishikawa and M. Izaki, *J. Electrochem. Soc.*, 2001, 148, D96-D101.

176. C. Huang, N. P. Young and P. S. Grant, *J. Mater. Chem. A*, 2014, 2, 11022-11028.

177. B. E. E. Systems, C. E. T. Systems, S. C. R. R. P. P. N. G. Vehicles, N. R. Council, T. R. Board and D. E. P. Sciences, *Review of the Research Program of the Partnership for a New Generation of Vehicles:: Sixth Report*, National Academies Press, 2000.

178. Y. W. Son, M. L. Cohen and S. G. Louie, *Nature*, 2006, 444, 347-349.

179. R. A. Susantyoko, X. Wang, L. Sun, W. Sasangka, E. Fitzgerald and Q. Zhang, *Nano Energy*, 2015, 12, 521-527.

180. L. Sun, Y. Fan, X. Wang, R. Agung Susantyoko and Q. Zhang, *Nanotechnology*, 2014, 25, 255302.

181. R. A. Susantyoko, X. Wang, Y. Fan, Q. Xiao, E. Fitzgerald, K. L. Pey and Q. Zhang, *Thin Solid Films*, 2014, 558, 356-364.

182. X. Wang, L. Sun, R. Agung Susantyoko, Y. Fan and Q. Zhang, *Nano Energy*, 2014, 8, 71-77.

183. L. Zhang, K. Jin, L. Wang, Y. Zhang, X. Li and Y. Song, *J. Alloy. Compd.*, 2015, 638, 298-304.

184. G. Hautier, A. Jain, H. L. Chen, C. Moore, S. P. Ong and G. Ceder, *J. Mater. Chem.*, 2011, 21, 17147-17153.

185. G. Hautier, C. C. Fischer, A. Jain, T. Mueller and G. Ceder, *Chem. Mater.*, 2010, 22, 3762-3767.